

**Design, Modeling, Fabrication, Testing, and Verification of Arrayed Micro-Photosynthetic  
Power Cells**

Soroush Rahimi

A Thesis

in

The Department

of

Mechanical, Industrial and Aerospace Engineering

Presented in Partial Fulfillment of the Requirements

For the Degree of Master of Applied Science (Mechanical Engineering) at

Concordia University

Montreal, Quebec, Canada

August 2021

© Soroush Rahimi, 2021

CONCORDIA UNIVERSITY  
School of Graduate Studies

This is to certify that the thesis prepared

By: Soroush Rahimi

Entitled: Design, Modeling, Fabrication, Testing, and Verification of Arrayed Micro-Photosynthetic Power Cells

and submitted in partial fulfillment of the requirements for the degree of

**Master of Applied Science (Mechanical Engineering)**

complies with the regulations of the University and meets the accepted standards with respect to originality and quality.

Signed by the final examining committee:

Dr. Rama Bhat Chair

Dr. Rama Bhat Examiner

Dr. Wei-Ping Zhu Examiner

Dr. Muthukumaran Packirisamy Thesis Supervisor(s)

\_\_\_\_\_ Thesis Supervisor(s)

Approved by \_\_\_\_\_

Dr. Sivakumar Narayanswamy, Chair of Department or Graduate Program Director

August 31, 2021

\_\_\_\_\_  
Dr. Mourad Debbabi, Dean of Faculty

## Abstract

### **Design, Modeling, Fabrication, Testing, and Verification of Arrayed Micro-Photosynthetic Power Cells**

Soroush Rahimi

The demand for implementing the energy harvesting systems to power up the sensors in the IoT applications attracted the attention of the scientists to bio-energy harvesting systems as a clean source of energy. Micro-photosynthetic power cell ( $\mu$ -PSC) is a promising technology that uses the photosynthetic microalgae culture to generate power at a micro-scale. The main objective of this thesis is to develop the design, fabrication, and performance investigation of the arrayed  $\mu$ -PSC. In addition, an improved model to predict the electrical behavior of the  $\mu$ -PSC is developed and corresponding results have been validated with the experimental characteristics of a single  $\mu$ -PSC.

In this study, the two techniques of fabricating  $1 \times 3$  array of  $\mu$ -PSC are developed. One consists of interconnected  $\mu$ -PSCs fabricated using 3D-printing of Polylactic Acid plastic frames, and the other design is made of independent  $\mu$ -PSCs molded with EPON 862 resin in a 3D printed mold. The biocompatibility of the selected materials is tested prior to the fabrication. Experiments are performed on both array designs to investigate the primary electrical parameters, including cell voltage, cell current, I-V characteristics, power characteristics and peak power. Testing of interconnected arrayed  $\mu$ -PSC showed about three times output current as that of the single chip. The tested performance characteristics of the independently arrayed  $\mu$ -PSC showed very similar trend as single  $\mu$ -PSC chip. Hence, by a proper series and parallel connection, higher level of current and voltage can be obtained. Interconnected array produced maximum Open Circuit Voltage (OCV) of about 850mV, Short Circuit Current (SCC) of 2.5mA, peak power of 0.54 mW and Fill Factor of 0.224 while the independent array produced OCV of around 820mV, SCC of 1mA peak power of 0.25 mW and Fill Factor of 0.262.

The modeling was verified with test characteristics and the agreement between prediction and testing was about 90%. The presented fabrication processes for making arrays of  $\mu$ -PSC are easier and faster compared to the previous techniques used for making single-chip  $\mu$ -PSC. This study revealed that multiple independently arrayed chips can be used to power-up sensors by proper electrical combination as a future work.

*To my beloved*  
*Father, Alireza*  
*Mother, Vahideh*  
*Brother, Sepehr*

## **Acknowledgment**

I would like to express my deepest gratitude to my advisor Professor Muthukumaran Packirisamy for accepting me as a part of his Optical-Bio Microsystems group. I am so honored to work under his supervision and as a member of a cutting-edge research team Micro-photosynthetic power cell. His guidance, novel ideas, and supports directed me through the greatest obstacles through my research and helped me to deepen my knowledge and being creative through this path.

I would like to thank Dr. Kiran Kuruvinashetti, the graduated Ph.D. student who helped me through my research. I also want to thank the research group members at Optical-Bio Microsystems Laboratory, including Dr. Mohsen Habibi and Shervin Foroughi and the others, for their kind advice.

In the end, I would like to thank my mother, my father, my brother, and my uncles for their unconditional support, patience and advice throughout my study.

# Contents

List of Figures .....	x
List of Tables .....	xiv
Nomenclature .....	xv
1. Introduction: Looking Into How Algae Can Help With Our Energy Demand.....	1
1.1. Energy Demand.....	1
1.2. Technologies and Devices.....	1
1.2.1. Fuel Cell .....	2
1.2.2. Solar Cell .....	3
1.2.3. Microbial Fuel Cell.....	5
1.2.4. Micro-Photosynthetic Power Pell ( $\mu$ -PSC) .....	7
1.3. Energy Conversion in $\mu$ -PSC .....	7
1.4. Photosynthesis and Respiration.....	8
1.4.1. Light and Chloroplast Absorption .....	8
1.4.2. Photosynthesis Organelles.....	9
1.4.3. Photosynthesis Electron Transfer Processes.....	11
1.4.4. Light-Independent Processes .....	13
1.4.5. Photosynthesis Limiting Factors .....	15
1.4.5.1. Light.....	16
1.4.5.2. Temperature .....	16
1.4.5.3. Carbon Dioxide.....	17
1.4.5.4. Nutrient Availability.....	17
1.5. History .....	17
1.6. $\mu$ -PSC Principle of Operation .....	21

1.6.1. Single-Chip Configuration .....	21
1.6.2. Operation Mechanism.....	22
1.7. Thesis Motivation.....	23
1.8. Thesis Objectives and Scopes .....	23
1.9. Contributions.....	24
2. Finite Element Analysis of the Micro-Photosynthetic Power Cell and Verification.....	26
2.1. Introduction .....	27
2.2. $\mu$ -PSC Operation Principles .....	29
2.3. Implementation of Micro-Photosynthetic Power Cell Model Analysis in COMSOL Multiphysics.....	31
2.3.1. Governing Equations .....	33
2.3.1.1. Electrical Modeling.....	33
2.3.1.2. Chemical Reaction Modeling .....	38
2.4.2. Model Geometry.....	42
2.4.3. Assumptions .....	43
2.4.4. Parameters and Constants.....	44
2.4.5. Mesh Configuration.....	45
2.5. Modeling Results.....	45
2.5.1. I-V Characteristics and Power Curve .....	46
2.5.2. Effect of Internal Resistance.....	48
2.5.3. Temperature Effect .....	50
2.5.4. Effect of Active Surface Area on the Output Power .....	52
2.6. Validation of Modeling Results .....	54
2.7. Conclusion.....	60
3. Design, Development and Verification of an Interconnected Array Micro-Photosynthetic Power Cell.....	61

3.1. Introduction .....	61
3.2. Principle of Operation .....	63
3.3. Material Selection Experiment.....	64
3.3.1. Materials and Method.....	65
3.3.1.1. Materials .....	65
3.3.1.2. Cell Culture.....	66
3.3.1.3. Catholyte Material .....	67
3.3.2. Methodology.....	68
3.3.3. Discussion on Material Selection .....	72
3.4. Geometry and Design.....	73
3.4.1. Chambers and Gaskets.....	74
3.4.2. Membrane-Electrode-Assembly.....	77
3.4.2.1. Membrane .....	77
3.4.2.2. Electrode Preparation.....	78
3.4.2.3. Assembly.....	79
3.5. Test Scheme .....	80
3.6. Experimental results.....	82
3.6. Validation of Modeling and Experiment.....	87
3.7. Conclusion.....	89
4. Design, Development, and Verification of an Independent Array of Micro-Photosynthetic Power Cell.....	90
4.1. Introduction .....	90
4.2. Independent Arrayed $\mu$ -PSC Design and Fabrication .....	93
4.2.1. Geometry and Design .....	93
4.2.2. Fabrication Process.....	96

4.2.3. Device Assembly .....	98
4.3. Experiment Condition and Setup .....	99
4.4. Experimental Characterization .....	101
4.4.1. Open-Circuit Voltage .....	101
4.4.2. Short-Circuit Current .....	103
4.4.3. Constant Loading Characterization .....	104
4.4.4. I-V Characteristics .....	106
4.4.5. Fill Factor .....	110
4.4.6. Array Configuration .....	112
4.5. Conclusion .....	115
5. Conclusion and Future Works .....	117
5.1. Conclusion .....	117
5.2. Future Works .....	118
References .....	120

## List of Figures

Figure 1.1 U.S. PV electricity capacity and generation.....	5
Figure 1.2 Schematic of the operating principle of a microbial fuel cell .....	6
Figure 1.3 The solar spectrum and its relation to the absorption spectrum of Chlorophyll .....	9
Figure 1.4 Chlamydomonas reinhardtii structure .....	10
Figure 1.5 Organelles inside chloroplast .....	10
Figure 1.6 Vectoral arguments of photosystem I and II .....	11
Figure 1.7 Z scheme of light-dependent photosynthesis process .....	13
Figure 1.8 Light-independent (Calvin-Benson) and carbon fixation cycle .....	15
Figure 1.9 A schematic diagram of photosynthesis rate (P) over light irradiance (I).....	16
Figure 1.10 Micro-photosynthetic power cell development major timeline.....	20
Figure 1.11 General schematic of the single-chip $\mu$ -PSC device .....	21
Figure 1.12 Principal of operation of the $\mu$ -PSC .....	22
Figure 2.1 $\mu$ -PSC principle of operation.....	30
Figure 2.2 Flowchart of the numerical analysis procedure in COMSOL Multiphysics .....	32
Figure 2.3 General polarization curve and the voltage loss domains .....	33
Figure 2.4 Boundary conditions of the $\mu$ -PSC model.....	42
Figure 2.5 geometry of the $\mu$ -PSC model .....	43
Figure 2.6 Overall view of Fill Factor Calculation.....	46
Figure 2.7 Predicted performance of the 22mm $\mu$ -PSC chip for (a) voltage-current variation, (b) current variation over resistance change, (c) voltage variation over resistance change, (d) power-current variation and (e) power variation over resistance change .....	48
Figure 2.8 Prediction of the (a) I-V characteristics and (b) power characterization at various internal resistance.....	49

Figure 2.9 Variation of OCV (mV), SCC (mA) and peak power point from the prediction at various internal resistance.....	50
Figure 2.10 Prediction of the (a) I-V characteristics and (b) power characterization at various temperature in COMSOL modeling.....	51
Figure 2.11 Prediction of the effect of active surface area on the (a) power curve and (b) polarization curve.....	53
Figure 2.12 Variation of OCV (mV), SCC (mA) and peak power point from the prediction at various active surface area .....	54
Figure 2.13 (a) Fabrication process of a single-chip $\mu$ -PSC, (b) experiment setup of the single-chip $\mu$ -PSC and (c) the schematic of single-chip $\mu$ -PSC test for the I-V characterization .....	56
Figure 2.14 I-V curve of model prediction and experimental data.....	57
Figure 2.15 Power-current curve of model prediction and experimental data .....	58
Figure 2.16 (a) Current-load resistance, (b) voltage-load resistance curve and (c) power-load resistance curve of model prediction and experimental data .....	59
Figure 3.1 $\mu$ -PSC principle of operation.....	63
Figure 3.2 Experiment preparation steps schematic of the biocompatibility of test specimens and microalgae culture.....	69
Figure 3.3 14 Days visual inspection of the sample plate.....	70
Figure 3.4 Optical 60x microscopic image of CC-125 in contact with (a) PDMS, (b) EPON 862, (c) PLA, (d) Formlabs clear resin, (e) D.E.R 324, and (f) CC-125 only .....	72
Figure 3.5. Exploded view of the interconnected array of $\mu$ -PSC.....	74
Figure 3.6 FDM layer-by-layer printing pattern.....	75
Figure 3.7 Integrated internally connected $\mu$ -PSC geometical specifications .....	76
Figure 3.8 Isometric view of the integrated internally connected $\mu$ -PSC chamber.....	76
Figure 3.9 Membrane-Electrode Assembly (MEA) view after fabrication .....	80
Figure 3.10 General schematic of (a) OCV and (b) SCC electrical circuit measurement for the interconnected array of $\mu$ -PSC.....	81

Figure 3.11 (a) Experimental setup of the interconnected array of $\mu$ -PSC and (b) general schematic of the load current and voltage measurement for the interconnected array of $\mu$ -PSC.	82
Figure 3.12. $\mu$ -PSC cells and electrical terminals notation for interconnected design.....	82
Figure 3.13 Transient behavior of the OCV in the interconnected array of $\mu$ -PSC.....	83
Figure 3.14 SCC data for each electrical connection of the integrated internally connection $\mu$ -PSC device.....	85
Figure 3.15 (a) I-V characteristics and (b) power-current data of the cells of the interconnected design.....	86
Figure 3.16 (a) I-V characteristics and (b) power curve for model prediction (shown with lines and dot lines) and experimental data for cell 2 (shown with data points and error bars).....	88
Figure 4.1 (a) Exploded view of the independent arrayed $\mu$ -PSC and complete geometrical specification* of (a) $\mu$ -PSC array and (b) high-temperature resin mold specification.....	95
Figure 4.2 Independently arrayed $\mu$ -PSC frame with EPON 826 and.....	96
Figure 4.3 Bonded PDMS to the epoxy chamber of independently arrayed $\mu$ -PSC and (b) final view of the bonded PDMS gasket and chamber after removing extra PDMS layer.....	97
Figure 4.4 Final Assembly of the $\mu$ -PSC array design.....	99
Figure 4.5 Overall view Experiment setup of the Independent arrayed $\mu$ -PSC.....	101
Figure 4.6 OCV data for 60 minutes test of each chip in the Independently arrayed $\mu$ -PSC.....	102
Figure 4.7 Long-term OCV data observation of the Independent arrayed $\mu$ -PSC.....	103
Figure 4.8 Short-circuit current data for each chip of the independently arrayed $\mu$ -PSC with the error bars showing one unit of standard deviation of the collected data.....	104
Figure 4.9 1kOhm loading data of (a) load current and (b) load voltage in 60 minutes.....	105
Figure 4.10 Proton exchange membranes deformation image after the test of independently arrayed $\mu$ -PSC.....	107
Figure 4.11 (a), (c), (e) I-V characteristics and (b), (d), (f) power-current curve of the Independent arrayed $\mu$ -PSC cells.....	109

Figure 4.12 Peak power variation of the  $\mu$ -PSC at various limiting current density and PEM conductivity..... 110

Figure 4.13 Modeling results fill factor of the Independent arrayed  $\mu$ -PSC cells ..... 111

Figure 4.14 (a) Parallel and (b) series combination for the test of independent arrayed  $\mu$ -PSC 113

Figure 4.15 (a)I-V characteristics and (b) power curve of three chips in series and parallel of the independent arrayed  $\mu$ -PSC ..... 114

## List of Tables

Table 1.1 Comparison of major fuel cell types.....	3
Table 1.2 Brief description of different Photovoltaic solar cells.....	4
Table 2.1 Geometrical specifications for the $\mu$ -PSC model .....	42
Table 2.2 $\mu$ -PSC Model parameters.....	44
Table 2.3 OCV, SCC, Peak Power and Fill Factor variation of model prediction and experimental data.....	60
Table 3.1 Material specification for the $\mu$ -PSC frame.....	66
Table 3.2. Preparation steps for 1 liter of TAP media .....	67
Table 3.3 Geometrical specification of the Aluminum grid .....	79
Table 3.4. Variation of OCV at every two terminals of the interconnected $\mu$ -PSC in mV .....	83
Table 4.1 Summary of MEA preparation steps .....	98
Table 4.2 The load voltage and load current of each chip of the independently arrayed $\mu$ -PSC at various constant loadings (range of variation is equal to one unit of standard deviation of the recording data) .....	105
Table 4.3 Simulation parameter change for Independent arrayed $\mu$ -PSC .....	107
Table 4.4 Modeling fill factor value for the Independent arrayed $\mu$ -PSC cells.....	112

## Nomenclature

$E_{anode}^0$	Standard anode electrochemical potential
$E_{cathode}^0$	Standard cathode electrochemical potential
$E_{cell}^0$	Standard Electromotive Force
$A$	Electrode surface Area
ATP	Adenosine Triphosphate
$C_b$	Concentration of $i^{th}$ component in the bulk region
$C_i$	Concentration of $i^{th}$ component near electrode surface
$D$	Diffusion coefficient
DI water	Deionized water
EMF	Electromotive Force
$E_{Nernst}$	Nernst reversible Voltage
$F$	Faraday Constant
FDM	Fused Deposition Modelling
FF	Fill Factor
GEP	Glycerate Three Phosphate
$I_{\mu PSC}$	Current of Micro-Photosynthetic Power Cell
$I_{MP}$	Cell current at maximum power point
IoT	Internet of Things
$I_{SC}$	Maximum measured current in Micro-Photosynthetic Power Cell
$j_0$	equilibrium exchange current density
$j_i$	Diffusion flux of $i^{th}$ species
$j_k$	Local current density in the absence of concentration loss
$j_{lim}$	Limiting current density
$j_{loc}$	Local Current Density
$L$	Length of the Micro-Photosynthetic Power Cell chamber
LPCVD	Low-Pressure Chemical Vapor Deposition
MB	Methylene Blue
MBH	Reduced Methylene Blue
MEA	Membrane-Electrode-Assembly
MEMS	Micro-Electromechanical Systems
MFC	Microbial Fuel Cell
$M_i$	Molar mass of $i^{th}$ species
$n$	Number of exchanged electrons in mole
NADPH	Nicotinamide Adenine Dinucleotide Phosphate
OCV	Open-Circuit Voltage
PAFC	Phosphoric Acid Fuel Cell
PEM	Proton Exchange Membrane
PEMFC	Proton Electrolyte Membrane Fuel Cell
PF	Potassium Ferricyanide

<b>pH</b>	Potential of Hydrogen
<b>PLA</b>	Polylactic Acid
<b>PS</b>	Photosystem
<b>PV</b>	Photovoltaic
<b><i>Q</i></b>	Electron Charge Transfer
<b><i>R</i></b>	Universal Gas Constant
<b><i>R<sub>electrons</sub></i></b>	Resistance toward electrons transfer
<b><i>R<sub>i</sub></i></b>	Reaction rate of $i^{\text{th}}$ species
<b><i>R<sub>int</sub></i></b>	Internal resistance of the Micro-Photosynthetic Power Cell
<b><i>R<sub>load</sub></i></b>	Load resistance
<b><i>R<sub>protons</sub></i></b>	Resistance toward protons transfer
<b>SCC</b>	Short-Circuit Current
<b>SLA</b>	Stereolithography
<b><i>T</i></b>	Temperature
<b>TAP</b>	Tris-Acetate-Phosphate
<b>TEA</b>	Terminal Electron Acceptor
<b><i>u</i></b>	Velocity
<b><i>V<sub>μPSC</sub></i></b>	Voltage of Micro-Photosynthetic Power Cell
<b><i>V<sub>act</sub></i></b>	Activation Potential Barrier
<b><i>V<sub>conc</sub></i></b>	Concentration Potential Loss
<b><i>V<sub>MP</sub></i></b>	Cell voltage at maximum power point
<b><i>V<sub>OC</sub></i></b>	Maximum measured voltage in Micro-Photosynthetic Power Cell
<b><i>V<sub>ohmic</sub></i></b>	Ohmic Potential Loss
<b><i>W</i></b>	Width of the Micro-Photosynthetic Power Cell chamber
<b><i>x<sub>k</sub></i></b>	mole fraction of $k^{\text{th}}$ species
<b><i>α<sub>Ox</sub></i></b>	charge transfer coefficient of the oxidation reaction
<b><i>α<sub>Red</sub></i></b>	charge transfer coefficient of the reduction reaction
<b><i>ΔG</i></b>	Gibbs free energy
<b><i>ΔG<sup>0</sup></i></b>	Gibbs free energy in the standard condition
<b><i>δ<sub>PEM</sub></i></b>	Proton exchange membrane thickness
<b><i>ε</i></b>	Electrode porosity
<b>μ-PSC</b>	Micro-Photosynthetic Power Cell
<b><i>v<sub>Ox</sub></i></b>	Stoichiometric coefficient of oxidized species
<b><i>v<sub>Red</sub></i></b>	Stoichiometric coefficient of reduced species
<b><i>Π</i></b>	Reaction Quotient
<b><i>ρ</i></b>	Density
<b><i>σ<sub>PEM</sub></i></b>	Proton exchange membrane conductivity
<b><i>Fe(CN)<sub>6</sub><sup>3-</sup></i></b>	Ferricyanide Ion
<b><i>Fe(CN)<sub>6</sub><sup>4-</sup></i></b>	Ferrocyanide Ion

# **1. Introduction: Looking Into How Algae Can Help With Our Energy Demand**

## **1.1. Energy Demand**

The ever-growing demand for energy[1] requires vast sources of fossil fuels which dramatically infect the environment. Global warming, air and water pollutions are the main problems of this over-utilization. On the other hand, the limitation of the current resources is the other critical reason for phasing out fossil fuels and replacing them with renewable energy sources mentioned from wind, solar, biomass, fuel cells, etc. This shift is gradually in progress and estimated to be completed in 2050[2].

The development of the Internet of Things (IoT) technology that is told to dominate the economy's future [3] is entirely dependent on energy supplies. Smart cities, homes, factories, measurement systems, and sensors, etc., are all examples that will be malfunctional without a proper, clean, and reliable source of energy[3]. Accordingly, increasing focus on the new type of energy harvesting systems and technologies is getting more attention each day.

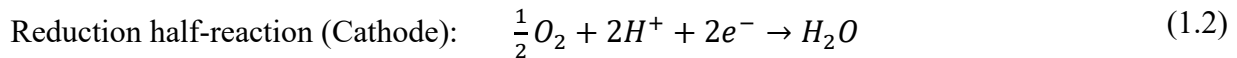
## **1.2. Technologies and Devices**

Recent studies[4] in solar panels, fuel cells, wind turbines, piezo thermal, and piezoelectric devices made glorious advancements in the rate of power output which can then be stored into batteries of different types for utilization. In spite of the fact that all the mentioned technologies are green with their advantages and disadvantages, which will be explained in this chapter, the environmental impacts, high cost, and inadequate power density are the main obstacles in IoT devices.

On the other hand, Micro-electromechanical systems, widely known as MEMS, are developing technology with possible applications in different scientific fields and energy harvesting systems. The reason behind is their low power requirement for proper functionality which keeps them as one the leading technologies in energy harvesting systems[5]. Some of the mentioned technologies in energy harvesting will be presented to portray the problem better.

### 1.2.1. Fuel Cell

Fuel cell is one of the emerging energy harvesting technologies which transforms electrochemical energy to electrical energy. Conceptually, the fuel cell harnesses the electrons as they move from high-energy reactant bonds in the chemical compound, which is fed into the system. In the simplest form, the following half-reactions taking place:



Electrons transfer from the anode through an electrode and an external load in the middle and reach the positive charges (protons) in the cathode side, which are already transferred through an electrolyte material, proton exchange membrane (PEM). Accordingly, the mentioned process would keep taking place as long as the hydrogen is supplied into the system. This is almost the same as the many other energy harvesting systems. However, as the energy conversion process is free of any pollutant like combustible engines, the efficiency showed to be higher depending on the application. In addition, the rate of pollutant chemicals such as  $NO_x$  and  $SO_x$  are almost zero due to the nature of the system. Besides, compared to batteries that show degraded performance in large size, fuel cells can be enlarged for almost Megawatt usage[6].

Despite mentioned advantages, at the moment, fuel cell manufacturing and utilization is costly and not worth manufacturing except for a small number of high-technology applications such as propulsion and some other systems in spacecrafts[7], [8]. Another limiting factor of fuel cells' wide usage is their low power density per unit volume (Volumetric power density) of the fuel or per unit mass (Gravimetric power density) of the fuel, which can not satisfy the industrial needs until now. In addition, hydrogen gas as a fuel has a complex, costly, and time-consuming preparation process. Even though other gases can be replaced with hydrogen, the output results cannot still satisfy the needs[9].

There are various types of fuel cells under study, which can be divided according to their electrolyte material. The major classifications are as follow[6]:

- Phosphoric acid fuel cell (PAFC)

- Alkaline fuel cell (AFC)
- Polymer electrolyte membrane fuel cell (PEMFC)
- Solid-oxide fuel cell (SOFC)
- Molten carbonate fuel cell (MCFC)

The study of the details of each of the mentioned fuel cells is not the main scope of the current thesis, and only a brief comparison between the mentioned fuel cell types is provided in Table 1.1.

Table 1.1 Comparison of major fuel cell types[10]

	<b>PEFC</b>	<b>AFC</b>	<b>PAFC</b>	<b>MCFC</b>	<b>SOFC</b>
<b>Electrolyte</b>	Hydrated polymeric Ion exchange membranes	Potassium hydroxide in asbestos matrix	Immobilized liquid phosphoric acid in SiC	Immobilized liquid molten carbonate in $LiAlO_2$	Perovskites (Ceramics)
<b>Electrodes</b>	Carbon	Transition metals	Carbon	Nickel and Nickel Oxide	Perovskite and metal cermet
<b>Charge Carrier</b>	$H^+$	$H^+$	$OH^-$	$CO_3^{2-}$	$O^{2-}$
<b>Operating Temperature</b>	40 – 80 °C	65 - 220 °C	205 °C	650 °C	600 – 1000 °C
<b>Catalyst</b>	Platinum	Platinum	Platinum	Nickel	Electrode metal / Ceramic
<b>Fuel compatibility</b>	$H_2$ , Methanol	$H_2$	$H_2$	$H_2$ , $CH_4$	$H_2$ , $CH_4$ , $CO$

### 1.2.2. Solar Cell

The evolution of light-sensitive semiconductors through the past decades changed the future perspective of the energy harvesting system. Doubtlessly speaking, the development of photovoltaic solar cells can be directly subjected to the presence of high-performance semiconductors. Light photons reach the panel's surface, and depending on the materials, a fraction of light reflects from the surface, and the rest enter the semi-conductor inside the panel. Most of the photons absorbed by the semi-conductor, transfers their energies to the electron-hole pairs and results in the measurable voltage and current from the solar cell[11].

From the first photovoltaic (PV) effect detected in 1839, various types of PV solar cells have been developed. Table 1.2 provides a brief description of different leading photovoltaic solar cell technologies. According to Table 1.2, each technology has its limitations and advantages.

Table 1.2 Brief description of different Photovoltaic solar cells[12]–[14]

	<b>Crystalline Silicone</b>		<b>Thin film</b>		<b>Third generation</b>	
<b>Cell type</b>	Monocrystalline	Polycrystalline	CdTe	CIGS	Nanocrystal	Concentrated
<b>Efficiency</b>	14% - 17.5%	12% - 14%	9% - 11%	10% - 12%	7% - 8%	40%
<b>High-temperature performance</b>	Not good at high temperature		Good at high temperature	Good in cold and high temperature	Perfect thermal stability	Perfect thermal stability
<b>Size</b>	Requires less volume for similar power generation		Offering a wide of range of design choices		Offering a wide range of design choices	Offering a specialized range of product design
<b>Cost</b>	Expensive crystalline silicone	Cheapest crystalline silicone	Most cost-effective – Half of the cost of crystalline silicone	Half of the cost of crystalline silicone	Half of the cost of crystalline silicone	Half of the cost of conventional Si cells
<b>Other details</b>	Oldest PV technology	Economical choice	Cd toxicity	High performance in some cells	Short installation time and large space	Long installation time and large space

The primary purpose of shifting from fossil fuels into clean energies is to minimize environmental pollutants such as  $CO_2$  emission into the atmosphere. Accordingly, as one of the leading clean technologies, solar cells are getting more portion of the total energy production industry each day (Figure 1.1). One of the main reasons for this development is the abundant free source of sunlight in every part of this planet. In addition, it does not require many workforces for its functional operation, which noticeably reduces the final price of the energy-generating this way. Moreover, the lack of noise pollution of solar cells both on a small scale and large scale makes them popular for urban usage[12].

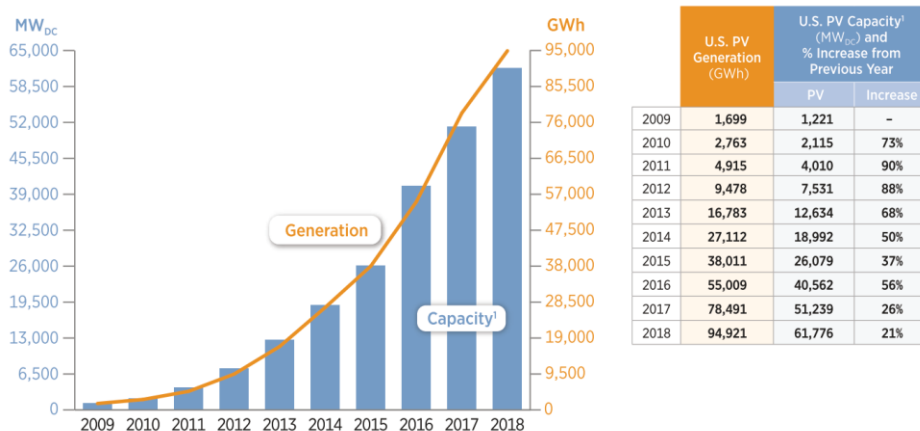


Figure 1.1 U.S. PV electricity capacity and generation[15]

Despite the provided advantages, solar cell technology has some severe limitations and disadvantages. The main part refers to the fact that the fuel supply, which is sunlight, is not available at night, shutting down the system for some hours. In addition, the light intensity must be higher than a specific level for the proper performance of the system. Thus, climate fluctuation, including clouds, rain, and thunder, can drastically reduce solar cell performance[11], [12]. Consequently, the presence of proper battery technology for saving the produced energy is required. Battery utilization of any kind results in different environmental pollutions regarding battery production processes, outdated waste batteries, etc. In addition, the conversion of raw  $SiO_2$  to solar-grade Si which are the main components in the solar cell, leads to an additional production cost and pollution making which therefore makes technology not that green as what many imagine[16].

### 1.2.3. Microbial Fuel Cell

One of the developing technologies in energy harvesting systems is microbial fuel cells (MFC) that implement active microorganisms as biocatalysts in an anode compartment for electricity production. Microorganisms oxidize organic matter with a series of respiratory enzymes and make energy in the form of ATP. On the other hand, the released electrons during the redox reactions reach the terminal electron acceptor (TEA). The common TEAs are oxygen, nitrate, and sulfate.

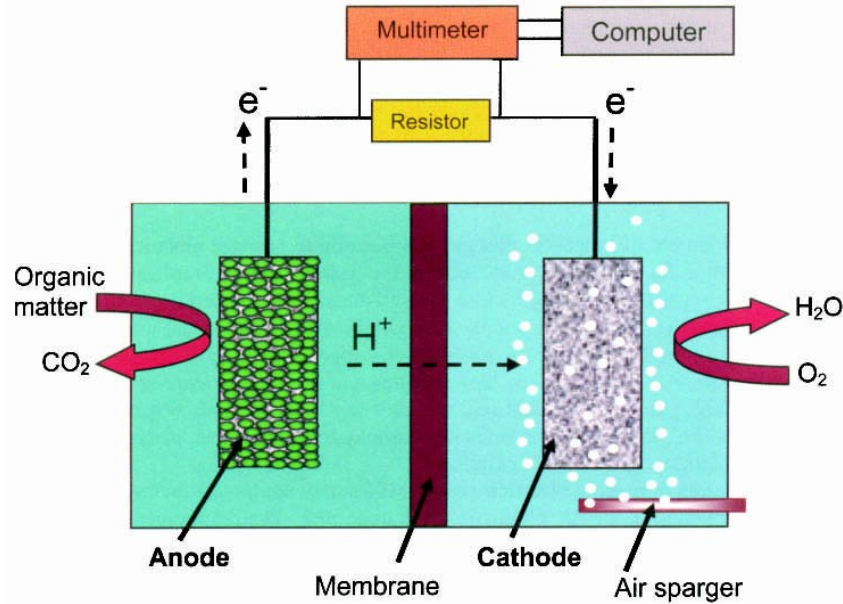


Figure 1.2 Schematic of the operating principle of a microbial fuel cell[17]

Figure 1.2 illustrates the general schematic of most types of microbial fuel cells. The system consists of anode and cathode chambers separated by a proton exchange membrane (PEM). Inside the anode chamber, the bacteria grow in the anode chamber. The design of the system must separate the oxygen from bacteria which can be done by PEM. In some types, the cathode is exposed to air, and the electrons transferred through an external circuit react to the catholyte. In other words, within the reactions that are taking place inside the system, the protons will be transferred from anode to cathode through PEM, and electrons are transferred through the circuit as PEM is only permeable to proton[17], [18]. The general reactions inside the system can be summarized to the two below reactions[19]:



Generally, microbial fuel cells can overcome some challenges in regular fuel cell technology. In addition to the fact that it is environmentally friendly, it can operate in a mild condition which overcomes the high-temperature challenge in normal fuel cells[20]. On the other hand, the waste product of MFC is usually hydrogen which is not dangerous to the atmosphere and environment.[21]

#### 1.2.4. Micro-Photosynthetic Power Pell ( $\mu$ -PSC)

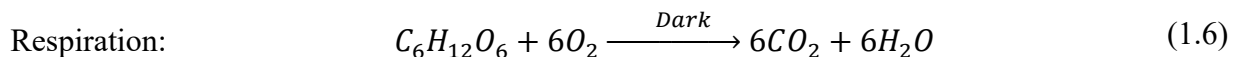
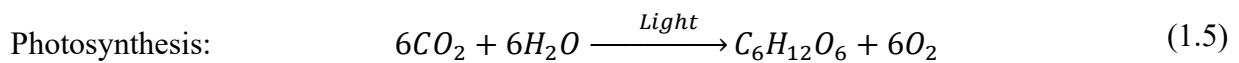
Another promising research technology for future energy harvesting systems, specifically low-power devices, is micro-photosynthetic power cell ( $\mu$ -PSC). It works with the concepts of fuel cell operation in terms of the presence of anode and cathode chambers. In addition, it uses a source similar to the photovoltaic cells.

The  $\mu$ -PSC uses micro living organisms with the capability of photosynthesis. Thus, this system does not require any fuel compared to the fuel cells. Accordingly, many complexities in designing the device are not needed. On the other hand, thermal stresses and well-performing temperature are not a concern as the system's base is biological and properly performs in standard conditions [22].

Photovoltaic solar cells can only be functional under proper light intensity. They will stop functioning in dark conditions and require batteries to save the generated energy for dark condition usages. However,  $\mu$ -PSC technology provides proper functionality in light and dark conditions, and the details will be explained in the following sections. As a result of this characteristic, the need for energy-saving devices can be overlooked for many applications whose energy sources can be supplied using  $\mu$ -PSC. Accordingly, the environmental concerns regarding soil, water, and air pollution caused by the production and wastes of energy-storing systems[23] and solar panels will be solved.

### 1.3. Energy Conversion in $\mu$ -PSC

Photosynthesis is one the most fundamental phenomenon of life on planet earth and is the base of the  $\mu$ -PSC energy conversion mechanism. The reason why  $\mu$ -PSC is able to operate both in dark and light conditions is that bio-organisms perform redox reactions under photosynthesis in the day and respiration at night. In the simplest form, the following reactions take place in living organisms with chloroplast organs:



In the presence of light, Carbon dioxide and water react with the existing other sub-cellular reactions and produce glucose and oxygen. In fact,  $CO_2$  is used as nutrition for the photosynthesis process. On the other hand, in a dark environment, the produced glucose and oxygen become nutrition for reversing the process known as respiration. The details for the mentioned two processes will be explained in the following sections.

Both of the mentioned reactions contain sub-cellular redox (reduction-oxidation) reactions with a large number of electrons transfer and release. The  $\mu$ -PSC provides a novel way to capture and use electrons to supply low-power devices. This includes an external electrical circuit that allows transfers of output current and voltage[24], [25].

## **1.4. Photosynthesis and Respiration**

Living organisms, from plant cells to human cells, are either in the process of production or respiration. The production can be of different types which the most important one is referred to as photosynthesis which occurs in cells with chloroplast and chlorophyll complexes. Meanwhile, some cells, including plant cells, are capable of both photosynthesis and respiration. Simple way, respiration is a process of consuming energy. In the terminology of plant biology is referred to the inverse process of photosynthesis taking place in the dark condition in which the produced glucose during the photosynthesis process is being consumed the production of carbon dioxide and water. The detail of each process will be explained in the following sections.

### **1.4.1. Light and Chloroplast Absorption**

Photosynthesis is the only biological process that can harvest sunlight energy and store it as chemical energy. The photosynthesis process is limited to organisms with Chloroplast and Thylakoid [26].

Sunlight provides light with different wavelengths to the earth, and chlorophyll pigments capture light for photosynthesis. There is a narrow band which Figure 1.3 shows that wavelength close to 400nm and 700nm result in the highest absorption in the Chlorophyll. When photons get absorbed by the chlorophyll pigments, due to the energy transfer between light photons and atoms structures

inside Chlorophyll, the state of atoms gets changed, and photosynthesis reactions start taking place. In photosynthesis, water gets oxidized by the use of solar energy, which consequently produces oxygen. By decreasing the amount of carbon dioxide, large carbon compounds such as glucose are being formed for the respiration process.

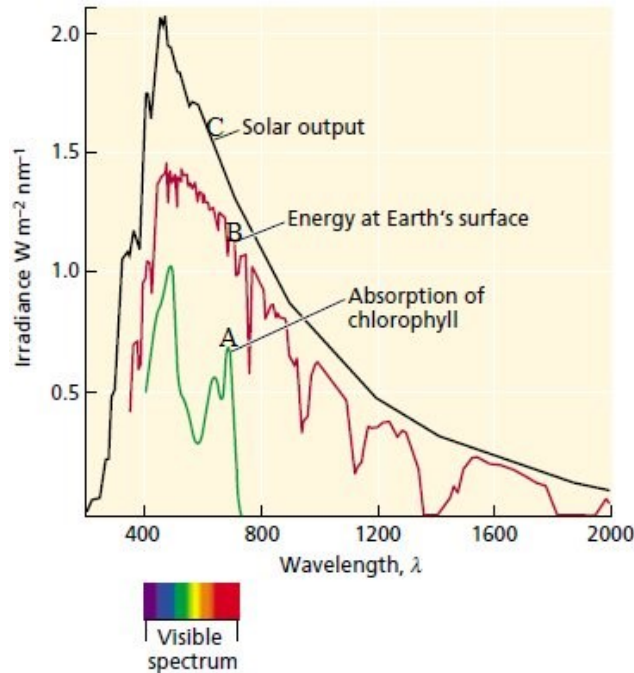


Figure 1.3 The solar spectrum and its relation to the absorption spectrum of Chlorophyll [26]

### 1.4.2. Photosynthesis Organelles

The main microorganism that fits the scopes of this research is green algae (*Chlamydomonas reinhardtii*, wild type CC-125). This microorganism with the approximate size of 5-10 micrometer[27] consists of a nucleus that holds the cell genomes, Chloroplast, which fill a large portion of the cell, Pyrenoid located inside the Chloroplast which is the factory for the carbon fixation process. It is worth mentioning flagella (more specifically Cilium), allowing the microorganism to move inside a medium. Figure 1.4 provides a general view of the organelles inside *Chlamydomonas reinhardtii*.

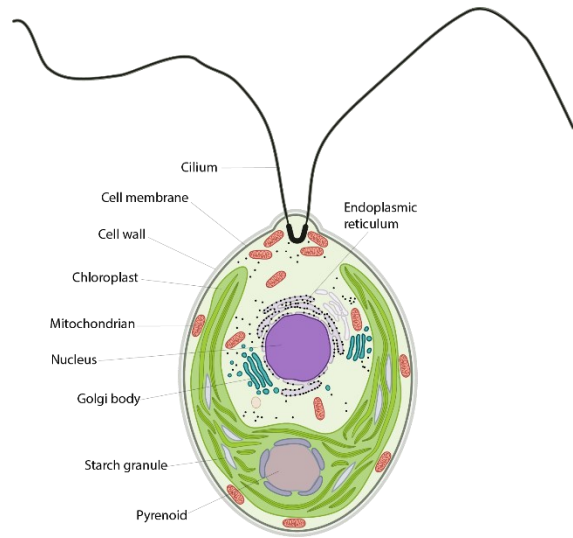


Figure 1.4 Chlamydomonas reinhardtii structure<sup>1</sup>

As mentioned previously, a large portion of green algae cells is filled with Chloroplast, which is the center of the photosynthesis process. The organelles inside the Chloroplast are defined in Figure 1.5. Chloroplast is a double membrane organelle consisting of an inner and outer membrane called chloroplast envelope. The most critical part inside the Chloroplast is Thylakoid in which photosynthesis occurs. Therefore, a large number of Thylakoids exist inside Chloroplast, and they are stacked together called Grana. All the Granum are inside a fluid called Stroma which is the place for light-independent reactions of photosynthesis[26].

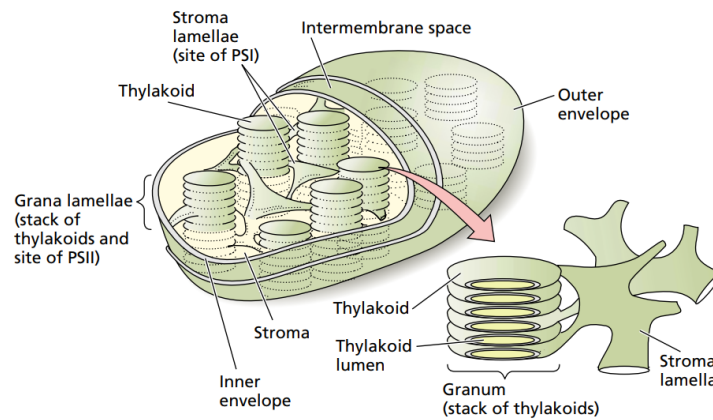


Figure 1.5 Organelles inside chloroplast[26]

<sup>1</sup> Image has been originally captured from Wikipedia and edited

The Thylakoid membrane is the primary location where reactions start. It contains five main complexes: Light-harvesting antenna, photosystem II (PS II), photosystem I (PS I), Cytochrome, and ATP synthase, which is portrayed in Figure 1.6. Inside the Thylakoid, there is a fluid called lumen where the positive charges ( $H^+$ ) temporarily will be kept there.

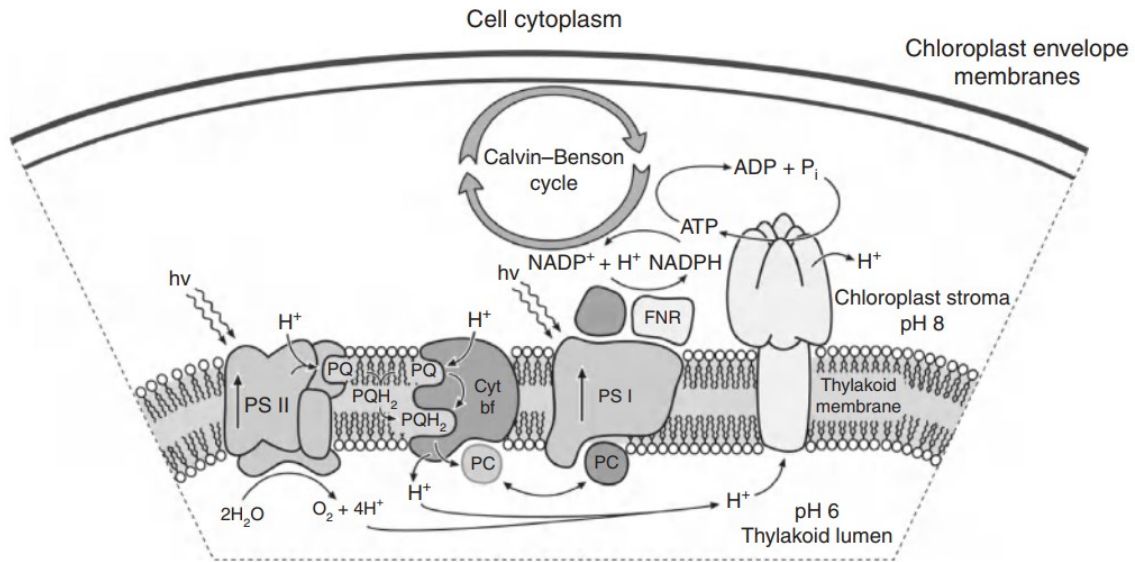


Figure 1.6 Vectorial arguments of photosystem I and II[28]

### 1.4.3. Photosynthesis Electron Transfer Processes

Photosynthesis is a complex series of naturally evolved reactions that is yet under investigation. About 50 different chemical sub-cellular reactions have already been identified since 1771, when Joseph Priestley observed an improvement in candle burning in the presence of a sprig of mint[26]. These reactions are based on the electron release and transfer between different parts inside plant Chloroplast, which builds the basis of energy conversion in  $\mu$ -PSC. The process of photosynthesis can be divided into two stages. The first stage is light-dependent that takes place in Thylakoid. The second stage is light-independent and takes place in Stroma, also known as the Carbon fixation process, and results in the production of glucose[28].

The principal function of light reaction is to build up a bio-chemical reductant known as NADPH and chemical energy sources called ATP, which almost acting as small biological batteries for the

further carbon-fixation and transformation of inorganic carbon. When light is radiate to a plant cell, the visible wavelengths activate the chloroplast light pigment. In other words, light pigments serve as an antenna complex, gathering light and transferring its energy to the reaction center complex. Some of the important light pigments are Billin pigments, Carotenoids and Chlorophyll a. Pigments absorb only a particular wavelength between 400nm to 700nm and reflect the rest. This is the reason why their appearance is colorful in different living organisms[28].

The light photons enter the Chloroplast and get trapped by photosystem I (PS I) and II (PS II), which are pigment-protein complexes. They function in series combination and are connected by a chain of electrons called the “Z scheme” (Figure 1.7) and Cytochrome. A total of 8 light photons are approximately required for PS II to decompose the water molecules into oxygen ions and hydrogen ions[28]. According to this decomposition, two excited electrons are released. Meanwhile, oxygens ions form oxygen which is the waste product of the photosynthesis process.

On the other hand, positive hydrogen ions are kept inside the lumen fluid. The electrons at a higher energy state are transferred from PS II to PS I using a cytochrome protein. This transfer causes electrons' energy to decrease and is spent pumping hydrogen ions from Stroma into Thylakoid actual lumen. The low energy electron enters PS I, and using the same process as of PS II, the energy level of electrons elevates. This elevation causes a conversion in a chemical carrier called  $NADP^+$ , also known as an electron acceptor, to NADPH. The chemical will be implemented in the light-independent stage of the photosynthesis process. With the conversion of  $NADP^+$  to NADPH, the system faces a shortage of electrons. Accordingly, PS II will decompose more water into oxygen gas as a waste product and hydrogen ions into thylakoid lumen fluid[28].



After a while, the concentration of  $H^+$  increases and makes an electrochemical gradient between two sides of the thylakoid membrane: Stroma and lumen fluid. The gradient causes a change in the lumen fluid pH, lowering it down to 6[28]. To reduce this generated gradient, hydrogen ions should be passed through ATP synthase from lumen fluid to Stroma (Figure 1.6). This transformation is accompanied by energy transfer and causes a chemical reaction that starts with

ADP and phosphates inside ATP synthase. The complete reaction is known as non-cyclic photophosphorylation and is as follow:



As mentioned previously, the ATP function is the same as the battery and is the energy carrier that powers up the light-independent process. Hence, the primary product of non-cyclic photophosphorylation is NADPH and ATP, which are the vital parts for completing the photosynthesis cycle[26]. The above reaction keeps taking place until the system confronts the shortage in the amount of NADP<sup>+</sup>. As a result, it changes the process to cyclic photophosphorylation. This process starts with the order as the previous one until the electrons reach PS I. As there are not enough NADP<sup>+</sup> in the system, the released electrons shift back to PS II to repeat the process in which more hydrogen ions will be generated inside the lumen fluid. The result is that more ATP will be generated while no more water is being used. Figure 1.7 shows the whole process and energy levels in a schematic format called “Z scheme”.

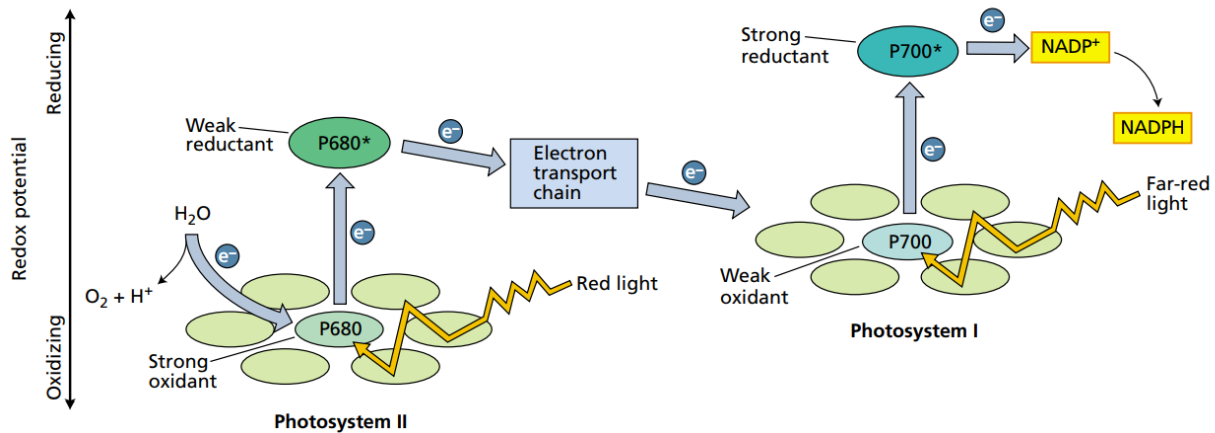


Figure 1.7 Z scheme of light-dependent photosynthesis process[26]

#### 1.4.4. Light-Independent Processes

The light-independent cycle or dark reaction occurs through a cycle known as the Calvin-Benson cycle, in which the inorganic carbons of carbon dioxide turn into simple organic sugar like glucose, also known as the carbon fixation process. In general, it requires two NADPH molecules and three

ATP molecules generating  $5.2E4(J)$  energy. The reaction starts by adding a carbon dioxide molecule to a five-carbon sugar, Ribulose biphosphate<sup>2</sup> (RuBP), and forms two molecules of phosphoglycerate (GP). The necessary catalyst for this reaction is an enzyme called ribulose biphosphate carboxylase, also known as Rubisco. Next, the GP molecules will transform into 3-carbon products or Glycerate three phosphate (GEP). The reaction takes place in the presence of NADPH as a reductant and ATP as an energy source. First, phosphorylation<sup>3</sup> applies to phosphoglycerate<sup>4</sup> to create ADP and diphosphoglycerate. Next, NADPH reduces the diphosphoglycerate and results in the creation of phosphoglyceraldehyde (GELP). With the reduction of NADPH, it will turn back to NADP+, and the ATP will turn back to ADP and phosphates as they do not have an adequate amount of energy[28].

In the next step, more Ribulose phosphate production is taken place to implement more carbon fixation and produce different organic carbon combinations such as 3- or 6- carbon sugar-phosphate. This action can only be done by the presence of aldolase enzymes. It is worth noting that the other varieties of products can be produced during this process depending on the material concentration, available nutrition, and light intensity[28]. Figure 1-8 shows the reaction chain and complete cycle of the light-independent process of photosynthesis.

---

<sup>2</sup> Principal CO<sub>2</sub> acceptor component if photosynthetic organism

<sup>3</sup> addition of phosphoryl group to an organic molecule

<sup>4</sup> an enzyme that catalyzes the reversible transfer of a phosphate group

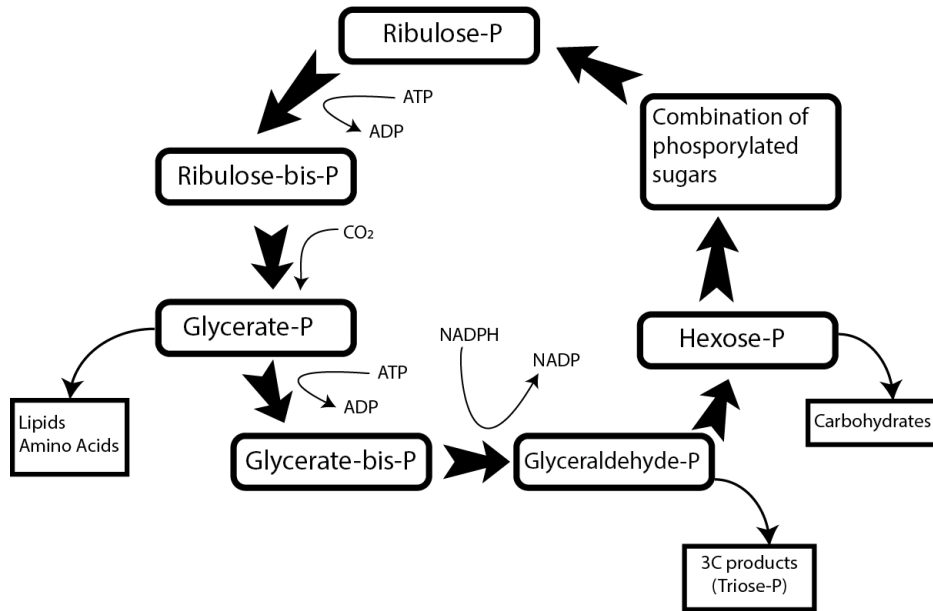


Figure 1.8 Light-independent (Calvin-Benson) and carbon fixation cycle[28]

Most living organisms do cellular respiration, also known as Aerobic respiration, and plants, more specifically microalgae, are not an exception. The specific aspect of plant respiration that distinguishes it from other cellular respiration is the mobilization of reduced organic compounds in a controlled manner. This phenomenon takes place in cell Cytoplasm and Mitochondria, in which the produced glucose in the photosynthesis process will be consumed as the nutrition for the generation of energy (ATP), water, and carbon dioxide[26]. The overall reaction of sucrose oxidization can be expressed as follow:



#### 1.4.5. Photosynthesis Limiting Factors

Photosynthesis is dependent on environmental factors, which can affect the rate and speed of the process. Blackman[26] first established this phenomenon in 1905 when he realized that some parameters are slowing down the process. According to the photosynthesis process discussed previously, four main parameters can reduce or intensify the process.

### 1.4.5.1. Light

Absorbed light by the green cells is the starting point of the process and it significantly affects the whole process. Measures show the total solar energy that reaches a plant, only 5% is used to produce carbohydrates. Figure 1.9 shows the general schematic of the light irradiance on the photosynthesis rate. It shows that after a certain intensity, the photosynthesis rate is saturated, and the rate follows a constant pattern. However, it is worth noting that increasing the intensity to high values can increase the temperature, which can negatively affect the microalgae culture. The effect of light intensity on the performance of  $\mu$ -PSC had been investigated thoroughly. The results show that the light intensity with a value above 230lux satisfies the microalgae need for light irradiance.

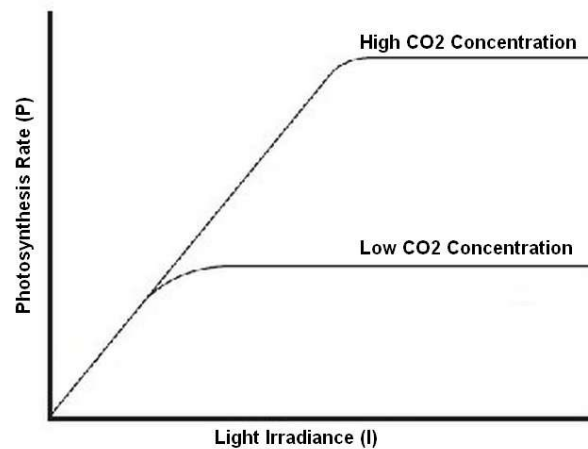


Figure 1.9 A schematic diagram of photosynthesis rate (P) over light irradiance (I)

### 1.4.5.2. Temperature

Temperature is one of the most critical parameters that have a direct effect on the photosynthesis process. The optimal value for the microalgae culture is 25°C[29]. Decker [31] studied the effect of temperature on the loblolly pines. It is approximated that the photosynthesis rate is almost at the same rate at 20°C and 30°C and about 40% decrease once the temperature increased to 40°C. In the current research, the environmental temperature during the cell culture, inoculation, and the  $\mu$ -PSC test are set to 25°C.

### 1.4.5.3. Carbon Dioxide

Carbon dioxide concentration plays a vital role in the rate of photosynthesis. A lower amount of carbon dioxide inside the photosynthetic medium causes a decrease in the rate. However, as a general overview, the Carbon dioxide concentration will be saturated after a particular value depending on the photosynthetic plant and organism[26]. The general schematic is shown in Figure 1.9.

### 1.4.5.4. Nutrient Availability

Several nutrient sources affect the processes of photosynthesis. Generally, Nitrogen, Phosphorus, Iron, and Salinity are the important components that can affect the growth rate of microalgae culture and the photosynthesis rate[28]. The nutrient needs can be different from one cell culture to another. However, the nutrient need for the *Chlamydomonas reinhardtii*, the main culture implemented in this research, has been supplied by the Tris-Acetate-Phosphate (TAP) media.

## 1.5. History

The idea of extracting electrons for generating electricity was first ignited in 1911 by M.C. Potter[30], [31]. However, the practical investigation for bringing the proposed theory to life was ignored until 1931, when Cohen made the first half microbial fuel cell. It follows the principles of electron extraction and transfers from anode to cathode, operating due to the redox potential difference and cause the electrons to travel throughout the electrical circuit.

In the 1980's, Drachev et al.[32], [33] suspend the reaction center and Cytochrome and test the system with redox mediators. The measurements showed a potential of 0.2V. Moreover, Pakham et al. performed the same research, which resulted in almost the same value[34], [35].

Tanaka et al. [36], [37] performed the very first research on measuring the electrical output of cyanobacterium *Anabaena variabilis* in the presence of *HNQ* (2-Hydroxy-1,4-Naphthoquinone) as the redox mediator for photosynthetic electrochemical cell (PEC) in both light and dark

condition and found that the PEC was able to generate electricity in light conditions using endogenous carbohydrates and catabolism in dark conditions.

Yagishita et al.[38] tested a PEC chip using cyanobacterium *variabilis* and *Synchronous*. Results showed the value of 800mV for open-circuit voltage (OCV), the current density of 320 ( $\mu A/cm^2$ ) and power density of 1.4( $mW/cm^2$ ) for the active cell surface area of 7.2 $cm^2$ . In another similar research proposed by Tsujimura et al.[39], the *Synechococcus* cyanobacteria were tested with another material known as DMBQ as a mediator in which showed the output of 80mV for OCV and the current density of 0.4 ( $\mu A/cm^2$ ) and power density of 0.19( $mW/cm^2$ ).

The first research on the development of current micro-photosynthesis power cell was done by Lam et al. in 2003[40]. The system consisted of a cathode and anode chamber, which were fabricated identically and were interchangeable. Chip was fabricated by both-side Low-pressure chemical vapor deposition (LPCVD) deposition and the *Anabaena* algae-gro freshwater used for the experiment. The first experiment measured the chip's electrical power output for two days while the algae culture was in the exponential growth phase and was metabolically active. The second experiment was implemented in a four-day period in the less active stationary phase of the culture. The results indicated that the voltage output after the two-day test was higher than that of the four-day test. The chip was able to properly function in light and dark conditions. Moreover, observation shows an open circuit voltage (OCV) of 200mV in light conditions and 250mV in dark conditions. Furthermore, the comparison with a similar micro-microbial fuel cell indicated that the micro-photosynthesis power cell performance is higher than of microbial version.

In 2006, Lam et al.[41], a photosynthetic electrochemical cell was fabricated in the configuration of a polymer electrolyte fuel cell with the help of *KOH* as the etchant. The chip was tested in both light and dark conditions in constant light intensity. Results showed the 330mV for the OCV after a 4 minutes test under full sunlight intensity and a maximum value of 470mV in the second test. The device then tested under 1k $\Omega$  of external resistance in which shows a current density of 1.1( $\mu A/cm^2$ ) after two minutes of direct illumination. The effect of algae culture flow in both light and dark conditions was also investigated. Qualitatively speaking, the flowing algae culture in dark condition increase the OCV from 60mV to 330mV in five minutes. When the flow condition was changed to a standing medium, the OCV decreased to 280mV in light conditions. However,

changing the condition from light to dark increases the OCV to 330 mV again. This device had a power density of  $5.4 (pW/cm^2)$  at  $1.1 (\mu A/cm^2)$ , maximum current density of  $9.6(\mu A/cm^2)$ .

Rosenbaum et al.[42] utilized microbial metabolic activity for the direct generation of electricity. In their chip configuration, a set of anode and cathode chambers existed, and *Chlamydomonas reinhardtii* (CC-125) was used as the fuel in the system. This research focused on the algal medium and hydrogen production of the system. Algae were cultured in Tris-Acetate-Phosphate (TAP) media at the pH of 7.2. The platinum mesh was used as the electrode, making it different from the electrode type used in the current research. Ninety hours of testing protocol showed that with the increment of hydrogen production resulting from photosynthetic activities of the cells, the output current of the system started to increase just after 24 hours. This research also indicated another protocol for measuring the progress and power generation of today's  $\mu$ -PSC.

Shahparnia et al.[22] designed and fabricated a  $\mu$ PSC based on photosynthesis in blue-green algae. The chip consists of a set of separate anode and cathode chambers with the material of PDMS. The anode and cathode were separated by a proton exchange membrane (PEM), Nafion, which was patterned with gold electrode for electron capturing purposes. The chip was tested under no-load performance and voltage-current (V-I) conditions to define the effect of different bio-design parameters properly. Results showed an OCV of 993 mV and a power peak of  $175.37 \mu W$  at the external load of  $850\Omega$ . The fabricated device also showed a power density of  $36.23(mW/m^2)$  and the current density of  $93.38 (mA/m^2)$ .

In research done by Ramanan[43], a developed prototype of the  $\mu$ -PSC device along with a power electronic converter for energy harvesting applications has been studied. According to the electrical results, a mathematical model has been developed which was able to model the electrical behavior of the  $\mu$ -PSC based on cell current, voltage, and quantum yield. Moreover, three different power electronic converters for low and large power energy harvesting applications have also been developed.

Bombelli et al.[44] tested a mediator-free micro bio photovoltaic power cell. For chip fabrication, soft lithography had been implemented to form the microchannels. The algal culture which had been used in this research was *Synechocystis*. The had been tested for 24 hours in which showed the maximum power density of  $275 (mW/m^2)$  and the current density of  $2840 (mA/m^2)$  in dark

condition. The same test in the light condition proposed a power density of  $294(mW/m^2)$  and the current density of  $2940(mA/m^2)$  in light condition.

Masadeh et al.,[25] electrochemical modeling has been provided based on the chemical reactions happening in the process and the electrochemical kinetics of the system. The results show a relatively low error value for the polarization curve with the SCC value of  $820\mu A$  and  $870mV$  for the OCV. Moreover, the peak power showed to be  $179.36 \mu W$  which happened at the current of  $459\mu A$ . In addition, the effect of temperature variation and internal resistance at different values have also been provided.

Kuruvinashetti[45] worked on a low-cost new fabrication technique for the  $\mu$ -PSC application. It provided the results of the same order as the previous research on the same technology. The results show a short-circuit current (SCC) of around  $750\mu A$  and an open-circuit voltage (OCV) of  $800mV$ . In addition, the electrical outputs for multiple  $\mu$ -PSC devices in series and parallel combinations have been analyzed. The results show higher total voltage in series combination and higher cell current in parallel combination while maintaining the other parameter equal to the lowest value of the cell in the combination. Figure 1.10 shows the timeline of the major development of the Micro-photosynthetic power cell.

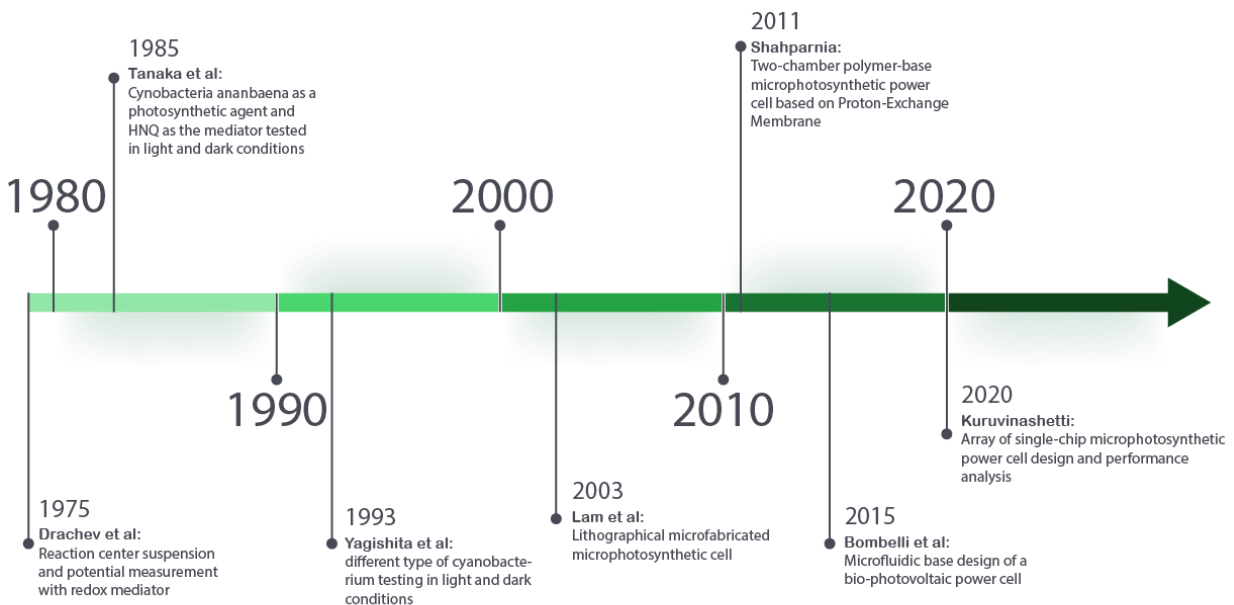


Figure 1.10 Micro-photosynthetic power cell development major timeline

## 1.6. $\mu$ -PSC Principle of Operation

### 1.6.1. Single-Chip Configuration

The originally developed single-chip  $\mu$ -PSC consists of two chambers which are anode and cathode chambers. An anode chamber is where the algal culture is placed, and it is better to keep the anode side on top so that proper light can be radiated to the algae. The cathode chamber is where the mediator can be placed, which acts as an electron acceptor. The materials are of different types, which can be either air, potassium ferricyanide, oxygen, etc. However, different materials can affect the system's performance, and results showed that Potassium Ferricyanide resulted in the highest output. The cathode chamber place in the lower part, which does not require any light, and the open part is covered by a glass adequately glued to the chamber. The chambers that compose the main solid part of the chip can be fabricated using different methods, which allows more complex geometries but can be more time-consuming. Figure 1.11 shows a general schematic of the single-chip  $\mu$ -PSC

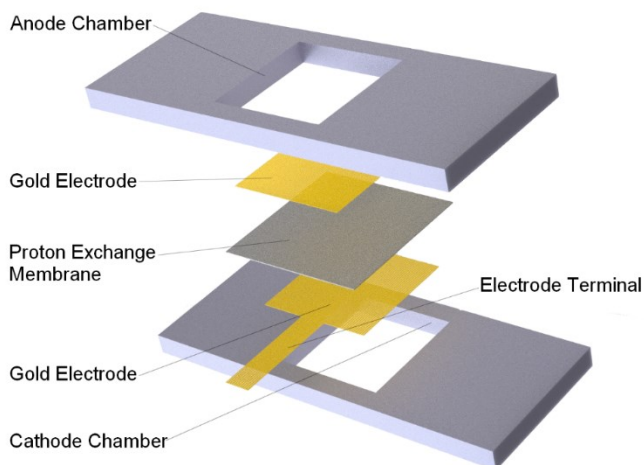


Figure 1.11 General schematic of the single-chip  $\mu$ -PSC device

The two chambers are separated by a proton exchange membrane (PEM), and the PEM material is Nafion 117, which is the same PEM used in fuel cell technology. Both sides of the PEM are uniformly covered with a patterned gold electrode that collects the free electrons and guides them into an external circuit for further measurements.

### 1.6.2. Operation Mechanism

The culture medium is the TAP media which forms a heterogeneous in which algae are suspended inside the solution. Tris-acetate-phosphate (TAP) medium can oxidize the NADP or NADPH and can be oxidized by electrons placed on each side of PEM[46].

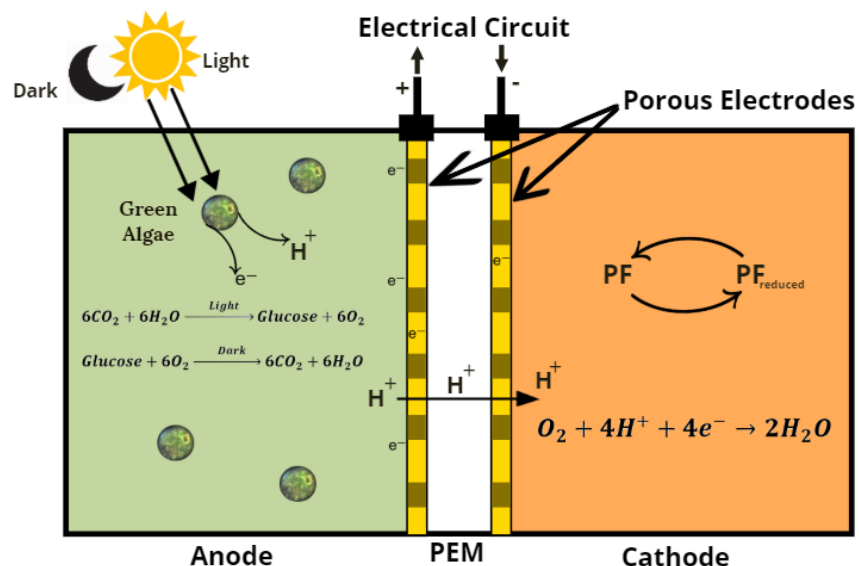


Figure 1.12 Principal of operation of the  $\mu$ -PSC

Figure 1.12 illustrates the overall reactions taking place in a  $\mu$ -PSC. The light photons are absorbed by the algal culture result in water molecules oxidization. This oxidization results in electron release. The released electrons are then transferred through the electron transfer chain and cause NADP and NADPH transformation. Moreover, these electrons are transferred to the cathode side using an external circuit. At the same time, photosynthesis causes a generation of hydrogen ions in the anode side. PEM is a membrane that allows positive ions (protons) to be transferred from the anode side to the cathode side[47].

The respiration starts when the system is kept in the dark condition. The process follows the light-independent reactions in which are also based on the electron transfer chain. In this process, the produced sugar in the photosynthesis process will be consumed. A part of produced energy is converted to electricity, letting the  $\mu$ -PSC function in light and dark conditions.

## **1.7. Thesis Motivation**

A sustainable future is a global concern that requires many practical actions. One aspect is to limit the use of fossil fuels due to their environmental pollution and limited resources. That is why the main focus on the current energy harvesting systems is on the development of clean energy harvesting systems. Photosynthetic-based micro energy harvesters or, more specifically, micro photosynthetic power cell ( $\mu$ -PSC) is the one that attracts the attention of the researchers.

So far, the  $\mu$ -PSC has been developed as a single-chip with considerable results. In order to obtain higher output voltage and current from the  $\mu$ -PSC device, multiple single chips were connected in series and parallel combinations. The current work is an attempt to develop the design, fabrication technique, and outputs verification of an arrayed  $\mu$ -PSC. Generally, there are two ways to design an array with multiple chambers for  $\mu$ -PSC. In one design, the chambers can be internally connected, and the other can consist of multiple independent chambers in one frame. In this study, the design and fabrication techniques for  $1\times 3$  chips of both the approaches have been developed, and the devices undergo experimental verifications. In addition, an improved model to predict the behavior of  $\mu$ -PSC is provided and verified with the single-chip  $\mu$ -PSC electrical output results. The model has also been verified for the arrayed  $\mu$ -PSC experimental results.

## **1.8. Thesis Objectives and Scopes**

This thesis aims to develop the design and fabrication of the arrayed  $\mu$ -PSC, which contains multiple  $\mu$ -PSC chips in one frame and utilizing algal photosynthetic cells to generate power. Two designs have been proposed, which are the interconnected array of  $\mu$ -PSC and the independently arrayed  $\mu$ -PSC. It is essential to consider the cost, simplicity of the fabrication, and device reusability for the final device compared to the previous designs for the single-chip PDMS-based  $\mu$ -PSC. The current thesis consists of five chapters, as explained below.

Chapter 1 discussed the need for energy in today's life and the development of  $\mu$ -PSC related technologies, and a comparison of their advantages and disadvantages are provided. The concepts of how photosynthesis and respiration work in an algal photosynthetic cell and how they related to the  $\mu$ -PSC technology are proposed. In the last part, the principle of operation of the  $\mu$ -PSC device is provided, and the recent research and developments in the field have been reviewed.

Chapter 2 provides the modeling of the  $\mu$ -PSC in COMSOL Multiphysics to predict the electrical behavior of  $\mu$ -PSC considering the geometrical aspects of the device, electrochemical reactions, and diffusion coefficient of the participating species in the system. The results will be validated with the experimental results of a fabricated single-chip  $\mu$ -PSC. The comparison between the predictions from the model shows good agreement with the experimental data.

Chapter 3 presents the designs and fabrication techniques of the interconnected array of  $\mu$ -PSC for the development of arrayed  $\mu$ -PSC. The interconnected array design consists of three chambers of  $\mu$ -PSC chips which are internally connected. The fabrication technique for the chip is explained, and the device undergoes testing to evaluate the system performance. The experimental results, including load current and load voltage, have been used to verify the developed model.

Chapter 4 discusses the design and developed fabrication technique of an independently arrayed  $\mu$ -PSC. The design consists of three  $\mu$ -PSC chips which are arrayed in one single frame. The fabricated chip has been tested for the characterization of its electrical parameters, including Open-Circuit Voltage (OCV), Short-Circuit Current (SCC), load voltage and load current variation, and power characterization. The model has been validated with the experimental data of the independently arrayed  $\mu$ -PSC.

Chapter 5 is the last chapter dedicated to the conclusion of findings and the potential future works.

## **1.9. Contributions**

Technical:

1. Fuel cell-based modeling of the Micro-Photosynthetic Power Cell
2. Development of the fabrication processes for the 1×3 array of Micro-Photosynthetic Power Cell
3. Testing and verification of the fabricated array designs

General:

1. Preparation of the Standard Operating Procedures (SOP) for maintaining the microalgae culture in laboratory and proton exchange membrane treatment with graduated Ph.D. student Kiran Kuruvinashetti

2. T. Payarou, S. Rahimi, K. Kuruvinashetti, P. Pillay and M. Packirisamy, "Detailed Electrochemical Model of Microphotosynthetic Power Cells," in *IEEE Transactions on Industry Applications*, vol. 57, no. 2, pp. 1703-1714, March-April 2021
3. K. Kuruvinashetti, S. Rahimi, Sh. Pakkiriswami, M. Packirisamy, "Economical and Simple Culturing Methods of Green Algae for Energy Harvesting from Photosynthesis under Microfluidic Environment" in *Current Protocols Essential Laboratory Techniques*, (Submitted in August 2021)
4. S. Rahimi, M. Packirisamy, "Design, Development, and Verification of an Interconnected Array Micro-Photosynthetic Power Cell" (To be submitted)
5. S. Rahimi, M. Packirisamy, "Design, Development, and Verification of an Independent Array of Micro-Photosynthetic Power Cell" (To be submitted)
6. S. Rahimi, K. Kuruvinashetti, M. Packirisamy, "Modeling and Validation of the Micro Photosynthetic Power Cell Harvesting from Blue-Green Algae" in *240th ECS Meeting in Orlando, Florida* (October 10-14, 2021) (Accepted and will be submitted to ECS journal)

## 2. Finite Element Analysis of the Micro-Photosynthetic Power Cell and Verification

### Abstract

The ever-growing need for energy is becoming an inevitable concern in today's life. Amongst various sources of new energy sources and, more specifically, energy harvesting systems, the biological-base energy harvesters have attracted attention within the past few years. The utilization of photosynthetic microorganisms as the heart of energy harvesting systems is a new technology which is still under development and study. Micro-photosynthetic power cell ( $\mu$ -PSC) is one such system that works based on the photosynthesis of living microalgae culture which has been under study for several years.

Micro-photosynthetic power cell is an electrochemical cell that produces electricity at micro-scale. During the light condition, a living microorganism culture that uses light, undergoes photosynthesis to consume carbon dioxide and water to generate electricity while during the dark conditions, the electrical power generates when the produced glucose undergoes respiration[29].

Same as the regular fuel cells,  $\mu$ -PSC consists of two chambers known as anode chamber and cathode chamber which are separated with a proton exchange membrane (PEM). PEM is responsible for transmitting positive hydrogen ions, more specifically protons to pass through from the anode side to the cathode side. On both sides of the membrane, patterned electrodes are placed to collect and transmit electrons which released during photosynthesis/respiration

In the anode chamber, living microalgae culture performs photosynthesis which results in the release of protons and electrons. The protons will be transferred through PEM from the anode side to the cathode side. On the other hand, the released electrons are collected by the electrodes and transferred through an external circuit for power generation. During the daytime, the cells do photosynthesis, and in dark conditions, they reverse the process, also known as respiration. The electrons will be released during both processes.

On the cathode side, the electrons will reduce the catholyte which is Potassium Ferricyanide to Potassium Ferrocyanide. At the same time, the transferred protons will oxidize back the reduced

catholyte and with their combination with oxygen, water will be released. More specified reactions are discussed in the following sections.

There are several advantages in implementing  $\mu$ -PSC over other conventional energy harvesting systems including photovoltaic power cells.  $\mu$ -PSC technology is cleaner than many other energy harvesting systems because it uses biological organisms as the main energy source. Moreover,  $\mu$ -PSC can operate in both light and dark condition which makes it a reliable source for low-power applications and sensors which requires a continuous power supply.

This chapter will discuss the modeling of the  $\mu$ -PSC using COMSOL Multiphysics in a similar way as with the general fuel cell operating concepts. This modeling considers the electrochemical aspects of the chemical species while considering the geometrical aspect of the  $\mu$ -PSC device. The geometrical parameters have been obtained from the actual device that has been used for experimental purposes. The simulation is based on the reduction and oxidation of algal species, concentration and mole fraction of the species, and the respective number of transferred electrons within the electrochemical reactions. The model is capable of predicting the polarization curve and power characterization of the  $\mu$ -PSC in a time-independent domain, considering the electrochemical kinetics and polarization losses, including concentration, ohmic, and activation losses.

In order to evaluate the performance of this simulation, the outputs have been compared with the experimental data at various configurations including different surface areas. In addition, the effect of internal resistance and temperature variation effect on the performance of the  $\mu$ -PSC have also been predicted.

## **2.1. Introduction**

Micro photosynthetic power cells ( $\mu$ -PSC) are a growing environmentally friendly technology for power generation. Their capability of functioning in both light and dark conditions makes them a proper candidate for the next generations of IoT micro sensors power supply[48] and mobile microelectrochemical systems. Various parameters affect both the functionality and performance

of the  $\mu$ -PSC, including the chamber's temperature, active surface area, the internal resistance of the device, etc.

The very first studies on the  $\mu$ -PSC related technology have been initiated in the early 1900s. Recent studies show more interest in developing  $\mu$ -PSC technology using various types of materials, microorganisms[49], and membranes[22]. In addition to the experimental aspect in the development of the  $\mu$ -PSC, many works focused on the modeling and performance prediction of the  $\mu$ -PSC device based on different models[25], [50].

The main focus on the modeling aspect of the  $\mu$ -PSC is the modeling of the electrochemical and physical phenomena that happen. Electrochemical phenomena are being described by the kinetic equation such as the Butler-Volmer equation. In order to validate the results from the model, they need to be compared with the experimental data as in[51], [52]. The results from the modeling can help understand how the change in some parameters can affect the performance of the  $\mu$ -PSC. In [25], an electrochemical modeling and equivalence electrical circuit have been provided based on the electrochemical kinetics of the system. The results show a relatively low error value for the polarization curve with the Short Circuit Current (SCC) value of 820 $\mu$ A and 870mV for the Open-Circuit Voltage (OCV). Moreover, the peak power showed to be 179.36  $\mu$ W which at the current of 459 $\mu$ A. In addition, the effect of temperature variation and internal resistance at different values have also been provided. In [53], develop a model to predict the effect of irradiance, day and light cycle, temperature, and media pH on the performance of the  $\mu$ -PSC. Different dc-dc converters have also been designed and evaluated with MATLAB/Simulink. The experimental results have also been provided to evaluate the model outputs. The value for the experimental and predicted open-circuit voltage was reported as 0.89 V and 0.909 V and the short-circuit current of 896  $\mu$ A and 899  $\mu$ A.

The biological organism which works as the primary part of  $\mu$ -PSC in this research is the microalgae culture *Chlamydomonas reinhardtii* which is widely implemented in the research of photosynthesis[54]. This strain of algae is best performing in the temperature range of 21°C to 25°C. High or low temperature can also damage the cells. The effect of temperature on the performance of  $\mu$ -PSC considering the equivalent electrochemical phenomena happening in the device is predicted in [25] and also stated in [55].

This chapter mainly focuses on the simulation of the single  $\mu$ -PSC device using COMSOL Multiphysics to simulate the electrochemical phenomena happening in the device in a time-independent domain. The simulation provides the possibility of predicting the effect of geometrical properties of the  $\mu$ -PSC device including active surface area. The target outputs include the polarization curve or I-V characteristics of the device which has been predicted by the model. In addition, the power curve provides the peak value at which the device can work. The effect of temperature and internal resistance has also been provided. The modeling results have also been validated with the experimental results of the chip with the same configuration.

## 2.2. $\mu$ -PSC Operation Principles

Micro-photosynthetic power cell ( $\mu$ -PSC) is an electrochemical cell that produces electricity at micro-scale. During the light condition, a living microorganism culture uses light to consume carbon dioxide and water to perform photosynthesis, and during the dark condition, the produced carbohydrate undergoes respiration with the help of oxygen. The electrons are released during photosynthesis/respiration and are siphoned to generate electricity. This is one of the main advantages of  $\mu$ -PSC over a photovoltaic cell that  $\mu$ -PSC is able to generate power under light and dark conditions [29].

Figure 2.1 provides a general schematic of the operation of  $\mu$ -PSC. The system consists of the anode chamber and cathode chamber which are separated by the proton exchange membrane (PEM). The two sides of PEM are covered by patterned electrodes. PEM only allows protons to be transmitted from the anode side to the cathode side. The electrodes are responsible for capturing electrons and transmitting them through an external circuit for power generation.

In the anode chamber, microalgae culture undergoes photosynthesis in the presence of light in which electrons and protons release. The protons transmit from the anode chamber to the cathode chamber through the PEM. At the same time, the electrodes will collect the released electrons and transmit them through an external circuit for power generation

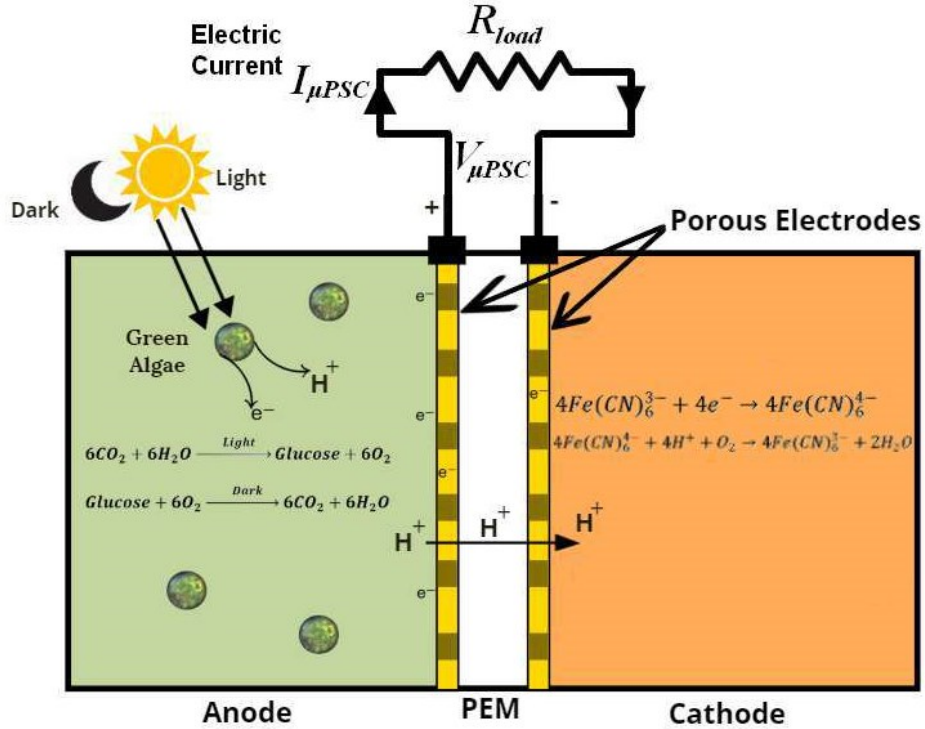
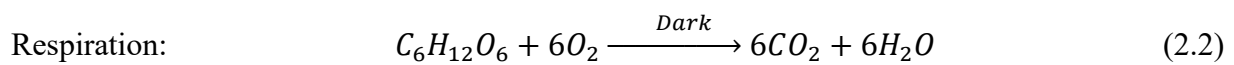
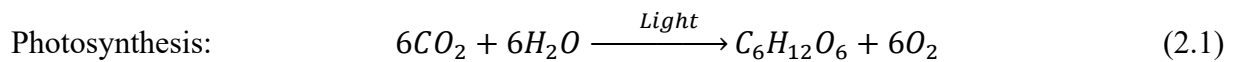


Figure 2.1  $\mu$ -PSC principle of operation

During the daytime, the cells perform photosynthesis in which consume carbon dioxide and produce carbohydrate and oxygen as the products. In dark conditions, they reverse the process also known as respiration, in which the produced sugar will be consumed along with oxygen and carbon dioxide will be produced. Electrons will be released during both the process



In the cathode chamber, Potassium Ferricyanide, which works as the electron acceptor, will be reduced by the electrons to Potassium Ferrocyanide. Potassium Ferrocyanide will oxidize back to Potassium Ferricyanide by the protons which pass through the PEM. The combination of protons and oxygen will result in the production of water. More specified reactions are discussed in the following sections.

### 2.3. Implementation of Micro-Photosynthetic Power Cell Model Analysis in COMSOL Multiphysics

The operation of  $\mu$ -PSC includes a system with multiple physics. It includes biological organisms which go through a chain of complex reactions to perform photosynthesis. During these reactions, electrons are released, which are used for power generation in the  $\mu$ -PSC. The electrical behavior of the system also follows certain rules in electrochemical kinetics.

In the current model, the electrochemical kinetic formulations are considered to measure the electrical phenomena as polarization curve (Current-Voltage or I-V characteristics) and potential drops/losses. In addition, the transport phenomena formulations which help to calculate the transports in electrochemical reactions are included. COMSOL Multiphysics is specifically designed for the analysis of such systems by providing the possibility of coupling multiple physics together. The model is developed with the coupling of two domains which are “*Secondary Current Distribution*” for kinetics equations and “*Transport of Concentrated species*” for chemical component analysis. In this chapter, the governing equations, geometry, assumption, major parameters, and mesh configuration are discussed. For ease of understanding, Figure 2.2 provides a flowchart that the numerical model follows to predict the electrical behavior of the model.

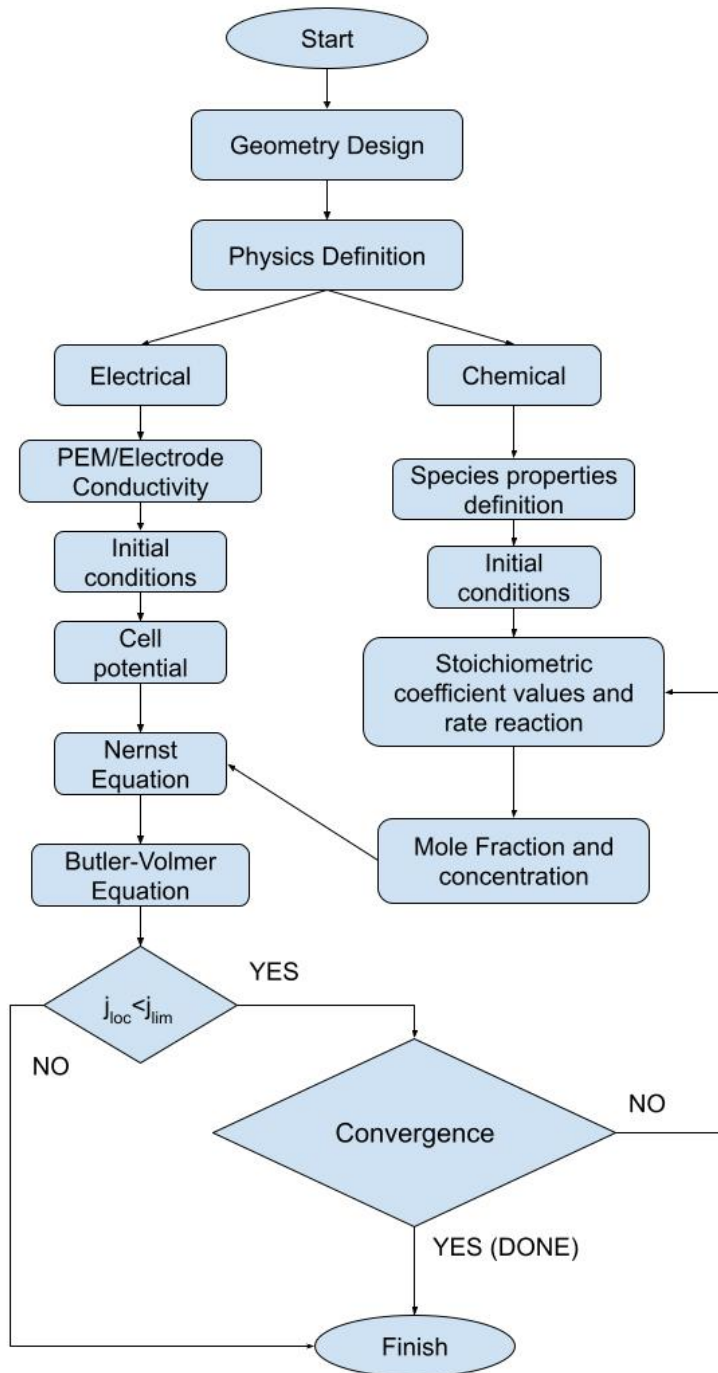


Figure 2.2 Flowchart of the numerical analysis procedure in COMSOL Multiphysics

## 2.3.1. Governing Equations

### 2.3.1.1. Electrical Modeling

The general form of the polarization curve for fuel cell-related technologies, including microbial fuel cells and micro-photosynthesis power cell consists of several stages in which different types of voltage losses occur. The relation between  $\mu$ -PSC voltage and current can be described by the following equation[17], [56], [57]:

$$V_{\mu PSC} = I_{\mu PSC} R_{Load} = E_0 - V_{act} - V_{conc} - V_{ohmic} \quad (2.3)$$

Where  $I_{\mu PSC}$  is the cell current,  $E_0$  is the Nernst reversible voltage which is also known as ideal open-circuit voltage (OCV),  $V_{act}$  is the activation potential barrier,  $V_{conc}$  is the concentration potential loss and  $V_{ohmic}$  is the ohmic potential loss[25]. Figure 2.3 provides a schematic of the polarization curve considering the voltage losses.

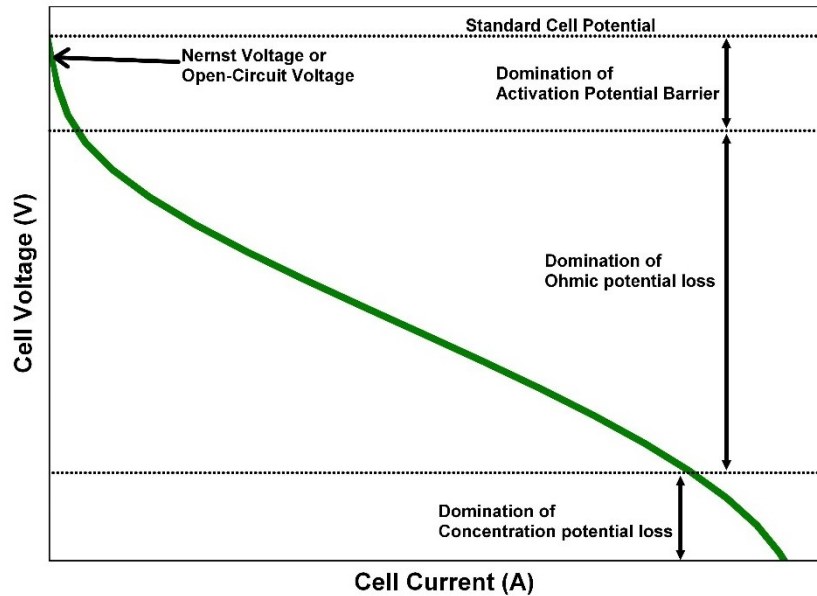


Figure 2.3 General polarization curve and the voltage loss domains

The change in system energy can be evaluated by the chemical components and chemical reactions occurring in the system and can be expressed in terms of Gibbs free energy with the unit of joules (J)[17]:

$$\Delta G = \Delta G^0 + RT \ln(\Pi) \quad (2.4)$$

In the above equation,  $\Delta G$  is the Gibbs free energy change,  $\Delta G^0$  is the Gibbs free energy in the standard condition where the temperature is 298.15 K, pressure is 1 atm, and the concentration of all the species are 1M.  $R$  is the universal gas constant (8.31447 J/mol.K), and  $T$  is the operating temperature in (K).  $\Pi$  is the reaction quotient which shows the chemical activity ratio of products over the reactants raised by their stoichiometric coefficients ( $p$  for products and  $r$  for reactants). It can be shown as[17]:

$$\Pi = \frac{[products]^p}{[reactants]^r} \quad (2.5)$$

It is more common to analyze the reactions in terms of cell electromotive force (EMF) or  $E_0$  in which the Gibbs free energy can be written as the multiplication of electromotive force and electron charge transfer ( $Q$ ). The electron charge transfer is the total number of electrons that transferred in the reaction and can be written as the multiplication of the  $n$ , which is the number of exchanged electrons (mol) in the reaction and Faraday constant ( $F = 96486$  C/mol)[17]:

$$-\Delta G = E_0 Q \quad (2.6)$$

$$E_0 = \frac{-\Delta G}{nF} \quad (2.7)$$

Accordingly, considering the standard condition, standard Gibbs free energy can be written as:

$$E_{cell}^0 = \frac{-\Delta G^0}{nF} \quad (2.8)$$

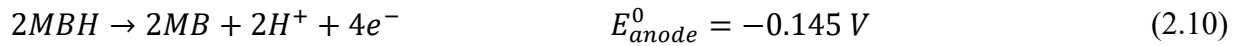
The  $E_{cell}^0$  is also known as standard cell electromotive force, which is the maximum potential difference between two electrodes or Open-Circuit Voltage (OCV). By replacing equations 2.7 and 2.8 into equation 2.4, Nernst reversible voltage can be estimated as follows[17]:

$$E_0 \approx E_{Nernst} = E_{cell}^0 - \frac{RT}{nF} \ln(\Pi) \quad (2.9)$$

The parameters that affect in the reaction quotient ( $\Pi$ ) are dependent on the concentration of the species which contribute to the electrochemical reactions. Due to the presence of living biological organisms in the  $\mu$ -PSC, the complex reactions that occur in the process of photosynthesis. It is hard to model the real occurring phenomena due to the complex dynamics of the microalgae

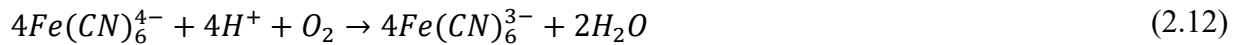
culture and photosynthesis reactions. Thus, the current model uses a reduction-oxidation (redox) reaction of a redox coupler known as Methylene blue which has been used in the previous models for  $\mu$ -PSC[25], [53], [58], [59]. Methylene blue also works as an electron mediator which can reduce the electrons from the oxidation between NADH and  $\text{NAD}^+$  in the photosynthesis process. This material provides a similar chemical potential as with the microalgae culture in the  $\mu$ -PSC. To effectively model the  $\mu$ -PSC, the reactions are simplified to one reaction in the anode chamber that releases the electrons and protons and one reaction in the cathode chamber that consumes the electrons and protons.

Accordingly, the reaction in the anode chamber is replaced by the oxidation of reduced Methylene blue (*MBH*) to Methylene blue (*MB*). The overall reaction in the anode chamber can be written as[59]:

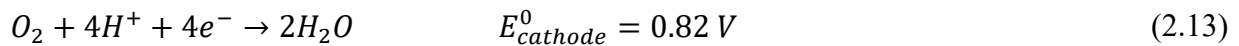


Equation (2.10) is the reaction that occurs in the anode chamber of the model. The standard electrochemical potential ( $E_{anode}^0$ ) of the half-reaction (2.8) has been calculated to be -0.145 V[59].

In the cathode chamber, Potassium Ferricyanide intakes electrons and reduces to Potassium Ferrocyanide. Next, it will oxidize back to Potassium Ferricyanide due to the presence of protons and oxygen and the water will be released. The overall reactions taking place in the cathode chamber of the  $\mu$ -PSC are as follows:



Accordingly, the overall reaction in the cathode chamber can be written by the summation of the Equations (2.11) and (2.12) which is the generation of water.



Equation (2.13) is the reaction that occurs in the cathode chamber of the model. The standard electrochemical potential ( $E_{cathode}^0$ ) of this half-reaction has been measured to be 0.82V[17]. The standard cell electromotive force  $E_{cell}^0$  for the model of  $\mu$ -PSC can be calculated as the difference between the potential of the anode and cathode side as:

$$E_{cell}^0 = E_{cathode}^0 - E_{anode}^0 \quad (2.14)$$

The total cell potential can be calculated from Equation (2.14) as the difference between the potential of the anode and cathode side which approximates the total  $\mu$ -PSC potential to be 0.965 V[25].

Activation potential drop is a part of voltage that is required to get the electrochemical reaction to overcome the energy barrier near electrode-PEM surfaces. The behavior of this zone in the polarization curve can be represented by different kinetic models. One of the comprehensive kinetic model for describing this phenomenon is the Butler-Volmer equation[25]:

$$I_{\mu PSC} = A_s j_{loc} = A_s j_0 \left( \exp\left(\frac{\alpha_{Red} F V_{act}}{RT}\right) - \exp\left(-\frac{\alpha_{Ox} F V_{act}}{RT}\right) \right) \quad (2.15)$$

Where

- $A_s$  ( $m^2$ ) is the area of the electrode surface, which is  $484mm^2$
- $j_{loc}$  is the local current density of the model, which will be calculated at the interface of the electrode and PEM
- $j_0$  is the equilibrium exchange current density which is a measure of readiness of the electrode to proceed with the chemical reaction. The higher the  $i_0$  is, the lower the barrier will be for the electrons to overcome. For this model, the value is equal to  $10^{-8} A/cm^2$ [25]
- $\alpha_{Red}$  and  $\alpha_{Ox}$  is the unitless parameter which describes a charge transfer coefficient in the reduction/oxidation reactions in anode chamber and cathode chamber. From previous models, both are estimated to be equally 0.5[25]. The sum of these two should be equal to one.
- $F$  is Faraday's constant and describe the amount of charge per unit mole and is  $96486 C/mol$
- $R$  is the universal gas constant and is equal to  $8.31447 J/mol.K$
- $T$  is the working temperature of the system which is  $298.15 K$

- $V_{act}$  is the activation potential drop

Another phenomenon that affects the shape of the polarization curve is known as concentration loss which is associated with the concentration of reacting components (e.g.,  $MBH$  in anode chamber and  $O_2$  in the cathode chamber of the model) near the electrode surface ( $C_i$ ) where reactions occur, and the concentration of components in the bulk region ( $C_b$ ) which is the region far from the electrode surface in each of the chambers. In the anode chamber of the  $\mu$ -PSC model, at high current density, more charge is being transferred. More charge transfer leads to the decrease in the concentration of reacting species near the electrode surface and causes a drop in the system performance. Generally, it can be described by[56]:

$$V_{conc} = \frac{-RT}{nF} \ln \left( \frac{C_i}{C_b} \right) \quad (2.16)$$

The decrease in  $C_i$  continues until the concentration near the electrode surface falls to zero. This is the point where the system cannot generate more current. The maximum current that can be generated by the system is known as limiting current density ( $j_{lim}$ ).

In the model, the effect of concentration losses which are associated with the concentration of species near the electrode surface ( $C_i$ ) and the concentration of species in the bulk region ( $C_b$ ), did not included in the formulation based on the species concentrations. Instead, it has been included by the Koutecký–Levich equation[60]. According to this equation, the effect of limiting current density has been included by measuring the local current in the model at the interface of electrode and PEM in the absence of concentration loss ( $j_k$ ) and adding limiting current density through Equation 2.17. It is worth noting that the equation only works for the  $i_k$  lower than  $i_{lim}$ .

$$j_{loc} = \frac{j_k}{1 + \left| \frac{j_k}{j_{lim}} \right|} \quad (2.17)$$

The other factor in the modeling of the  $\mu$ -PSC polarization curve is the ohmic loss which is associated with the resistance confronting the proton and electrons to be transferred. Generally, the formulation of this phenomena can be summarized as the multiplication of  $\mu$ -PSC device internal resistance and cell current as below

$$V_{ohmic} = A_s j_{loc} R_{int} = A_s j_{loc} (R_{electrons} + R_{protons}) \quad (2.18)$$

To be more specific, the ohmic loss can be divided into three terms as follows:

$$R_{int} = R_{anode\ electrode} + R_{PEM} + R_{cathode\ electrode} \quad (2.19)$$

The Ohmic loss is mostly associated with the resistance of the proton exchange membrane (PEM). With the increase in PEM active surface area ( $A_s$ ), there will be more active area for the protons to be transferred which leads to the decrease in PEM resistance. On the other hand, with the increase in proton exchange membrane thickness ( $\delta_{PEM}$ ), protons need to move further inside the PEM membrane which acts as an additional resistance toward their movement. The last parameter is the PEM conductivity which has an inverse relation with the resistance of the PEM. Thus, Equation (2.19) can be simplified to PEM resistance term. Accordingly, The ohmic loss can be written as[56]:

$$V_{ohmic} = A_s j_{loc} R_{int} = j_{loc} A_s \left( \frac{\delta_{PEM}}{A_s \sigma_{PEM}} \right) = j_{loc} \frac{\delta_{PEM}}{\sigma_{PEM}} \quad (2.20)$$

### 2.3.1.2. Chemical Reaction Modeling

Conceptually,  $\mu$ -PSC follows similar phenomena as with the different types of PEM fuel cells and Microbial fuel cells. This consists of several electrochemical/bioelectrochemical reactions. These reactions and half-cell reactions include electron transport chain and mass transport which are the main reasons for power generation. Negative charges are generated as electrons and positive ions are released as positive hydrogen ions (proton) as a result of reactions taking place in the anode chamber. Electrons are collected by conductive electrodes and transferred through an external circuit for electrical power generation. Then they will transfer to the cathode side for the completion of electrochemical/bioelectrochemical reaction. At the same time, positive ions pass through the proton exchange membrane through a mass transport phenomenon to the cathode chamber.

In order to model the chemical reactions in Equations (2.10) and (2.13), the species, which are the reduced Methylene Blue (MBH) in the anode chamber and oxygen and water in the cathode

chamber, and their respective reactions need to be considered. In the actual  $\mu$ -PSC, the species would be the chemical components that contribute to the act of photosynthesis of the microalgae culture in the anode chamber, including oxygen, carbon dioxide, water, carbohydrate, nutrient sources etc. In the cathode chamber, the species would be the reduction/oxidation of Potassium Ferricyanide and oxygen. In the case of modeling, the species that include in the anode chamber is Methylene Blue, and the species in the cathode chamber are oxygen and water.

In the cathode chamber, it would be Equations (2.11) and (2.12). For the purpose of this modeling, Equation (2.10) is occurring in the anode chamber, and Equation (2.13) is occurring in the cathode chamber.

The governing equation in COMSOL Multiphysics for a reacting flow which consists of a mixture with multiple species, which in actual  $\mu$ -PSC are algal cell and nutrient sources in anode chamber and Potassium Ferricyanide, oxygen and water in cathode chamber, and multiple, which in actual  $\mu$ -PSC are photosynthetic reactions in anode chamber and Equation (2.11) and (2.12) in the cathode chamber. The below equation describes the mass transport for an individual species[61], [62]:

$$\frac{\partial}{\partial t}(\rho_i) + \nabla \cdot (\rho_i u) + \nabla \cdot j_i = R_i \quad (2.21)$$

On the left side of Equation (2.21), the first term describes the density ( $\rho$ ) change of  $i^{th}$  species over time, the second term shows the flux of  $i^{th}$  species that is carried by reference velocity of  $u$ , and the third term is the diffusion flux ( $j_i$ ) of  $i^{th}$  species which relate to the gradients that affect the diffusion of species including temperature, pressure, etc. According to the conservation of mass, the summation of mentioned three terms should be equal to the production or consumption of the  $i^{th}$  species. This variable is shown with  $R_i$ , which is known as reaction rate.

In order to properly implement Equation (2.21) for the modeling of  $\mu$ -PSC, the analysis has been done in a time-independent domain (stationary study). Moreover, the  $\mu$ -PSC does not include an inlet/outlet, which leads to a velocity of zero. Thus, Equation (2.21) can be written as:

$$\nabla \cdot j_i = R_i \quad (2.22)$$

Diffusion flux can be described by the Maxwell-Stefan diffusion model[63] for a multicomponent system. It provides the possibility of relating the diffusion of species to the  $\mu$ -PSC potential. The model includes the parameters that can affect the diffusion of a multi-species system, including temperature gradients, the diffusive force between every two species, the pressure gradient and external forces by the presence of an electric field. The  $\mu$ -PSC does not include temperature change as it functions at constant room temperature. Moreover, it does not undergo pressure gradients or external electric fields. In addition, due to the simplified reactions and limited species in the model, the diffusion coefficient is considered constant in cathode and anode chambers. Thus, for the current model, the simplified form of the Maxwell-Stefan equation is as follows:

$$j_i = -\rho_i D \sum_{k=1}^Q \nabla x_k \quad (2.23)$$

Where

- $D$  (m<sup>2</sup>/s) is the diffusion coefficient
- $x_k$  is the mole fraction of  $k^{th}$  species
- $\rho_i$ (kg/m<sup>3</sup>) is the density of  $i^{th}$  species

The reaction rate ( $R_i$ ) can be defined by the oxidation/reduction reactions which occur in the anode chamber and cathode chambers. The overall reaction that occurs in each chamber can be denoted as follow[61]:



In the model, the stoichiometric coefficient  $\nu_{red}$  and  $\nu_{ox}$  with  $\nu$  being positive for products and negative for the reactants, can be defined from the oxidation/reduction reactions of Equations (2.10) and (2.13). Also,  $n$  is the number of participating electrons. In an electrochemical reaction, the rate of reaction can be calculated by the transferred charges. In other words, the rate of reaction can be extracted for the output current (modeled by electrochemical equations: Nernst voltage and Butler-Volmer equations)[60]:

$$R_i = \frac{v_i j_{loc}}{nF} \quad (2.25)$$

The variable  $v_i$  is the stoichiometric coefficient of the  $i^{th}$  species. The  $j_{loc}$  is the calculated current density of the model,  $n$  is the number of participating electrons and  $F$  is the Faraday's constant. For this model, on the anode side, it takes the stoichiometric coefficient of *MBH*, and on the cathode side, it takes the stoichiometric coefficient of oxygen and water. The  $j_{loc}$  is the coupled parameter between the electrical and electrochemical equations. Given the above relations and equations, it is possible to use the chemical reactions and proceed with the modeling.

The boundary condition which are applied to the model are shown in the schematic of Figure 2.4. The outer boundary of the MEA is electrically insulated. (a) is the zero species flux which is applied to the walls of the geometry of each chamber. The properties of materials, including mold fraction and temperature, are defined in (b) for the anode chamber and in (c) for the cathode chamber. (d) is where the electrical modeling in section 2.3.1.1 is applied. (f) defines the cell voltage (potential) and is the boundary of the reaction rate calculation. (e) defines the electrical ground, which is defined relative to the value in (f). Moreover, the rate reaction in the anode side is calculated at the boundary (e).

The introduced equations and procedure can be used to measure the local current density  $j_{loc}$  by integrating the final  $j_{loc}$  at the boundary of the electrode and PEM as provided in Figure 2.4. The variation of  $j_{loc}$  can be obtained through the parametric study over the cell voltage. In order to obtain the cell current, the integrated local current density  $j_{loc}$ , can be multiplied by the 22mm.

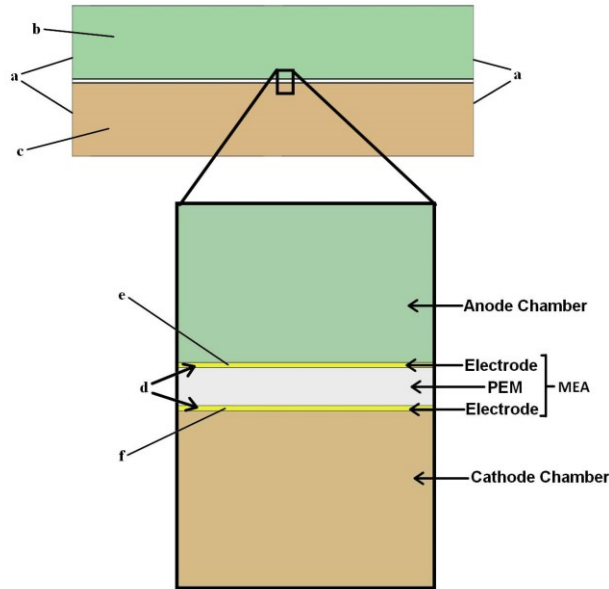


Figure 2.4 Boundary conditions of the  $\mu$ -PSC model

### 2.4.2. Model Geometry

The micro photosynthetic power cell model provides the simulation using the actual dimensions of the fabricated  $\mu$ -PSC. The length of all components is equal to the active surface area of the actual cell, which is 22mm. The width of each part also follows the same dimensions as the actual device, which is provided in Table 2.1. Figure 2.5 provides the geometry that has been used in this simulation. The red lines are assigned as the wall. The dimensions are presented in Table 2.1 and the model geometry is presented in Figure 2.5.

Table 2.1 Geometrical specifications for the  $\mu$ -PSC model

Parameter	Value
Chamber Length (L)	22mm
Chamber Width (W)	22mm
Chamber thickness	4mm
Electrode thickness	25 $\mu$ m

PEM thickness	183um
Active Surface Area ( $A=L \times W$ )	22mm $\times$ 22mm

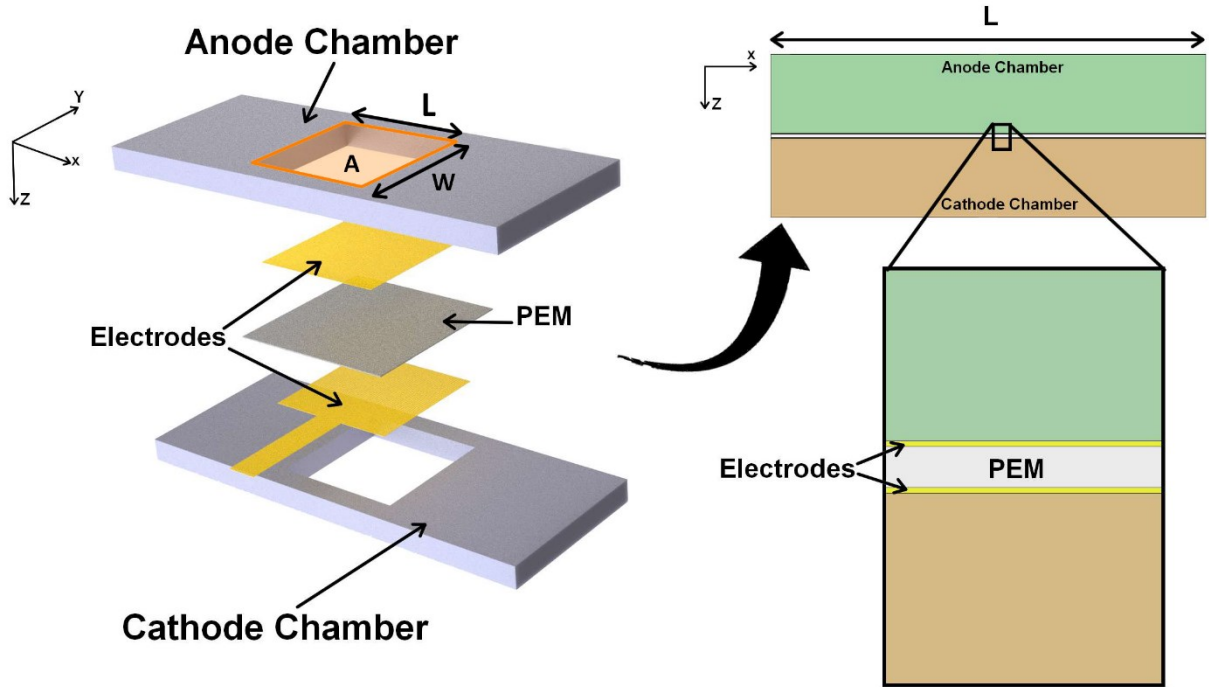


Figure 2.5 geometry of the  $\mu$ -PSC model

### 2.4.3. Assumptions

- Modeling the actual  $\mu$ -PSC power cell is very complex due to several reasons. The main component in the  $\mu$ -PSC power cell is living microorganisms which leads to the generation of power in  $\mu$ -PSC through the process of photosynthesis which is a series of complex biochemical reactions, and modeling the exact process is out the scope of this chapter. For the research, according to the studies, a redox coupler with a chemical potential similar to the microorganism culture is used for this modeling to reduce the numerical computation.
- The components that are available in the actual  $\mu$ -PSC consist of different chemicals and elements which are being used as the nutrition source for microalgae which are not included in the modeling.
- The modeling has been done in a cross-sectional space which provides the assumption that all the properties in the horizontal direction (y-direction) are homogeneous.

- The diffusion coefficient of the included materials inside the model, which are reduced Methylene Blue (*MBH*) in the anode chamber and oxygen and water in the cathode chamber, is assumed to be constant and not related to media properties[64].
- The modeling is being performed in the time-independent domain (stationary study).
- It is assumed that the components are properly mixed and uniformly distributed and there is no initial concentration gradient in anode and cathode chambers
- The temperature gradient is also assumed to be zero.

#### 2.4.4. Parameters and Constants

The constants and related material properties, including PEM conductivity, Effective charge transfer coefficient, etc. values have been obtained from Masadeh et al.[25] on the mathematical modeling of the  $\mu$ -PSC device and are available in Table 2.2.

Table 2.2  $\mu$ -PSC Model parameters

Symbol	Description	Value
$R$	Universal gas constant	8.31447 J/mol.K
$T$	Operating temperature	298.15 K
$F$	Faraday's constant	96486 C/mol
$n$	Number of transferred electrons	4[53]
$i_0$	Equilibrium exchange current density	$2 \times 10^{-4}$ A/m <sup>2</sup> [56]
$i_L$	Limiting current density	1.818 A/m <sup>2</sup> [25]
$\sigma_a$	Anode electrode conductivity	$4.42 \times 10^8$ S/m
$\sigma_c$	Cathode electrode conductivity	$4.42 \times 10^8$ S/m
$\sigma_e$	Membrane conductivity	10 S/m
$\alpha_a$	Anode effective charge transfer coefficient	0.5[25]
$\alpha_c$	Cathode effective charge transfer coefficient	0.5[25]
$R_{int}$	Internal resistance	599 $\Omega$ [55]
$D$	Diffusion coefficient	$1 \times 10^{-5}$ m <sup>2</sup> /s
$\varepsilon$	Electrode's porosity	0.6
$X_a$	Anolyte mole fraction	0.14[53]
$X_c$	Catholyte mole fraction	0.97[53]

$M_{MBH}$	Molar mass of reduced Methylene Blue	321 gr/mol
$M_{water}$	Molar mass of water	18 gr/mol
$M_{oxygen}$	Molar mass of oxygen	32 gr/mol
$\rho$	Mixture density	1000 kg/m <sup>3</sup>

### 2.4.5. Mesh Configuration

For this model, a structured quad with a minimum element size of 0.0165mm has been used. The total number of mesh that has been used in this modeling is 100393, with an average element quality of 0.9. Different mesh size has been tested and the observation shows no specific change on the output results. In the case of adding parameters with gradients, e.g., the local concentration of the species or inlet/outlet, the mesh may be needed to be reconstructed to provide more exact information on the velocity, pressure, etc.

## 2.5. Modeling Results

In this section, the results from the modeling have been provided. The focus would be on the variation of cell voltage versus cell current and, respectively, the variation of cell power over cell current at various loading. Moreover, the effect of some main parameters which can affect the performance of the device has been predicted, including operating temperature, internal resistance, and surface area.

In order to compare the prediction results in various configurations, the Fill Factor is calculated, which is the measure for the quality of the power generating device. It can be calculated by the ratio of maximum power which happens at the voltage of  $V_{MP}$  and the current of  $I_{MP}$  in the normalized I-V characteristics plot over the multiplication of open-circuit voltage of  $V_{OC}$  and short-circuits current of  $I_{SC}$  as provided in Equation (2.26). The overall view of the fill factor is also provided in Figure 2.6.

$$Fill\ Factor\ (FF) = \frac{I_{MP} \times V_{MP}}{I_{SC} \times V_{OC}} \quad (2.26)$$

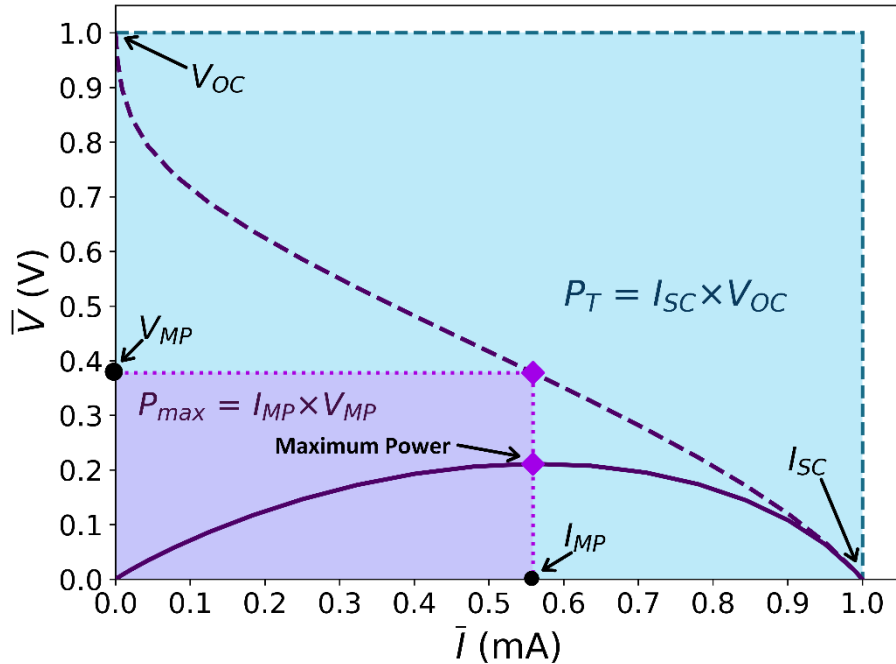


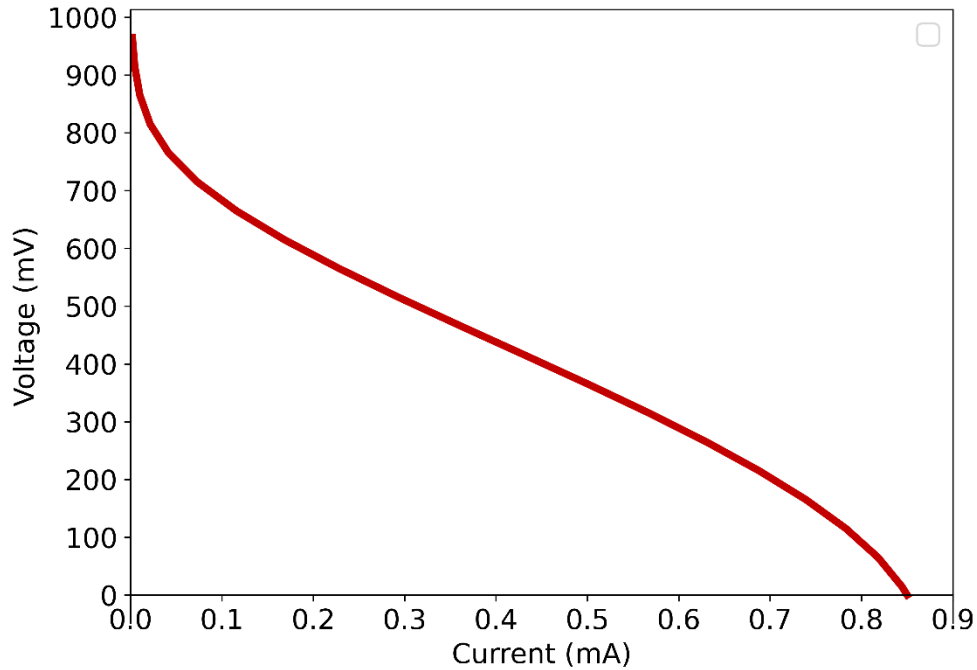
Figure 2.6 Overall view of Fill Factor Calculation

### 2.5.1. I-V Characteristics and Power Curve

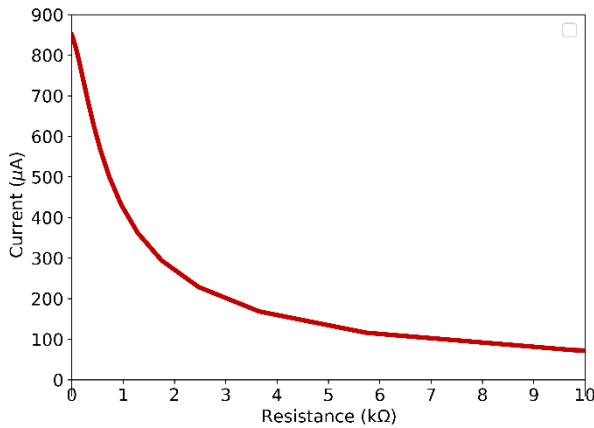
The voltage-current behavior which also known as the polarization curve provides valuable information on the power-generation behavior of the  $\mu$ -PSC. In the current modeling, the focus will be on this curve. Moreover, this curve can be helpful in electrical modeling and designing of power converters.

Figure 2.7 shows the prediction of the electrical behavior of a 22mm  $\mu$ -PSC chip. According to Figure 2.7 (a), the maximum voltage shows the value 0.965 V, which is the theoretical cell maximum potential. With the decrease in cell voltage, the current starts increasing by a pattern explained in section 2.3. Until about the current equal to 0.1 mA, the behavior is more subjected to activation losses. After that, the effect of ohmic losses dominates and leads to an almost linear variation of voltage and current. In the last region which starts at the current of about 0.7mA, the cell is more subjected to concentration losses which shows a steeper slope until reaching the maximum current at about 0.85 mA. In Figure 2.7 (b) and (c), the variation of cell current and cell voltage at various resistance is portrayed. Accordingly, as with the theory, with the increase of resistance, it is expected that the current starts decreasing and the cell voltage to increase. Figure 2.7 (d) shows the variation of cell power over the cell current. The model predicts that the

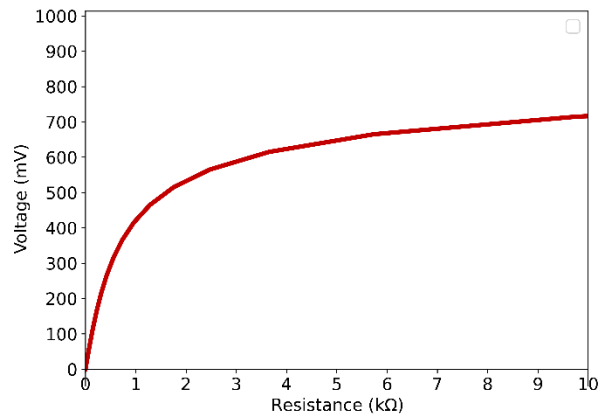
maximum power has could have the value of about 0.18 mW at the current of about 0.5 mA. Figure 2.7 (e) shows the variation of cell power at various resistance. It is predicted that the maximum power may be obtained at the resistance of about 800  $\Omega$ , and it starts decreasing with the increase in resistance.



(a)



(b)



(c)

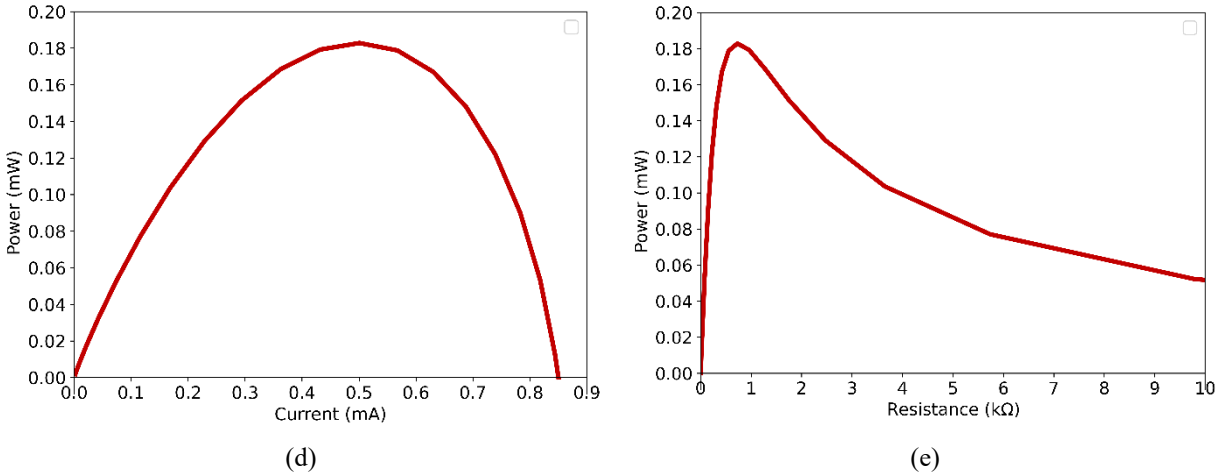
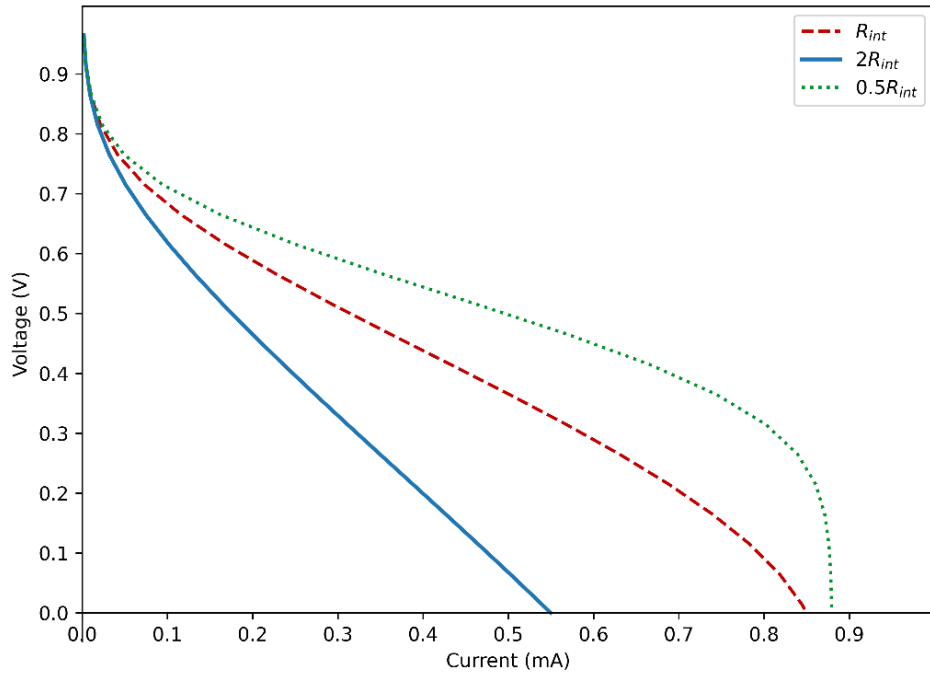


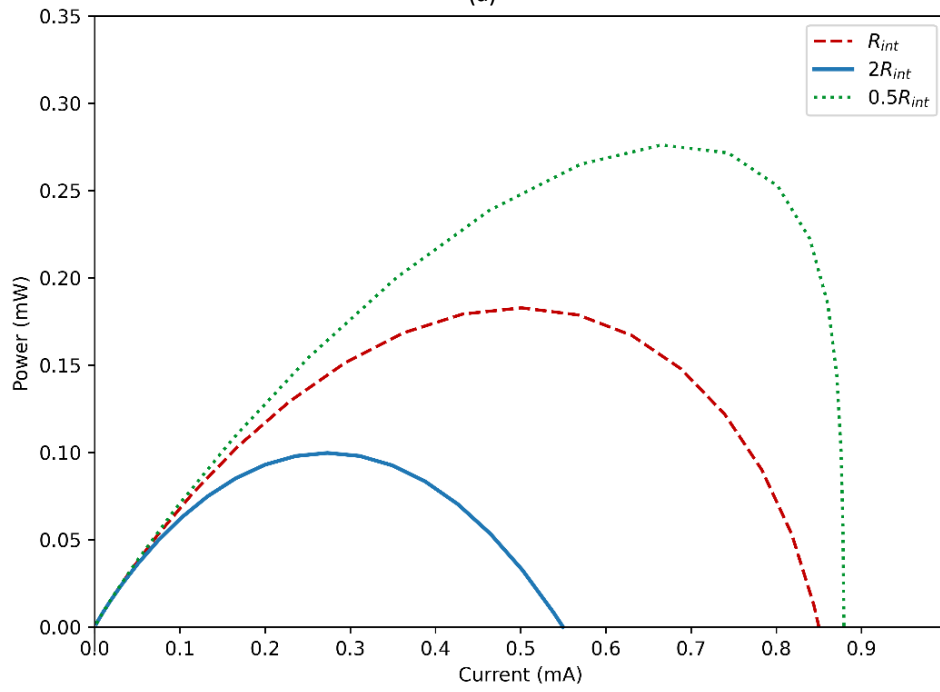
Figure 2.7 Predicted performance of the 22mm  $\mu$ -PSC chip for (a) voltage-current variation, (b) current variation over resistance change, (c) voltage variation over resistance change, (d) power-current variation and (e) power variation over resistance change

### 2.5.2. Effect of Internal Resistance

In order to evaluate the effectiveness of the developed model, A change in the internal resistance has been implemented. Theoretically, the internal resistance is mostly due to the resistance in the proton exchange membrane against proton transfer which is estimated by Equation (2.20). Higher internal resistance results in more ohmic losses. Figure 2.8 illustrates the effect of PEM thickness on the load voltage and load current variation. Following Equation (2.20), the polarization curve and power curve for various internal resistances are proposed in Figures 2.8 and 2.9. According to the Figure, lower internal resistance, which is obtained by reducing the thickness of the PEM from 183 $\mu\text{m}$  to 86.5 $\mu\text{m}$ , causes a decrease in the ohmic losses. This shows an increase in the peak power point as also compared in Figure 2.9. On the other hand, by increasing the internal resistance by changing the PEM thickness from 183 $\mu\text{m}$  to 366 $\mu\text{m}$ , the domination of ohmic losses will increase which leads a decrement in peak power. According to Figure 2.9, the Fill Factor of the prediction for  $0.5R_{int}$  is higher than the other two predictions which shows better performance of the system at lower internal resistance.



(a)



(b)

Figure 2.8 Prediction of the (a) I-V characteristics and (b) power characterization at various internal resistance

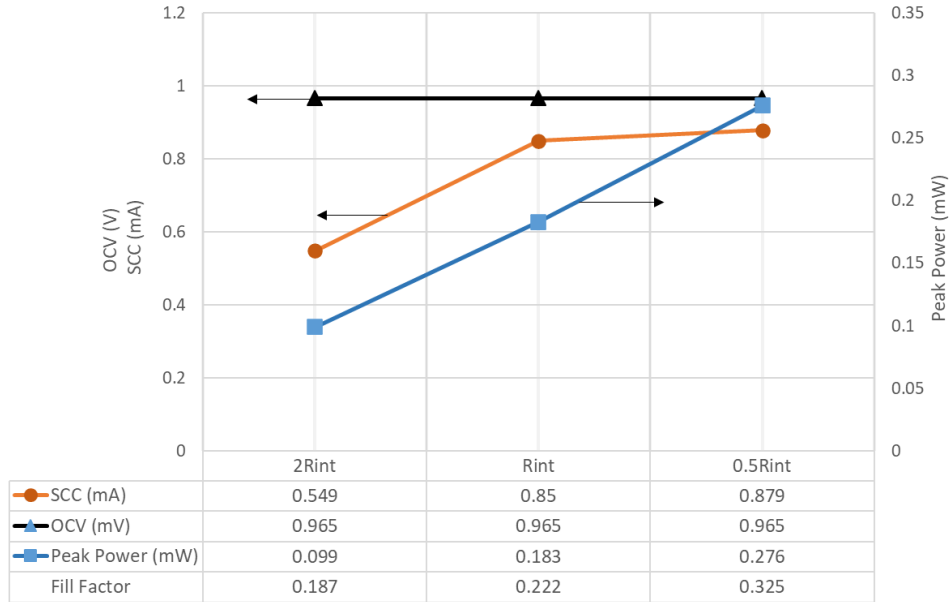
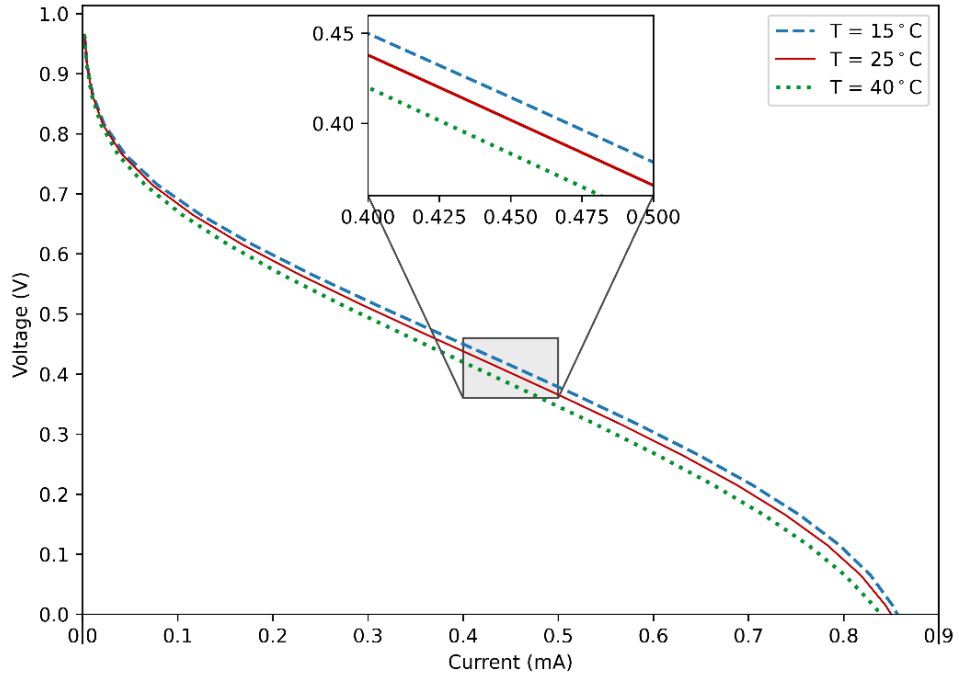


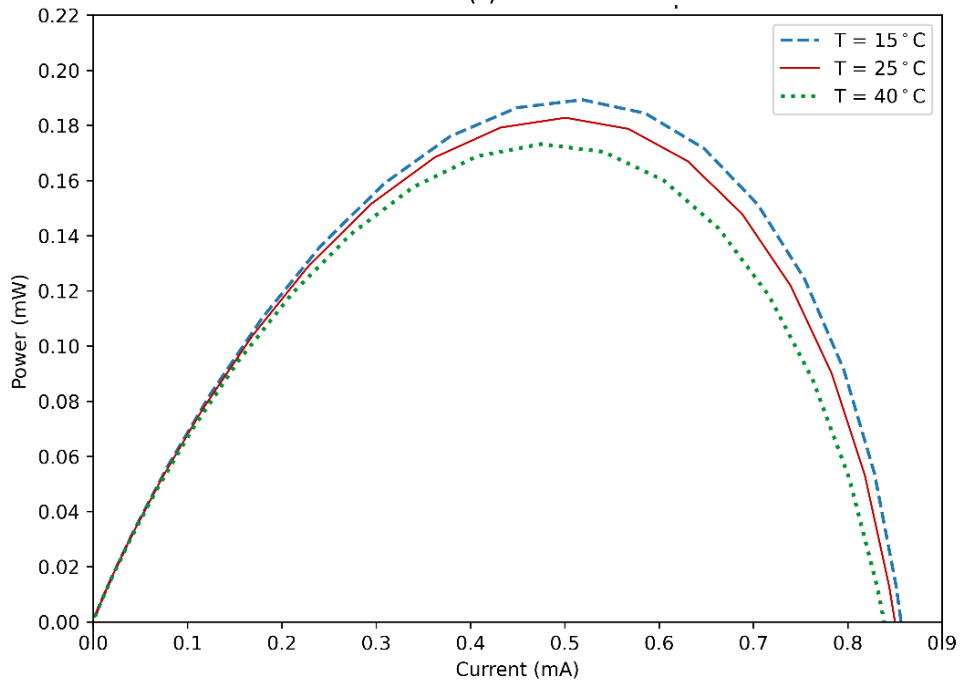
Figure 2.9 Variation of OCV (mV), SCC (mA) and peak power point from the prediction at various internal resistance

### 2.5.3. Temperature Effect

Most of the governing equations covered in the theoretical part are dependent on the temperature of the system. Temperature affects the diffusion of the participating species, the pressure of the system and respectively the system behavior. Initially, the  $\mu$ -PSC is operating and be tested at room temperature. Higher temperatures can damage the microalgae cells and lower temperatures can be fatal for them. Considering that the microalgae cell condition does not change, and the cells remain healthy within the mentioned range, the system may function more properly at a lower temperature than higher temperatures. However, within the ambient temperature range of 15°C to 40°C, the change in polarization curve and power curve is predicted and provided in Figures 2.10 which shows no significant effect on the operation of  $\mu$ -PSC which also stated in [55] and [29]. The small variations in the results at different temperatures can be subjected to the difference in flux  $j$  and diffusion coefficient.



(a)



(b)

Figure 2.10 Prediction of the (a) I-V characteristics and (b) power characterization at various temperature in COMSOL modeling

#### 2.5.4. Effect of Active Surface Area on the Output Power

Power generation in PEM fuel cells and similar technologies such as  $\mu$ -PSC is a function of the active surface area of the proton exchange membrane[65]. The effect of the same concept has also been studied within the modeling through COMSOL Multiphysics. Conceptually, the open-circuit voltage (OCV) of the device remains constant since the overall potential of the  $\mu$ -PSC device is defined by the potential of the chemical species that exist in each of the chambers of the  $\mu$ -PSC. In the cathode chamber, potassium ferricyanide (PF) and the set of chemical reactions as in Equation (2.11) and (2.12), give the potential of 0.82 V. similarly, the redox coupler (Methylene Blue) in the anode chamber that is assumed to portray a similar potential as with the microalgae culture inside the anode chamber is equal to -0.145V.

The output current is the parameter that is dependent on the active surface area of the  $\mu$ -PSC device. Higher active surface area lets more ions be transferred from anode chamber to cathode chamber through the PEM, and at the same time, due to the higher surface area of the electrodes, more electrons can be collected and be transferred through the external circuit for power generation. However, the higher active surface area can increase the overall cost of the device, increase the complexity of the device fabrication and the material needed for the fabrication. In addition, a higher surface area decreases the flexibility of the system compared with the output that can be achieved with several standard  $\mu$ -PSC devices with an area of 22mm by 22mm in series and parallel combination[45]. Figure 2.11 provides the prediction of the I-V characteristics and power characterization at the various active surface areas. The predictions have been made by varying the length ( $L$ ) of the model geometry, as provided in Figure 2.5 and Table 2.1. The variations of  $L$  are 11mm, 22mm, 33mm, 44mm, 66mm, and 88mm. According to Figure 2.11, the increase in surface area results in the increase in  $\mu$ -PSC current and peak power. The trend of the OCV, SCC, peak power and the Fill Factor of the prediction is provided in Figure 2.12. It can be seen that the variation in surface area, does not change the Fill Factor.

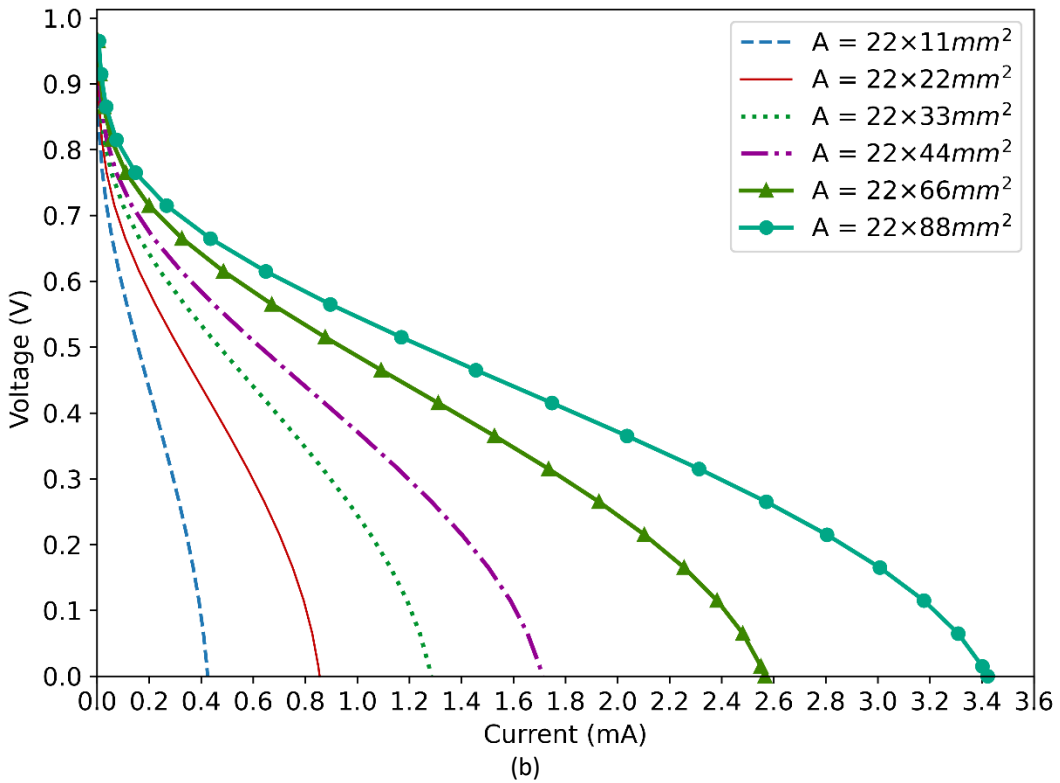
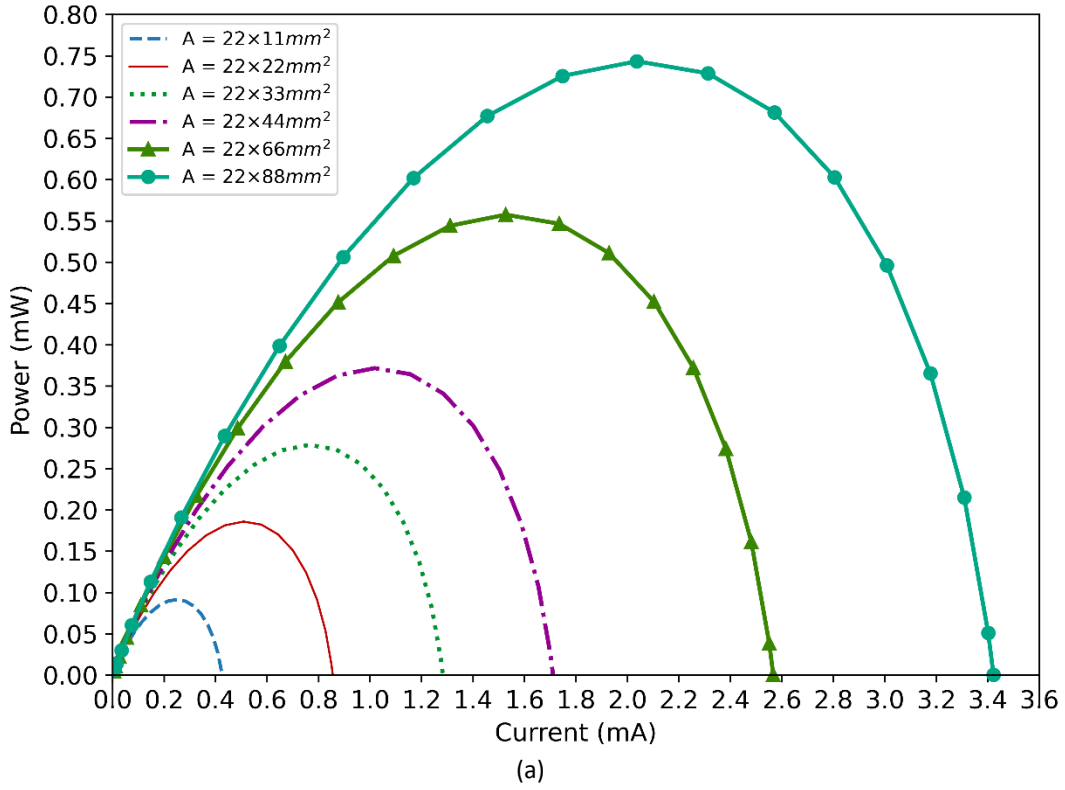


Figure 2.11 Prediction of the effect of active surface area on the (a) power curve and (b) polarization curve

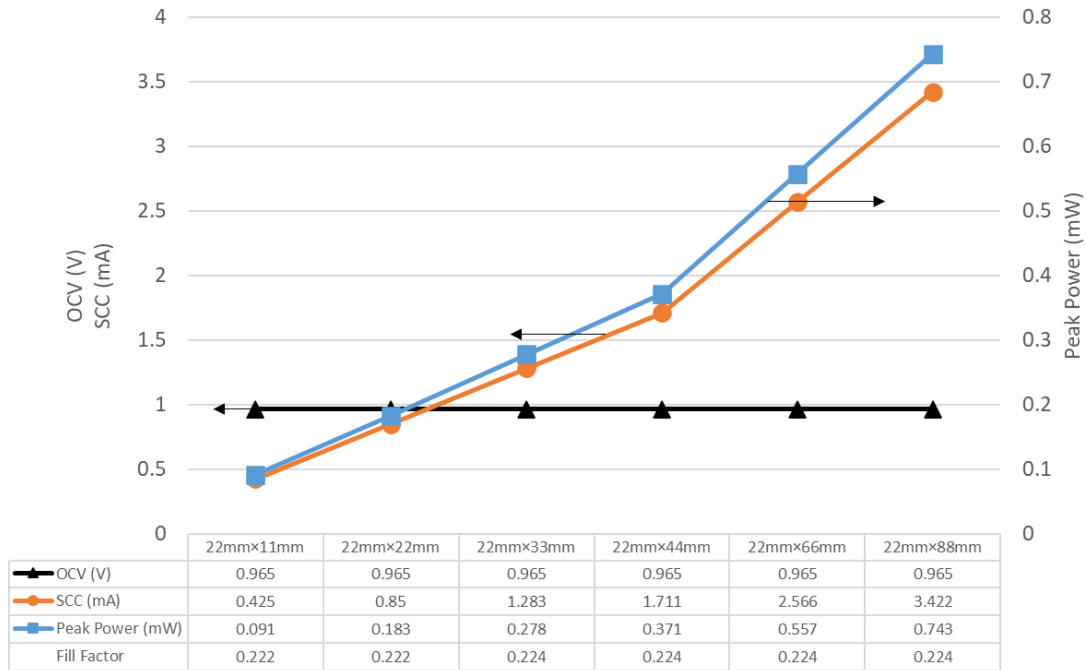
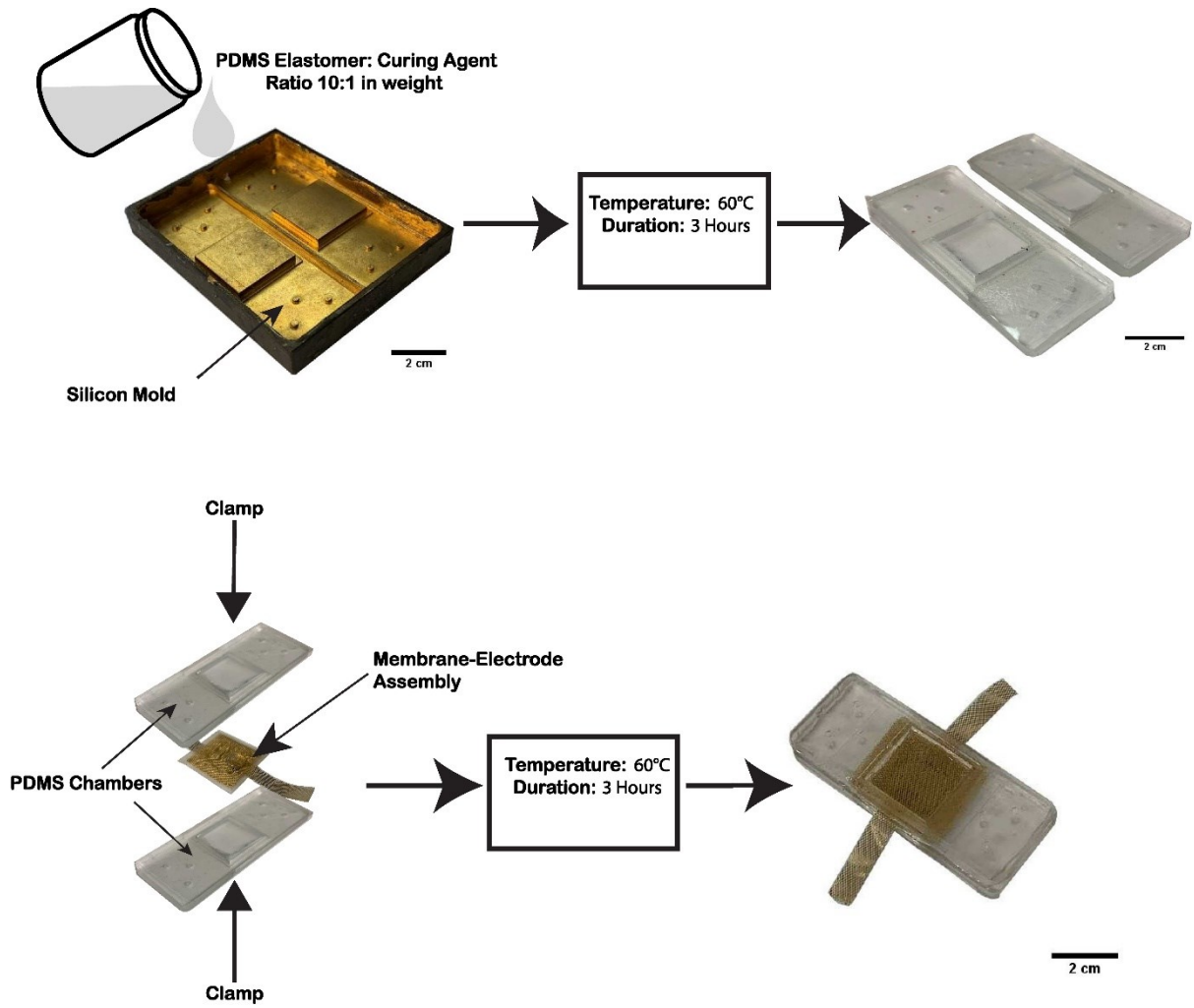


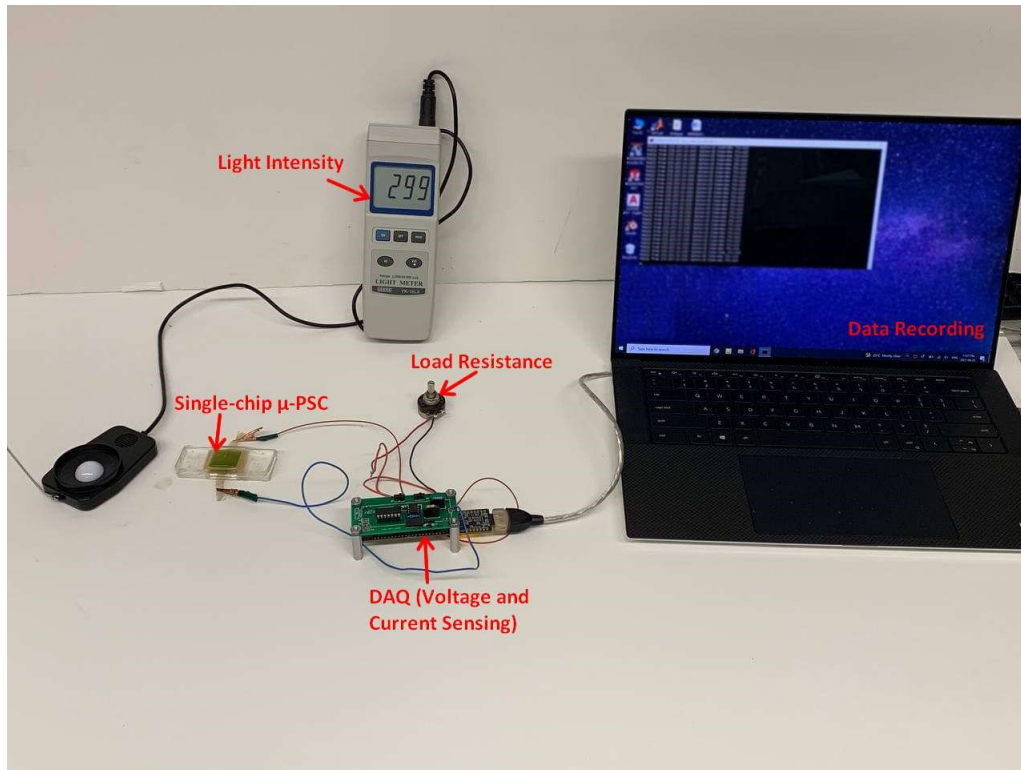
Figure 2.12 Variation of OCV (mV), SCC (mA) and peak power point from the prediction at various active surface area

## 2.6. Validation of Modeling Results

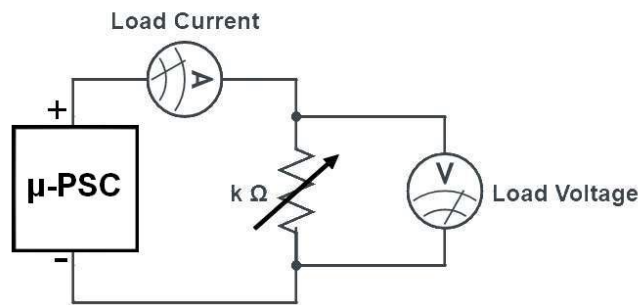
The modeling results need to be validated with the experimental data to be able to be used for future designs and further development. For this reason, the results have been compared and validated with the experimental results. For this purpose, a single-chip  $\mu$ -PSC has been fabricated similar to the fabrication process developed by Kuruvinashetti[45] and provided in Figure 2.13 (a). The chip has been tested with the experimental setup as in Figure 2.13 (b) and Figure 2.13 (c) and the experimental data for the I-V characteristics has been collected within three trials. The experimental data has been shown with the average value of the three trials as the midpoint and the variation of data as the error bar.



(a)



(b)



(c)

Figure 2.13 (a) Fabrication process of a single-chip  $\mu$ -PSC, (b) experiment setup of the single-chip  $\mu$ -PSC and (c) the schematic of single-chip  $\mu$ -PSC test for the I-V characterization

Figure 2.14 provides the I-V characteristics for the prediction showed in red dashed line, and the experimental data of the single-chip  $\mu$ -PSC showed in blue dots and error bar. It shows that the  $\mu$ -PSC cell can ideally produce around 900 mV at the near-OCV region and a short-circuit current (SCC) of  $850\mu\text{A}$  in the near-SCC domain. The experimental results show the OCV value of about 820mV at the first data point and reach the near-SCC value of about  $860\mu\text{A}$ , which shows a good agreement between the prediction and the experiment.

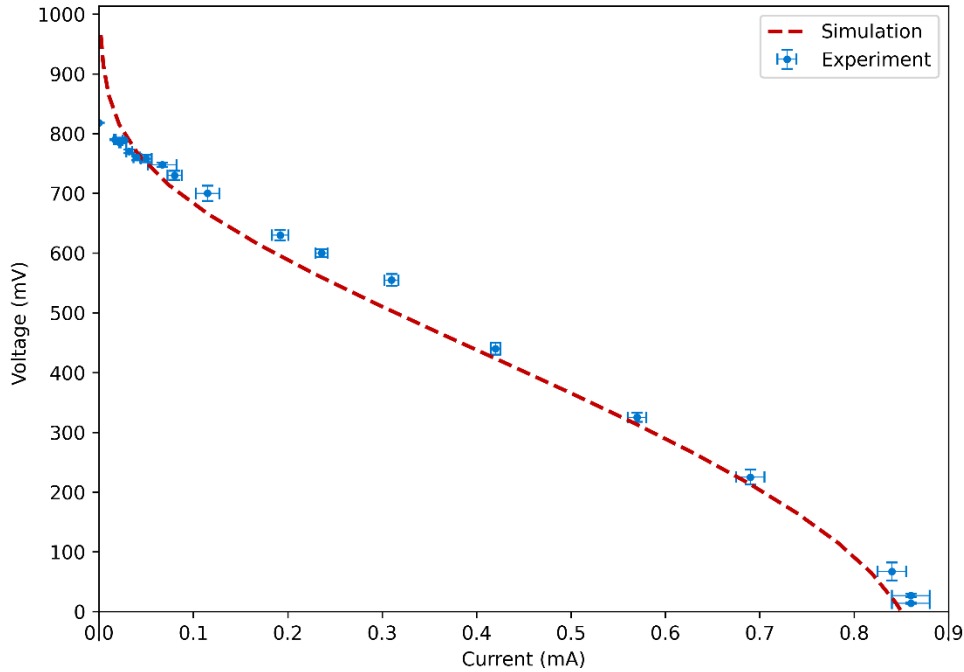


Figure 2.14 I-V curve of model prediction and experimental data

The prediction of the power curve in Figure 2.15 shows follows the same trend as with the I-V characteristics curve. The effect of resistance load variation on the current of the  $\mu$ -PSC and the power compared with experimental data is provided in Figures 2.16. When the resistance starts to change from  $0 \Omega$  to high values, the current starts decreasing from the maximum value in short-circuit current domain, which is around  $850 \mu\text{A}$ . This decrease will continue until very high values of resistance. The reason can be explained as when the external resistance starts increasing, the electric current decrease while the cell voltage increases on the electrodes, as provided in Figures 2.16 (a) and 2.16 (b). The trend between model prediction and experimental results for the variation of power over resistance follows a similar trend with the peak at a similar range. With the increase in resistance, the system reaches the peak power at the resistance of about  $800\Omega$ . The power decreases at which, in high resistance, it would reach zero. The comparison of OCV, SCC, Peak Power, and Fill Factor between the prediction and experimental data are provided in Table 2.3.

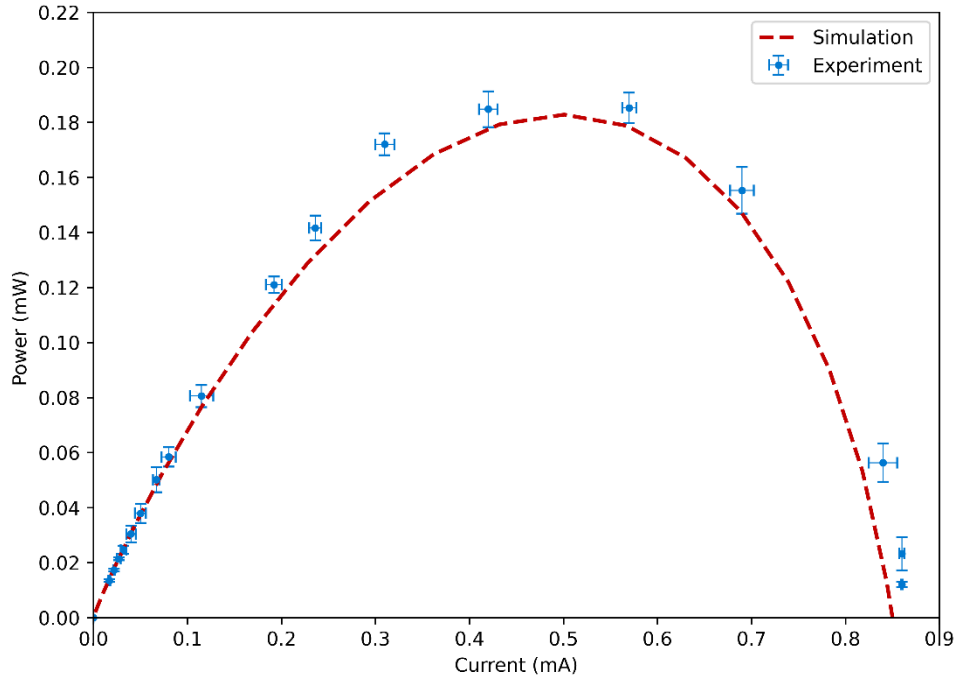
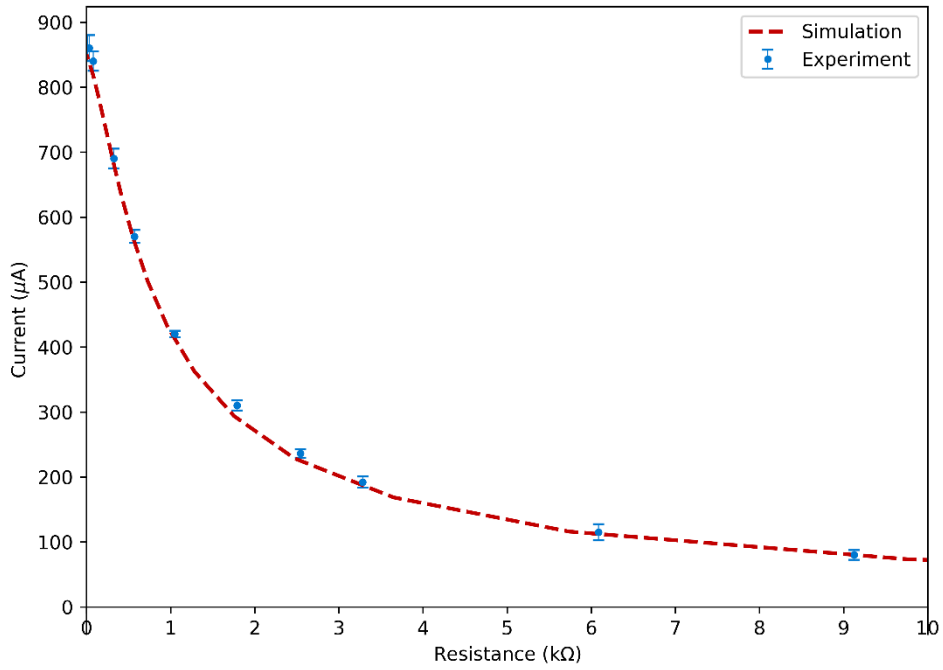
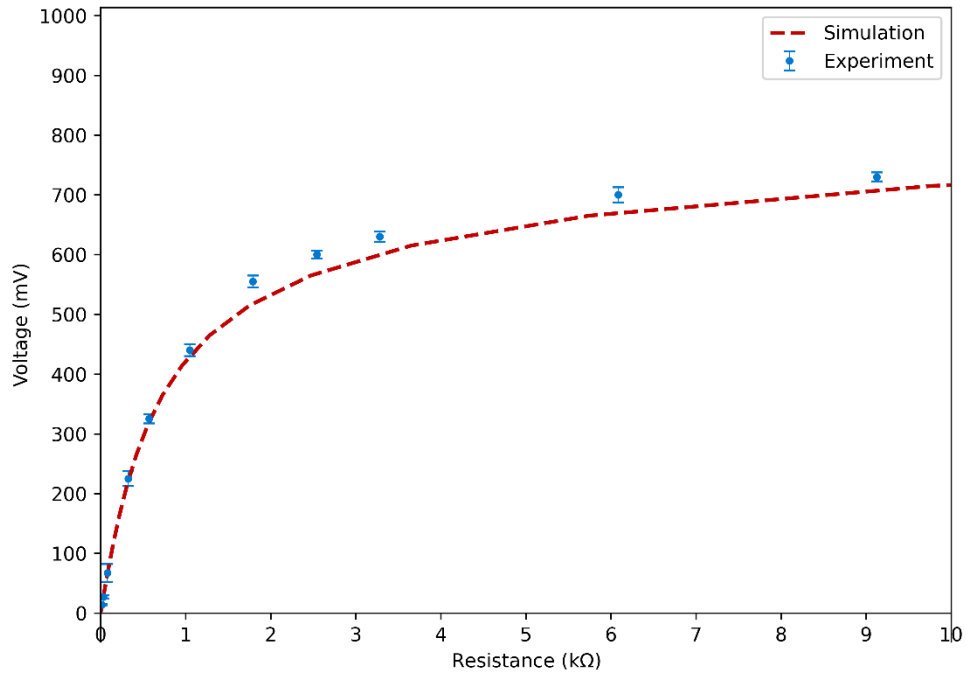


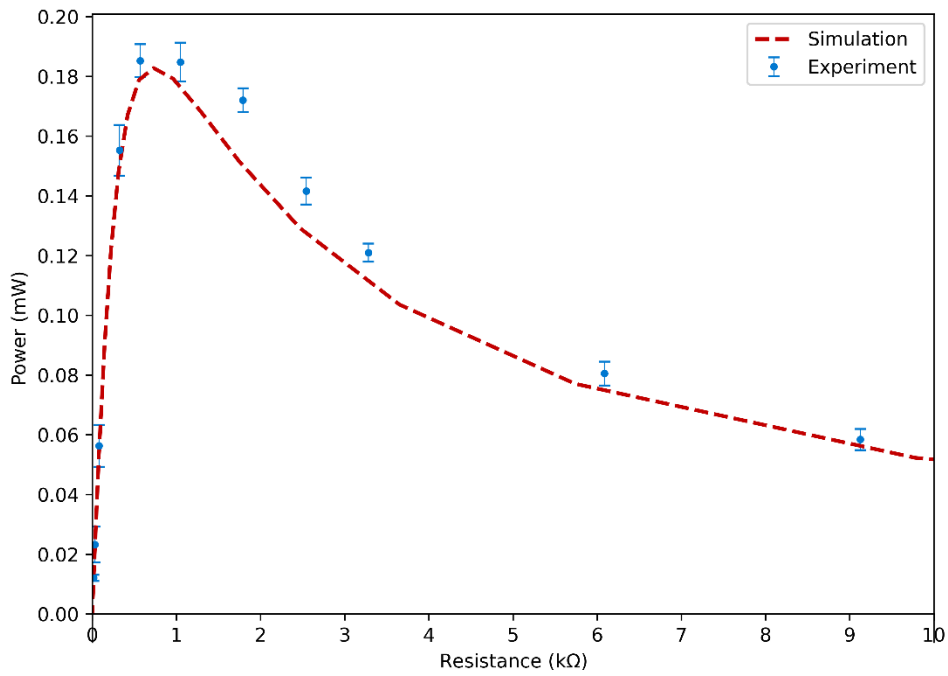
Figure 2.15 Power-current curve of model prediction and experimental data



(a)



(b)



(c)

Figure 2.16 (a) Current-load resistance, (b) voltage-load resistance curve and (c) power-load resistance curve of model prediction and experimental data

Table 2.3 OCV, SCC, Peak Power and Fill Factor variation of model prediction and experimental data

<b>Variable</b>	<b>Model</b>	<b>Experiment</b>
<b>OCV (V)</b>	0.965	0.818
<b>SCC (mA)</b>	0.85	0.86
<b>Peak Power (mW)</b>	0.183	0.185
<b>Fill Factor</b>	0.222	0.258

## 2.7. Conclusion

In this chapter, the modeling of the  $\mu$ -PSC device has been provided with the fuel cell operation perspective. The model has been developed based on previous research on the same technology adding electrochemical kinetic formulation and overpotential drops and losses. The parametric study at various conditions, including active surface area, temperature, internal resistance, etc. have been predicted and verified with experimental data of the I-V characteristics of a single-chip  $\mu$ -PSC. The comparison of the model shows good agreement with experimental. More development can be done on the model to predict the effect of other parameters on the performance of  $\mu$ -PSC.

### **3. Design, Development and Verification of an Interconnected Array Micro-Photosynthetic Power Cell**

#### **3.1. Introduction**

Recent advancements in wireless sensors and the Internet of Things (IoT)[1] require energy harvesting technology that can provide power in micro-scales. It is desired that the energy harvesting source can be able to function in light and dark conditions. Moreover, the environmentally friendly aspect of the power source is another critical factor to provide a sustainable future. The micro photosynthetic power cell ( $\mu$ -PSC) is an alternative in providing such power both in light and dark conditions. In  $\mu$ -PSC, living photosynthetic microalgae culture, which has been suspended in cell media, works as the heart of the system by generating electrons through photosynthesis. In light conditions, cells absorb light energy and release electrons and protons through a series of complex subcellular reactions involving a split of water molecules. In the absence of light, the generated sugars created during photosynthesis works as the source of electrons and proton generation in a process known as respiration[66].

Recently, researchers conducted different studies to optimize the design and implemented material and chemical components to obtain higher power from the  $\mu$ -PSC. Many of these optimizations have been conducted on developing microbial fuel cells, which are quite similar to  $\mu$ -PSC in terms of system design and outputs.

In the development of  $\mu$ -PSC technology, Shahparnia[29] prepared a two-chamber PDMS chamber  $\mu$ -PSC in which the chambers were separated by a proton-exchange membrane (PEM). On the anode side, the microalgae culture of *Chlamydomonas reinhardtii*, which was suspended in cell media, has been used as the source of proton and electron generation, and potassium ferricyanide has been used as the catholyte. The effect of various parameters on the performance of  $\mu$ -PSC has been determined and optimized, including the catholyte concentration. The device was designed within an active surface area of 22mm by 22mm. The results showed an OCV of around 700 to 800 mV.

Caprariis et al. [67] design a PEM bio photovoltaic power cell that implements *Chlorella Vulgaris* algae culture as the electron generator. The device was made of PMMA in two overlaying

cylindrical compartments. The device's overall size was reported to be 4cm in diameter and 3.1cm in height, and an active surface area of 5cm<sup>2</sup> for the membrane-electrode assembly. The polarization curve shows an open-circuit voltage (OCV) data of about 150mV.

Rowden et al.[68] provides a fabricating technique for bio photovoltaic power cell which implement cyanobacteria biofilm for electricity generation. The design consisted of 50mm by 50mm in surface area of PMMA anode and cathode chambers. The design includes an inlet/outlet for media change. The results showed a short-circuit current density of 90 mA/m<sup>2</sup> in the light condition.

Kuruvinashetti[45] provides a cheaper way of fabricating PDMS  $\mu$ -PSC. In this method, gold was sputtered on a thin Aluminum grid. The electrodes then bonded to the proton exchange membrane by water-proof adhesive to form the membrane-electrode-assembly (MEA). The final device was resulted by the stacking of PDMS chambers and MEA. The combination of multiple single-chip  $\mu$ -PSC for series and parallel connection has also been studied. The results show higher voltage/current in the series/parallel combination of the cells.

The conducted researches showed promising results with a single chip design. The obstacle toward further integration of  $\mu$ -PSC and IoT microsensors is the low power density and current output of the  $\mu$ -PSC, which cannot be operational for micro sensors[69]–[71]. Several ways can lead to an increase in output power density. Due to the similarities between PEM fuel cells and  $\mu$ -PSC in terms of electrochemical functionality, the effect of several parameters follows the same trend in both systems. The surface area is one main parameter that can increase the output current dramatically. In other words, power generation in these systems can be expressed as a function of surface area as more surface area is capable of collecting more electrons and protons transfer in comparison with the designs with lower surface area[17]. This will increase power and current output with the increase in the surface area, while OCV depends on the electrochemical potential of anolyte and catholyte.

In this chapter, a new design for the  $\mu$ -PSC is provided. The device consists of an array of three  $\mu$ -PSC devices which are internally connected, having three chambers with an active surface area of 4.84cm<sup>2</sup> each. Theoretically, the higher surface area will lead to an increase in output current. In this chapter, the design of the system has been provided, and the outputs from each chip and the effect of internal connections are presented.

### 3.2. Principle of Operation

Micro-photosynthetic power cell ( $\mu$ -PSC) is an electrochemical cell that produces electricity at micro-scale under light and dark conditions. In light conditions, a blue-green algae culture uses light to consume carbon dioxide and water in the photosynthesis process which results in the production of glucose and oxygen. Moreover, during the dark conditions, the produced glucose, disintegrates with the help of oxygen. Both the processes cause the release and the transfer of electrons which are the main source of power generation in  $\mu$ -PSC. This shows that  $\mu$ -PSC is able to generate electricity under both light and dark conditions, which overcome the limitation of photovoltaic power cells[29].

Figure 3.1 provides a general schematic of the operation of  $\mu$ -PSC. The  $\mu$ -PSC consists of two chambers known as anode chamber and cathode chamber which are separated with a proton exchange membrane (PEM). The PEM only allows positive hydrogen ions (protons)[72] to pass through itself from anode chamber to cathode chamber. The negative charges or electrons would be collected from the anode chamber by the electrodes which have been placed on both sides of the PEM and releasing them in the cathode chamber for the completion of the electrochemical reaction.

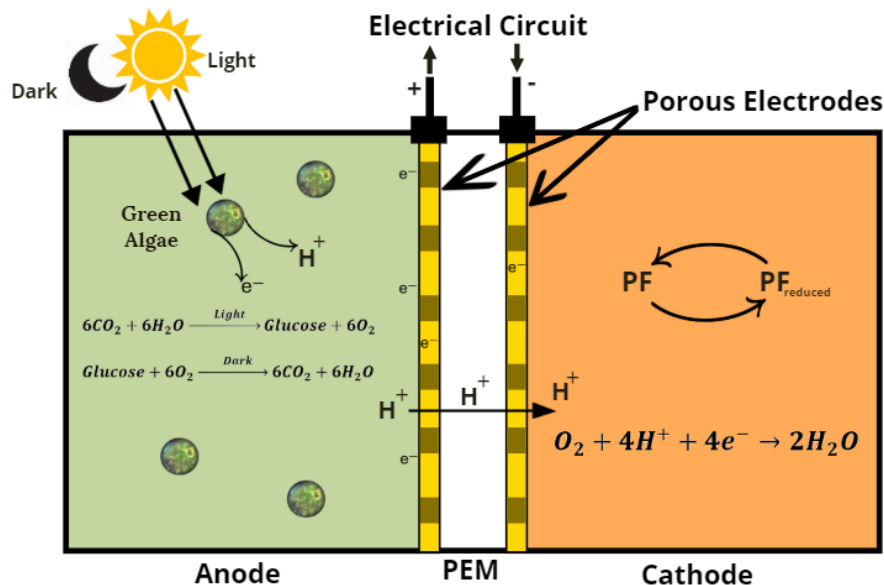
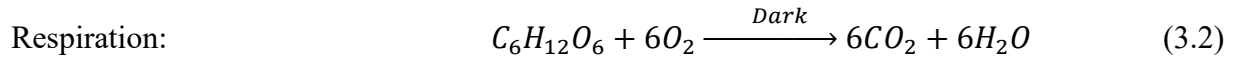
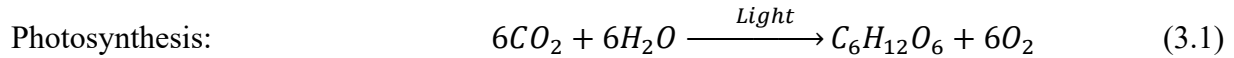


Figure 3.1  $\mu$ -PSC principle of operation

The living microorganism which has been used for this research is *Chlamydomonas reinhardtii* CC-125 wild-type. This microalgae culture is a widely used species for the research of photosynthesis[54]. In the anode chamber, microalgae culture performs photosynthesis or respiration depending on the light conditions. In the presence of light, the cells absorb light, and through a complex series of sub-cellular reactions, photosynthesis will occur. During this process, electrons and protons will be released. The protons pass through the PEM and are transferred from the anode chamber to the cathode chamber. At the same time, the electrons will be collected by the electrodes and transferred through an external circuit for power generation. In dark conditions, the overall reactions revert, is known as the respiration process, in which the released glucose will be turned back to carbon dioxide. The overall reaction in both the light and dark conditions can be summarized as follow:



On the cathode side of the  $\mu$ -PSC, the electrons will reduce the electron acceptor (catholyte) which is Potassium Ferricyanide, to Potassium Ferrocyanide. At the same time, the transferred protons will oxidize back the reduced catholyte and with their combination with oxygen, water will be released[59].

### 3.3. Material Selection Experiment

An important aspect of the development of  $\mu$ -PSC, especially for this research, is the design and fabrication technique. It is desired that the design be scaled up with many cells implemented in one frame. Moreover, within the conventional fabrication technique, the complexity of having an array of multiple  $\mu$ -PSC will be increased dramatically. On the other hand, increasing the complexity causes an increase in the consumption of material, fabrication time, overall costs, and errors that might happen during the fabrication. For these reasons, it is important to provide a fabrication technique that covers the limiting aspects of the previous designs in addition to the fact that the chip material that is going to be used must be compatible with the biological organisms, catholyte material, and cell media.

### 3.3.1. Materials and Method

#### 3.3.1.1. Materials

The choice of material plays an important role in the development of  $\mu$ -PSC. Previously, polymer-based chambers were prepared using PDMS. This material is bio-compatible, which makes it a proper choice while being used with living microorganisms. However, due to its high structural flexibility, the portability of the device is low as the device can be easily damaged. A proper bonding material to isolate the chambers, prevent leakage, and fabricating the device is a thin layer of PDMS itself which can work as a proper adhesive to bond the PDMS chambers. However, modifying the fabrication technique for an array of  $\mu$ -PSC devices with the PDMS chambers increase the complexity of fabrication and also increases the possibility of device failure.

For the given reasons, A new material needs to be chosen which provides higher strength for having multiple devices in one frame and being compatible with the living microorganism. Four materials have been chosen and investigated in terms of cell compatibility as provided below:

- Epoxy Resin D.E.R 324[73] from ANAMET company is a low viscosity liquid resin with low surface tension, which provides a proper surface wetting for component preparation. The mixing ratio for this resin and its hardener is 100:60 in weight. This material is optically clear. The given material was found to be chemically unstable in contact with several corrosive materials. Due to the presence of weight change in the presence of chloride ions which are one of the elements in cell media, the biocompatibility of this epoxy needs to be determined which is discussed in the next section. The structural specification is available in Table 3.1
- Epoxy Resin EPON 862[74] from HEXION is a low viscosity liquid resin with zero amount of diluent or modifier and provides good surface quality. This resin is reported to have proper chemical resistance. This resin needs to be mixed with an organic curing agent known as EPIKURE curing agent W with the resin to curing agent ratio of 100:26 in weight to be able to be cured and form solid components. However, a biocompatibility test has been implemented which will be discussed in the next section. The more structural specification is available in Table 3.1
- Polylactic Acid (PLA) plastic from Jgaurora company is a polymer material used in Fused Deposition Modelling (FDM) 3D printer technology. It provides the possibility of

producing mechanical components with proper geometrical detail and low cost. This material is reported to be biocompatible[74] in the presence of the living cell. Moreover, due to the presence of ions in cell media (Tris-Acetate-Phosphate solution), it is important to also test the toxicity of PLA with algae cell. The more material specification is available in Table 3.1

- Formlabs standard resin for Stereolithography (SLA) 3D printing is a thermoset polymer provided in various configurations. The material used in this research is the clear resin with the mechanical specification provided in Table 3.1. Biocompatibility has been investigated previously[75]. However, its interaction with cell media needs to be investigated.

Table 3.1 Material specification for the  $\mu$ -PSC frame

	Epoxy Resin D.E.R 324[73]	Epoxy Resin EPON 862[76]	Polylactic Acid (PLA)	Formlabs clear Resin[77], [78]
Tensile Strength (MPa)	87.9	122	37	65
Density at 25°C (g/ml)	1.10	9.9	1.3	1.09
Dynamic viscosity at 25°C (mPa.s)	600-800	2500-4500	-	900

In order to investigate the biocompatibility of the selected materials and to find out whether the materials have a fatal effect on the cells, a simple qualitative experiment has been designed to check the effect of direct contact of each of the proposed materials with the cells and their viability.

### 3.3.1.2. Cell Culture

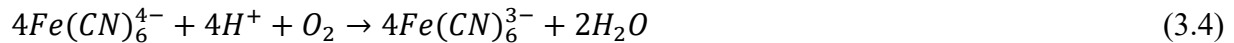
The main cell culture that has been used in the whole research is green-algae *Chlamydomonas reinhardtii* CC-125 wild type which is a widely used species[54] specifically in the research of photosynthesis and the function of the chloroplast. The cells have been cultured and suspended in Tris-Acetate-Phosphate solution (Known as TAP media). The solution contains the reduced carbon acetate which allows rapid cell division[79]. The components of 1 liter of TAP media have been provided in Table 3.2.

Table 3.2. Preparation steps for 1 liter of TAP media

<b>TAP media</b>	Deionized water	1000 ml
	1 Molar Tris base	20 ml
	Phosphate Buffer II*	1.0 ml
	TAP salts**	10.0 ml
	Hutner's trace elements	1.0 ml
	Glacial acetic acid	1.0 ml
* Phosphate Buffer II (100ml)	Deionized water	100 ml
	Dipotassium phosphate ( $K_2HPO_4$ )	10.8 g
	Potassium dihydrogen phosphate ( $KH_2PO_4$ )	5.6 g
** TAP salts (500 ml)	Deionized water	100 ml
	Ammonium Chloride ( $NH_4Cl$ )	20 g
	Magnesium sulfate hexahydrate ( $MgSO_4 \cdot 7H_2O$ )	5 g
	Calcium chloride dehydrate ( $CaCl_2 \cdot 2H_2O$ )	2.5 g

### 3.3.1.3. Catholyte Material

The main characteristic of the catholyte is able to accept electrons properly. Potassium ferricyanide ( $K_3[Fe(CN)_6]$ ) is bright red color salt that can be dissolved in water. Its redox potential lets it be reduced easily to potassium ferrocyanide when accepting electrons. With the appearance of protons on the cathode side, the ferrocyanide oxidizes back to ferricyanide, and the combination of electrons, hydrogen, and oxygen in the cathode chamber, results in the generation of water[59].



The  $\mu$ -PSC chip potential is dependent on the concentration of the potassium ferricyanide in Deionized water. The optimum concentration results in acquiring higher open-circuit voltage (OCV) from the  $\mu$ -PSC. Shahparnia[22] investigate the effect of potassium ferricyanide concentration to find out the optimum value. For this reason, the optimum concentration of 25% w/v (25gr/100ml) of potassium ferricyanide is going to be used as the catholyte.

### 3.3.2. Methodology

In order to find out the bio-toxicity of the materials, a small sample of each of the chosen materials has been prepared with the same size. Figure 3.2 provides an overall schematic of test specimens preparation for the test of their biocompatibility with microalgae culture. The size of the samples has been chosen to be able to be fit inside a 24-well cell culture plate. For the two epoxy resins of D.E.R 324 and EPON 862, the materials have been mixed with the ratio provided in Section 3.3.1.1 and have been cured to have the final specifications that are required for the potential  $\mu$ -PSC chambers frame. The test PLA specimen has also been 3D-printed into with the size of 1cm<sup>3</sup>. A test specimen of Polydimethylsiloxane (PDMS) 184 sample, which has been mixed with curing agent at the ratio of 10:1 and cured at the temperature of 60°C for 3 hours, has also been prepared as the control sample and reference. The samples have been washed with deionized(DI) water having a resistivity of 18.1 M $\Omega$ , as in Figure 3.2 (1), dried, and kept under a germicidal UV lamp in class II biological safety cabinet, in the sample well for 30 minutes, as in Figure 3.2 (2), to minimize the contamination including bacteria, dust particles, etc.

Next, the CC-125 microalgae culture, which suspended in TAP media for 48 hours at the temperature of 23°C, with the volume of 2.5ml, as in Figure 3.2 (3), has been added to each sample well to make algal cells have direct contact with the test specimens as shown in Figure 3.2 (4). A CC-125 culture with no test material has also been placed as a reference for cell conditions. The samples then isolated using parafilm and kept at room temperature and light condition of 300 lux. The condition of the cells has been investigated every 24 hours for 14 days. The investigation of cell condition includes the green color of the cell in each time step by visual inspection. The daily images from the samples have been provided in Figure 3.3.

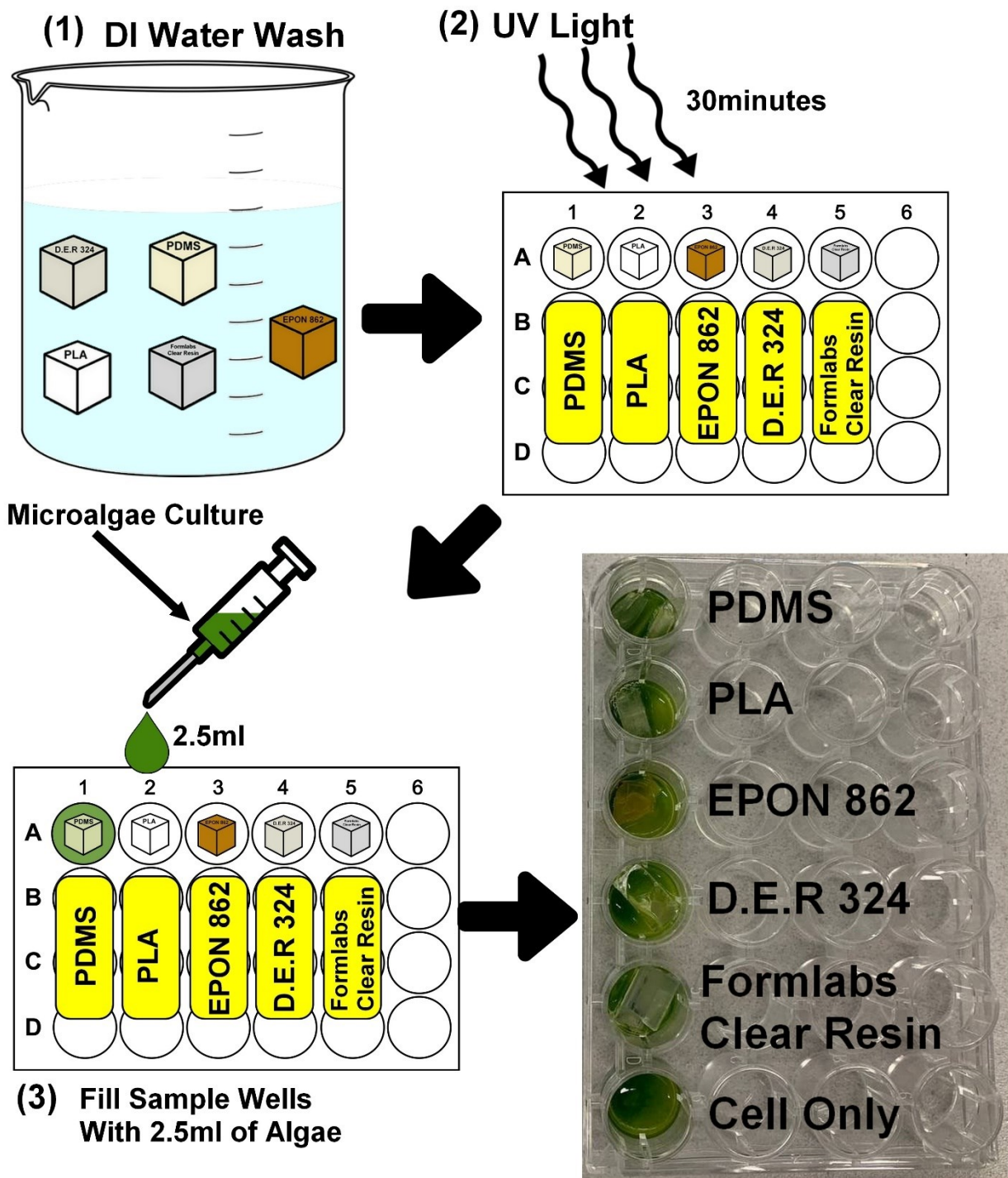


Figure 3.2 Experiment preparation steps schematic of the biocompatibility of test specimens and microalgae culture

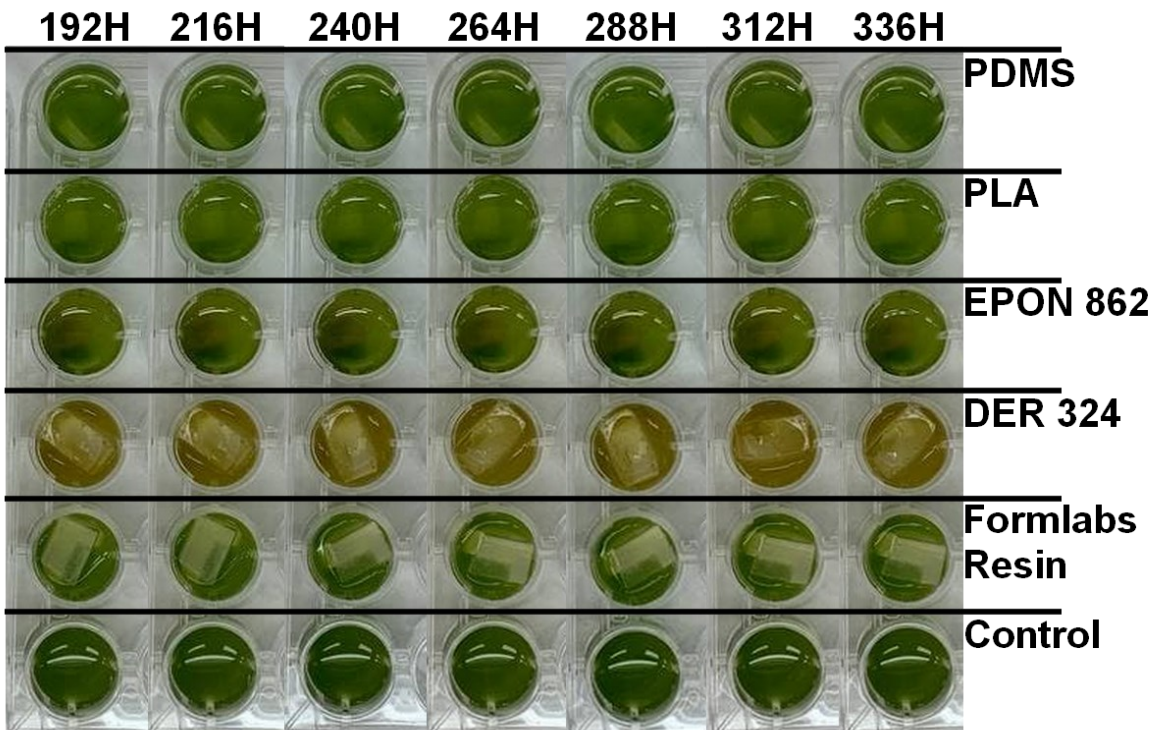
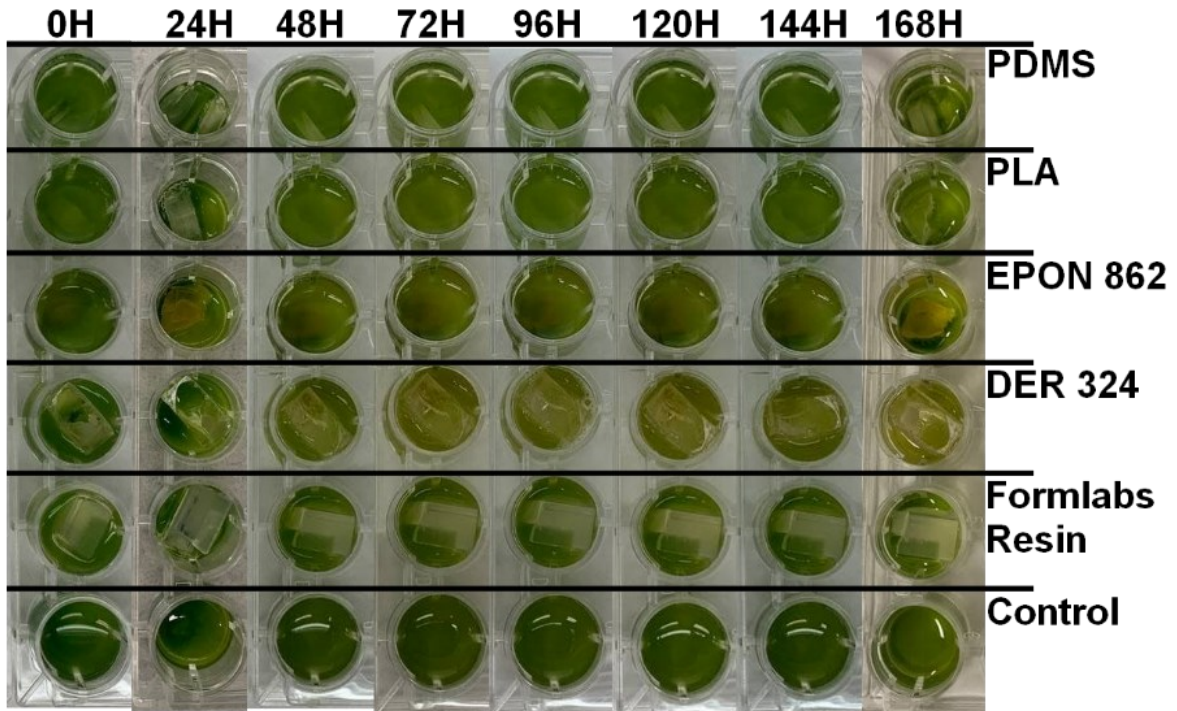
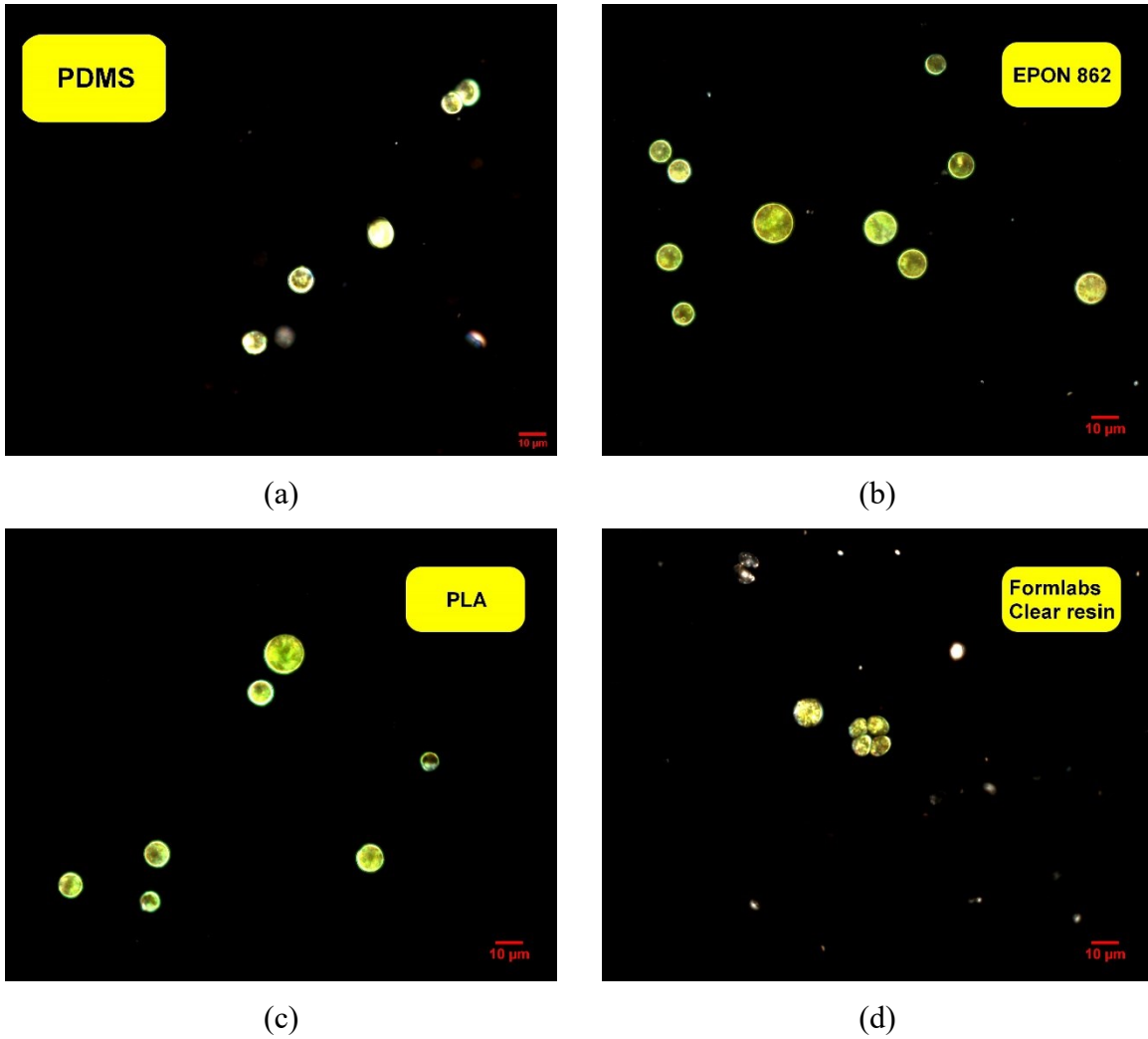


Figure 3.3 14 Days visual inspection of the sample plate

It has been seen that the condition of the cells in the PLA sample, Epoxy Resin Epon 862, and Formlab Clear resin follows the same manner as with the reference PDMS sample. The cells were green in the visual inspection and showed flagella movement in the microscopic investigation. On the other hand, the green color of the cells that disappeared in the D.E.R 324 sample shows the possible damage to the cell chloroplast. Figure 3.4 provides the microscopic image at 60x magnification with results and visual color check of the samples after 14 days.



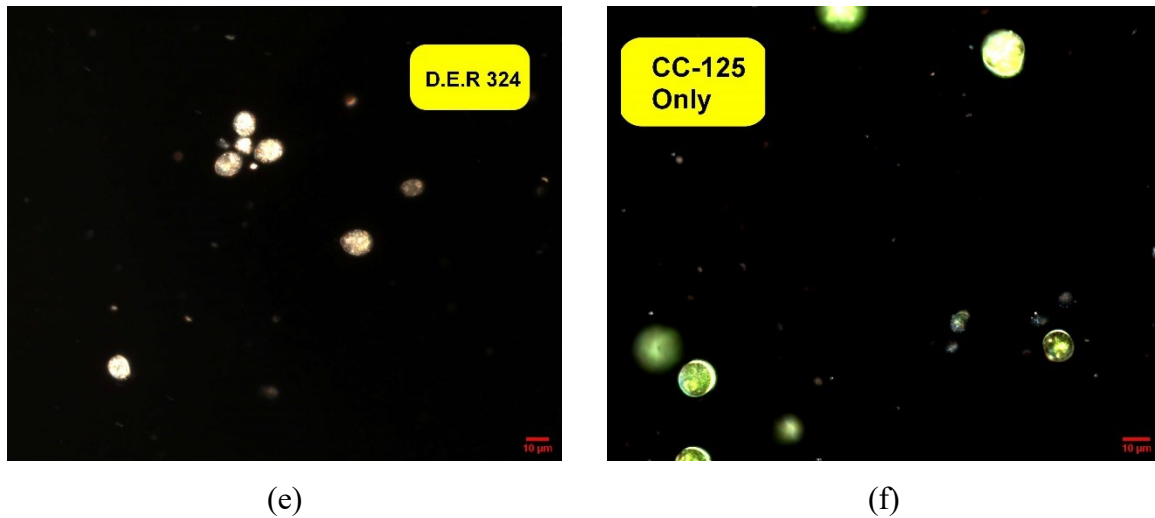


Figure 3.4 Optical 60x microscopic image of CC-125 in contact with (a) PDMS, (b) EPON 862, (c) PLA, (d) Formlabs clear resin, (e) D.E.R 324, and (f) CC-125 only

### 3.3.3. Discussion on Material Selection

The observation from daily visual inspections can help to choose the proper substrate material which is compatible with the cell environment.

The images in Figure 3.3. show that the Polylactic Acid (PLA) plastic provides proper compatibility with the cells and cell media as the color of the media did not change after the period of the test. Moreover, the microscopic image in Figure 3.4 (b) demonstrates green and healthy algal cells after the experiment's period.

The visual inspection of the contact between CC-125 with EPON 862 shows no sign of color change and observable change in the condition of cells with respect to reference samples, as provided in Figure 3.3. In addition, as shown in Figure 3.4 (c), an optical microscopic image of the cell shows the proper condition of the cells in the EPON 862 sample in terms of cell color.

The observation of the 14 days of visual inspection shows that the color of the cell in contact with epoxy resin D.E.R 324 starts changing after 48 hours. The change in color from green to yellowish may be a sign of damage to chloroplast which is the photosynthesis factory of the cell which results in degradation of overall cell quality. The reason can be both biological or chemical and the exact occurring process can be quite complex while it is not in the scope of this experiment. Epoxy resin D.E.R 324 shows weight change when in contact with corrosive material[73]. As with the chemical

composition of TAP media in Table 3.2, the presence of chloride ions as well as glacial acetic acid, etc. might be the reason for such incompatibility. The color change and degradation of the algal cell after two weeks of direct contact with D.E.R 324 is shown in Figure 3.4 (d) using 60x optical imaging.

Formlabs clear resin shows no change when in contact with microalgae cells in the visual inspection experiment as in Figure 3.3. The color of the cells remains green, as with the previous researches[75]. The microscopic image shows no specific change in the chloroplast and cell color with respect to the image of CC-125 at no contact and in contact with PDMS.

The D.E.R 342 resin shows incompatible results with the cells, which makes it an improper choice for the fabrication of the array of  $\mu$ -PSC. From the results of the visual investigation and microscopic images, the Formlabs clear resin, EPON 862, PLA plastic shows compatibility with the cell and have the potential to be used for the fabrication of an array of the  $\mu$ -PSC chamber.

### **3.4. Geometry and Design**

The overall design of the interconnected array of  $\mu$ -PSC consists of one frame with three anode chambers and one frame with three cathode chambers. Two PDMS gaskets are fabricated to prevent the leakage of the anolyte/catholyte. Between the PDMS gaskets, the assembly of proton exchange membrane (PEM) and the gold electrodes are placed. The parts need to be stacked together with eight M4 screws to form the final device. The overall view of the interconnected array of  $\mu$ -PSC is provided in Figure 3.5. The specification of each of the mentioned part is explained as follow.

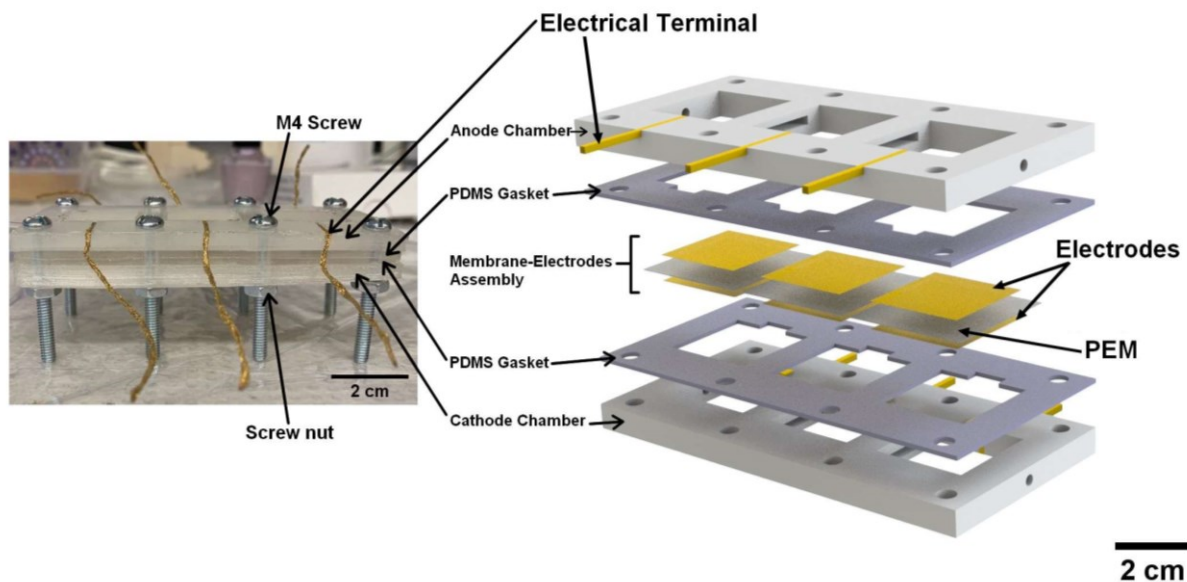


Figure 3.5. Exploded view of the interconnected array of  $\mu$ -PSC

### 3.4.1. Chambers and Gaskets

The design of the interconnected array of  $\mu$ -PSC is based on having multiple 22mm by 22mm chips into one frame with an internal connection between adjacent chambers. As the main goal is to investigate the effect of the internal connection of the anolyte/catholyte on the output of the  $\mu$ -PSC, the frame containing three chambers with internal connection has been 3D-printed using an (FDM) printer. Due to the presence of the internal connections between the chambers, fabrication of the chambers with PDMS, as provided in previous researches[29], [45], is a complex and time-consuming process. The FDM 3D printing is based on the deposition of melted PLA using a pre-determined layer-by-layer pattern. It provides a low-cost solution for 3D printing structures with certain complexities. Figure 3.6 shows the interconnected chamber schematic with 3D-printing resolution.

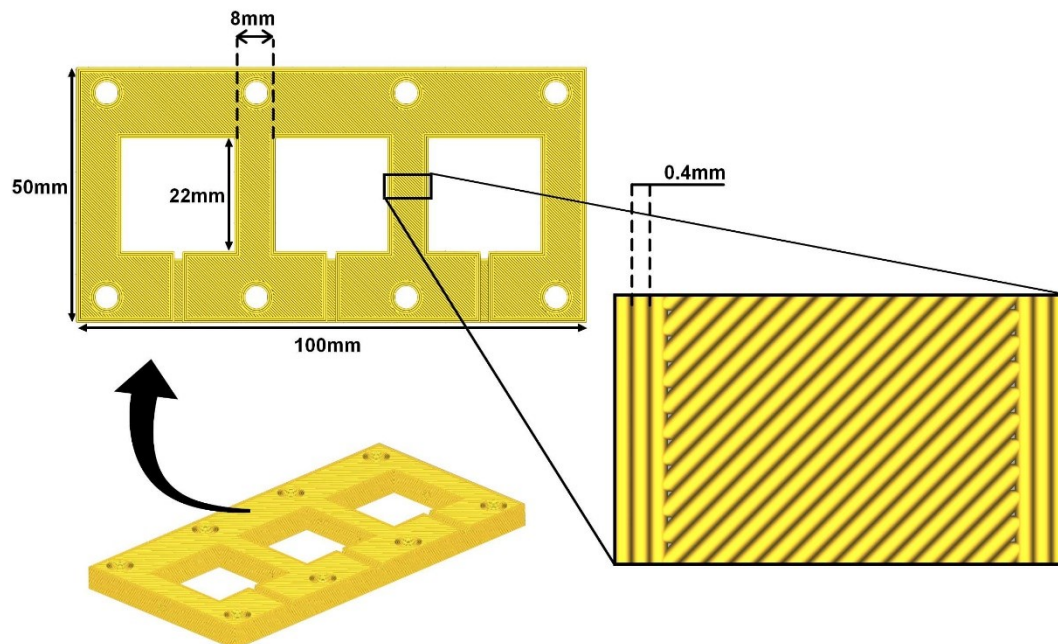


Figure 3.6 FDM layer-by-layer printing pattern

Figure 3.7 and Figure 3.8 provide the chamber design and other specifications for the interconnected array  $\mu$ -PSC which has been 3D printed with PLA plastic. The structure contains an inlet and outlet on the ends of the device and can be used for anolyte/catholyte replacement. The inlet and outlet can be blocked using a hot glue stick from Gorilla company. The surface area of each chamber follows the previous designs, which were 22mm by 22mm. The chambers were internally connected using 14mm by 2mm channels. The complete design of the chamber is provided in Figure 3.7. The dimensions were chosen based on the mainframe design. The eight holes are placed for M4 size screws and would be used for stacking the structure.

The printed PLA part does not provide enough flexibility to ensure zero medium leakage between the anode and cathode chamber. For this reason, the presence of sealing is required to make sure that the media on each side are not leaking to the other chambers. For this reason, two thin PDMS layer with a thickness of 2mm has been prepared with SYLGARD 184 at the ratio of 10:1 and cured in the oven at 60°C for 3 hours, in order to have proper flexibility[80], and cut in the dimension of the frame as shown in Figure 3.5.

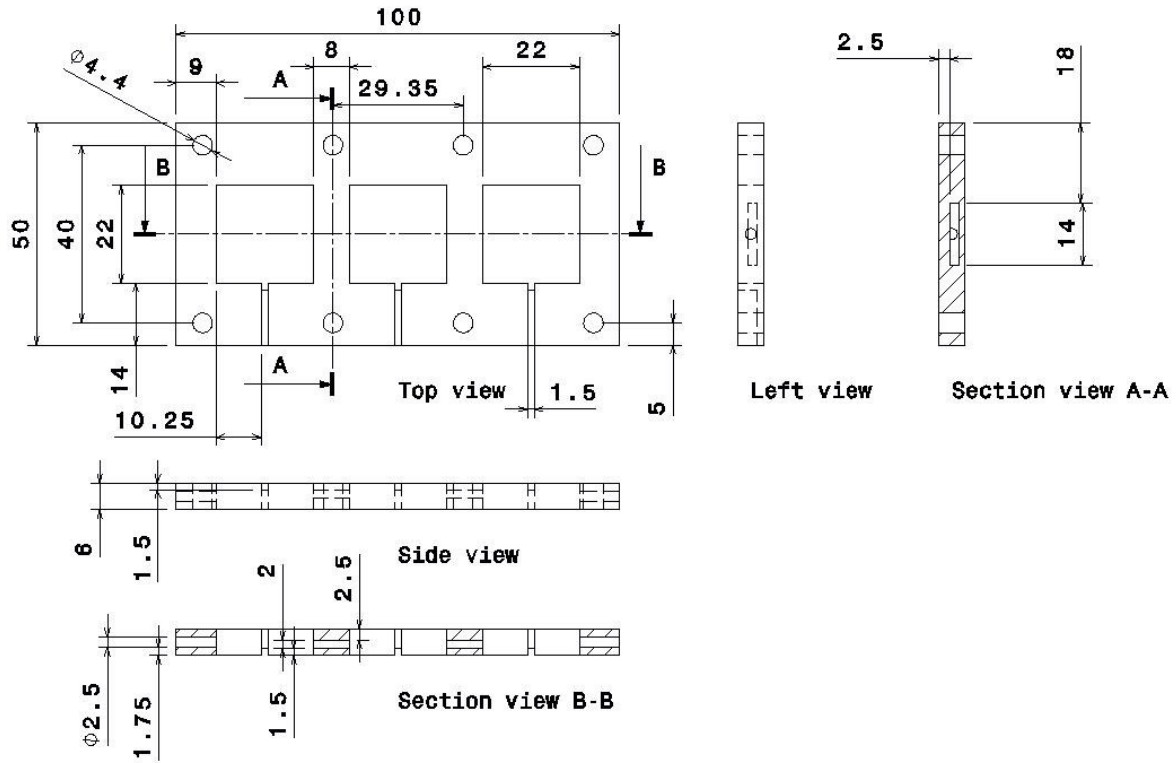


Figure 3.7 Integrated internally connected  $\mu$ -PSC geometrical specifications\*

\* All dimensions are in millimetre

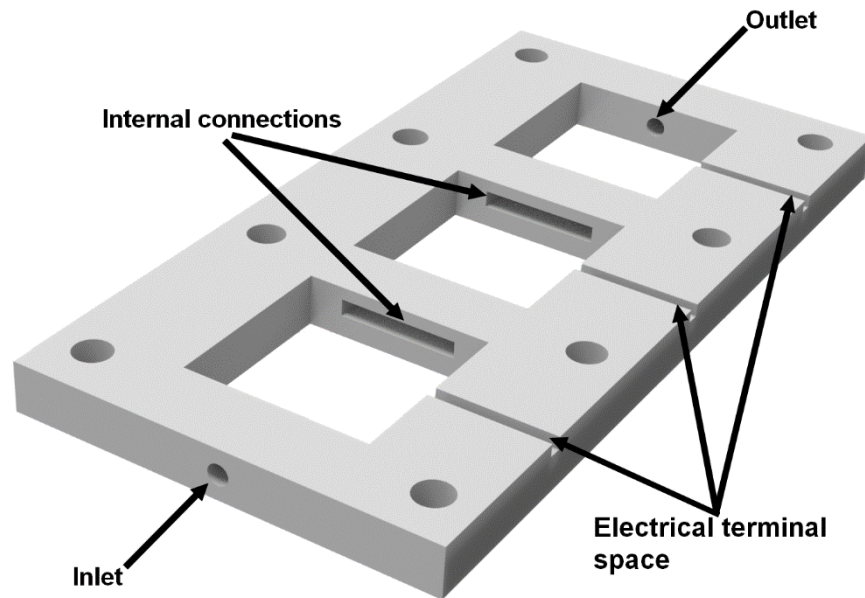


Figure 3.8 Isometric view of the integrated internally connected  $\mu$ -PSC chamber

### 3.4.2. Membrane-Electrode-Assembly

Membrane-electrode-assembly (MEA) is the most critical part of the structural aspect of the  $\mu$ -PSC. It consists of a proton exchange membrane (PEM) and electrically conductive porous electrodes placed on both sides of the PEM. The PEM allows protons to be transferred from the lower potential chamber to the higher potential chamber.

#### 3.4.2.1. Membrane

One of the most widely used PEM in fuel cell technology is Nafion 117, which has an excellent ability in delivering  $H^+$  ions from the anode to the cathode while preventing electrons to pass through. It is an ionic polymer material composed of polyfluorocarbon and highly concentrated pendant sulfuric acid groups that are responsible for increasing the proton transfer phenomenon[57]. The sulfuric acid groups and the amount of water content in the membrane can affect the proton transfer from the anode to the cathode side. Thus, to use a proper PEM for the  $\mu$ -PSC, it is important to pre-treat the Nafion to adjust the amount of water content inside. This phenomenon has been researched and investigated thoroughly in the previous years[81], [82] and the protocol with minor adjustments for the use in  $\mu$ -PSC devices have been provided in [29]. For this research Nafion 117 is selected according to the optimizations that had been done previously[45]. First, it is recommended to cut the Nafion in size of the device and fabrication technique needs. Thus, it is easier to handle these effects on the smaller size rather than treating large sheets. For this research, the active surface area of each cell is designed to be 22mm by 22mm. Therefore, considering the small offset that is required for fabrication, the Nafion cuts of 3cm by 3cm are prepared. Next, Nafion membrane is treated by the following protocol:

- 30 minutes wash in deionized water (DI water) at 70°C, which hydrate the membrane and remove the surface contamination
- 30 minutes in Hydrogen Peroxide (3%) at 70°C to remove the surface organic contaminations
- Three-times wash in DI water each for 30 minutes at 70°C

The above procedure makes the Nafion ready to be used in the  $\mu$ -PSC device. However, due to the fabrication technique which requires bonding the electrodes to the PEM, it is required to keep the treated Nafion in a clean environment (Clean room, class 1000) for 12 hours for the Nafion surface to get dried.

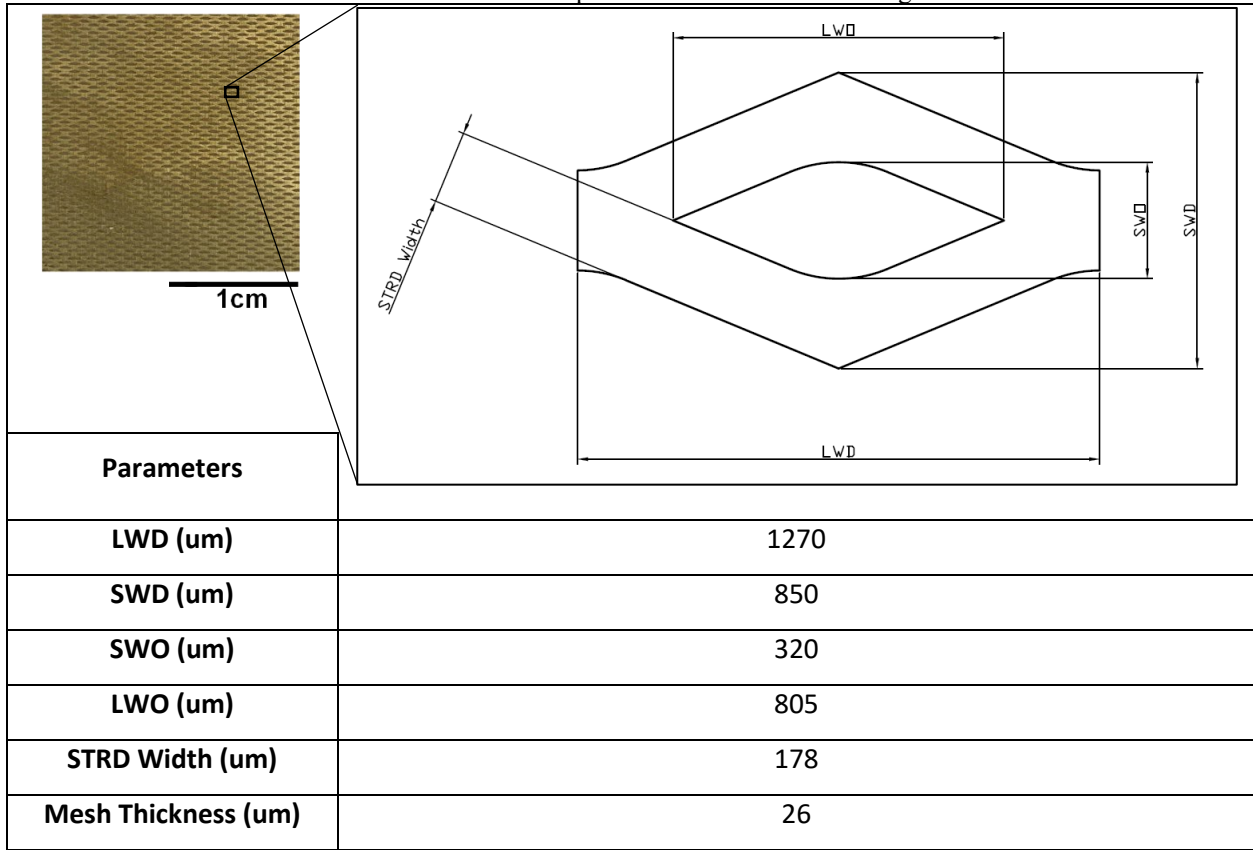
### **3.4.2.2. Electrode Preparation**

Electrodes are the porous component that must be on both sides of PEM and are responsible for collecting the generated electrodes in the anode side and transferring them through an external circuit and release the electrons in the cathode chamber. Various specifications and properties are critical in the design and implementation of electrodes. Due to the fact that living microorganisms present in the system, it is crucial to consider the biocompatibility of the selected material. Noble metals such as Gold provide proper properties in biocompatibility within algae cells[28][83] while providing high electrical conductivity ( $4.42 \times 10^6$  S/m) and chemical stability in contact with other aqueous components in cell media. High electrical conductivity reduces the internal resistance of the device and chemical stability can make sure that there will be no side reactions other than the photosynthesis-related reaction which can damage the cell or increase the noise in output power.

Previously, Gold was directly deposited on the surface of the PEM with specific lithography and sputtering procedure[29]. This method was very expensive and was hard to fabricate. Therefore, a modified method[45] has been developed in the previous research in which the Gold was sputtered on the surface of a thin 25 $\mu$ m Aluminum grid with a thickness of 20nm, and then the prepared component was on both surfaces of PEM. In this method, the fabrication process was easier and the fabrication cost was lower than the previous method.

An alternative method of preparing the electrode is to electroplate gold on the surface of another substrate which satisfies the geometrical need while reducing the overall costs. For this purpose, in this research, a 25 $\mu$ m Aluminum grid with the geometrical specifications provided in Table 3.3 has been prepared by the Dexmet company. The provided mesh has been electroplated with Gold with a thickness of 500nm.

Table 3.3 Geometrical specification of the Aluminum grid



LWD: Long Way of Diamond  
 SWD: Short Way of Diamond  
 LWO: Long Way of Diamond Opening  
 SWO: Short Way of Diamond Opening  
 STRD: Strand

### 3.4.2.3. Assembly

The MEA must be able to function in a wet environment with water as the main component both in the anode and cathode chamber. As recommended from the previous research and the provided technique, Gorilla glue has been used for the assembly of electrodes and PEM. This glue is waterproof and did not show any adverse effect on the PEM functionality.

A less amount of glue has been added on all the sides of PEM to form a continuous narrow line. The electrodes are then placed on both sides and the MEA has been clamped for 90 minutes which is recommended by the manufacturing company. Figure 3.9 provides an image of the MEA after the fabrication. It is important to keep the micro holes in the active surface of the device out of the reach of glue for the ions and electrons be able to be transferred to the cathode chamber. Once the

electrodes have properly attached to the PEM, a narrow conductive mesh has been attached to each of the electrodes to provide spots for electric terminals connection[45].

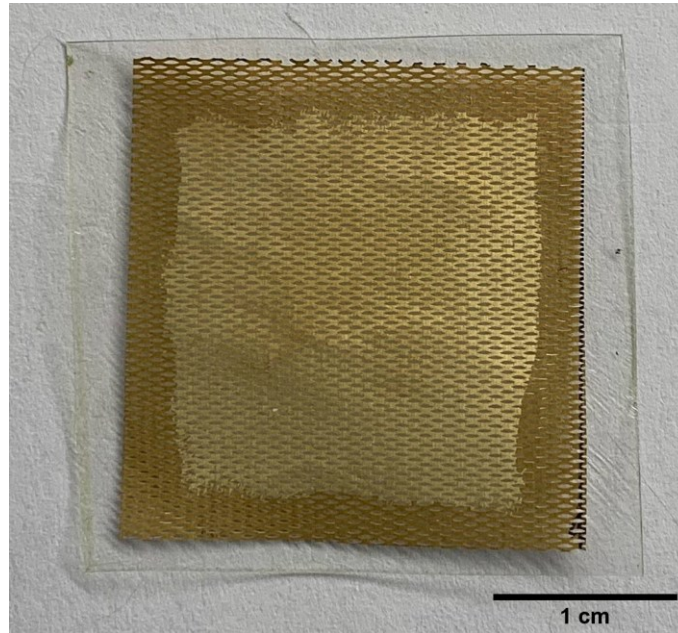


Figure 3.9 Membrane-Electrode Assembly (MEA) view after fabrication

### 3.5. Test Scheme

In order to check the performance of the design, it is crucial to analyze the electrical outputs. The open-circuit voltage (OCV) provides information on the potential of work within the  $\mu$ -PSC device. The short-circuit-current (SCC) shows the maximum amount of current obtained from the device that happens at the near-zero resistance region. Moreover, the variation of cell voltage over current at various amounts of external resistance can help to better understand the device performance, peak power, and electrical behavior of the system. At this point, it can be compared to similar technologies. In addition, it can help in designing dc-dc power converters.

The test setup consists of micro-scale data acquisition[84], with the schematic configurations in Figures 3.10 and 3.11 for the OCV, SCC, and various load resistance measurements. The chip was filled with 8ml of microalgae culture of *Chlamydomonas reinhardtii* as the anolyte, which had been in growing condition for 50 hours at the temperature of 23°C. This is when the cells are in their most active condition in terms of growth and photosynthesis[85]. 8ml of potassium

ferricyanide has been used as the catholyte material. The device has been tested in light conditions with an average light intensity of 300 Lux. The temperature for the experiment was 23°C.

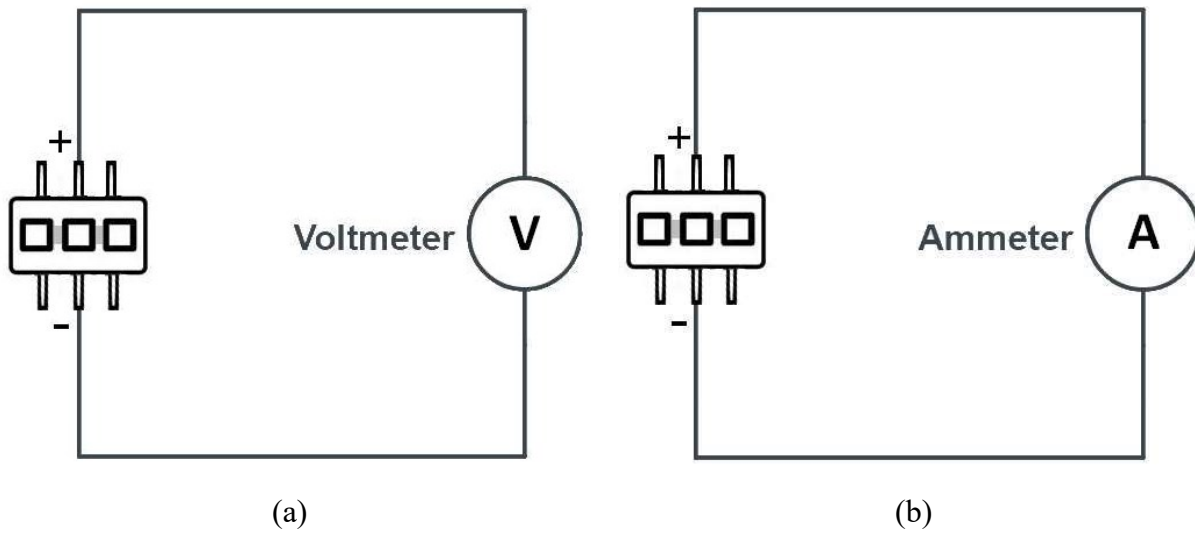
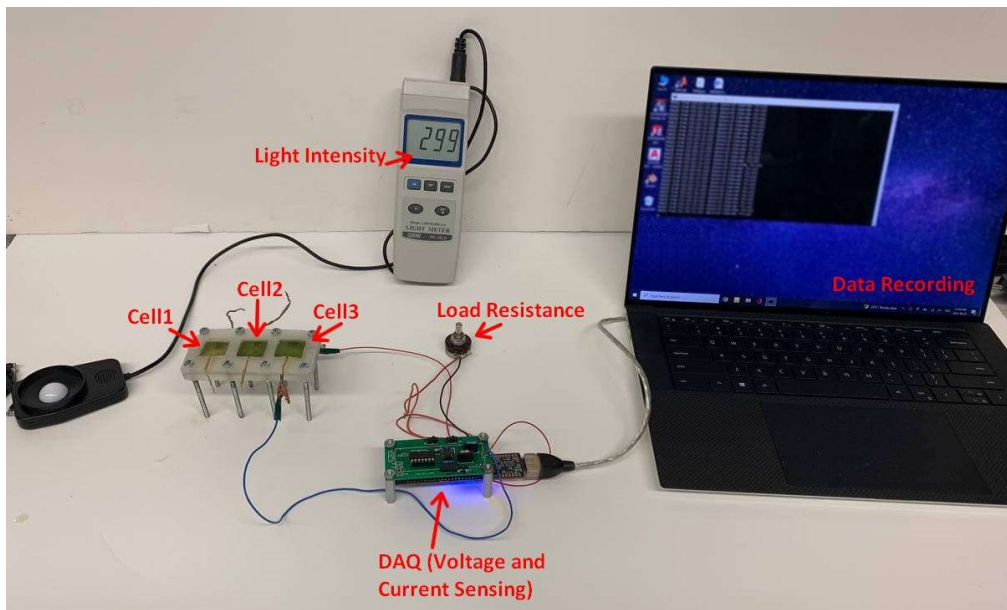
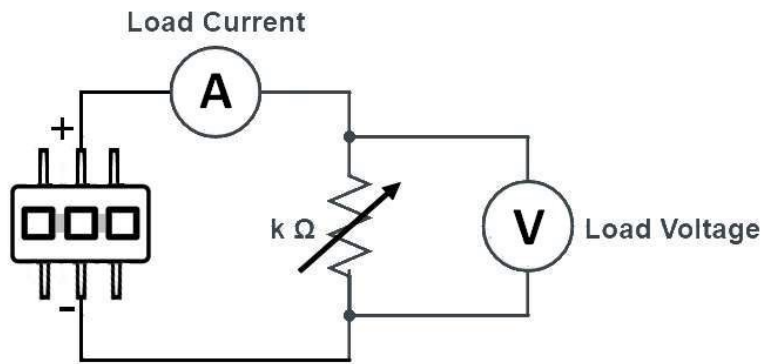


Figure 3.10 General schematic of (a) OCV and (b) SCC electrical circuit measurement for the interconnected array of  $\mu$ -PSC



(a)



(b)

Figure 3.11 (a) Experimental setup of the interconnected array of  $\mu$ -PSC and (b) general schematic of the load current and voltage measurement for the interconnected array of  $\mu$ -PSC

### 3.6. Experimental results

The experiments for the integrated  $\mu$ -PSC have been conducted for each of the  $\mu$ -PSC cells. As the device consists of 3 cells in an array structure, the cells and their electrical connections have been shown by numbers in Figure 3.12. As the cells are internally connected, it is vital to check the effect of internal connections on the outputs of the device.

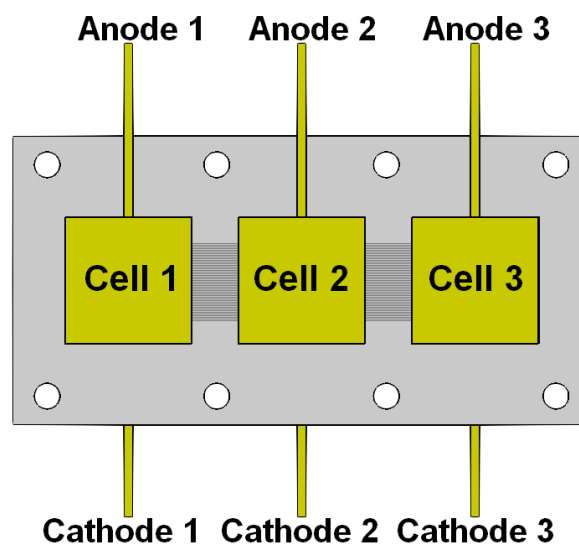


Figure 3.12.  $\mu$ -PSC cells and electrical terminals notation for interconnected design

The OCV data for every two electrical terminals in the Figure 3.12 has been recorded after 15 minutes of anolyte and catholyte addition to let the system reach the steady-state condition. A sample of transient behavior is provided in Figure 3.13. Table 3.4 shows the mean value of the recording of the OCV data with the one unit of standard deviation as the range of variation. Terminal 1 of the voltmeter has been connected to the terminals of the interconnected array of  $\mu$ -PSC. The OCV data has been recorded by connecting the other voltmeter terminal to the other five electrical terminals of the interconnected array of  $\mu$ -PSC one after another.

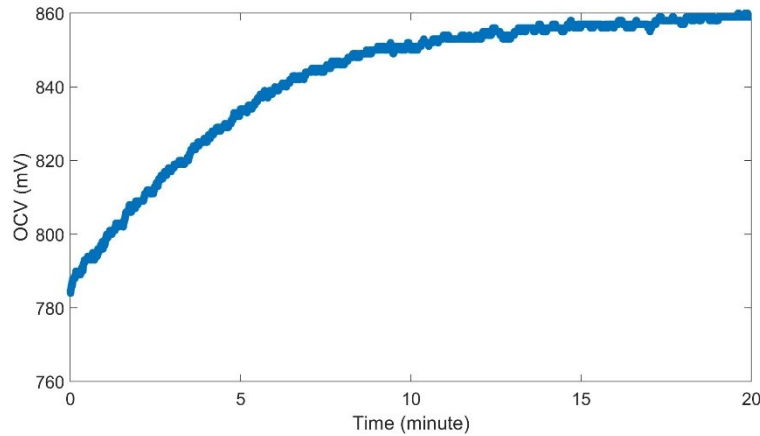


Figure 3.13 Transient behavior of the OCV in the interconnected array of  $\mu$ -PSC

Table 3.4. Variation of OCV at every two terminals of the interconnected  $\mu$ -PSC in mV

Terminal 1	Terminal 2					
	Cathode 1	Cathode 2	Cathode 3	Anode 1	Anode 2	Anode 3
Cathode 1		$59.9 \pm 0.49$	$50 \pm 0.70$	$734.1 \pm 0.32$	$794.7 \pm 0.48$	$549 \pm 0.78$
Cathode 2			$13.2 \pm 0.44$	$816.4 \pm 2.23$	$872.8 \pm 0.38$	$605.1 \pm 1.38$
Cathode 3				$800.1 \pm 0.33$	$836.7 \pm 9.40$	$620.2 \pm 2.48$
Anode 1					$27 \pm 0.53$	$152.7 \pm 1.66$
Anode 2						$191.6 \pm 0.58$
Anode 3						

According to Table 3.4, the potential difference between each cathode probe is very low, showing a relatively uniform electrochemical potential distribution. The same trend can be applied to the results from each two anode terminals. This can also indicate that the cathodes are internally connected with each other as well as the anode chambers. Moreover, the difference can be due to the cells' dynamic and complex biological phenomena taking place in the micro-scale and the minor differences in the fabrication of MEA. It can be seen that each cathode shows a noticeable potential difference when connected to the anode terminals. This could indicate that the electron transfer phenomena may be shared between all three chips when the cells are subjected to external loads. The small output difference can be due to the minor differences in MEA fabrication, microalgae culture dynamics, etc.

Figure 3.14 shows the SCC data between the different cathode and anode connections. In each plot of Figure 3.14, one DAQ terminal is connected to one cathode connection as provided in Figure 3.14, and the other terminal was connected to each anode connection for measurement, one after another. According to the figure, the direct anode-cathode current measurement (e.g., cathode one and anode one) shows a higher value than the cross-connections (e.g., cathode one and anode two). One parameter that can affect the output trend in the cross-connection is the distance between the probes. This trend can be observed when terminal 1 is set to cathode 1 and cathode 3. Once the distance between the measurement probes increases, the output current shows a lower value. Moreover, the cross-connection can cause an increase in the internal resistance of the system, which causes a decrease in the outputs of cross-connection. The direct connection leads to the maximum current output as the electron and proton (mass) transport mainly happens in the same cell. As provided in Figure 3.14, the direct connections show a higher value.

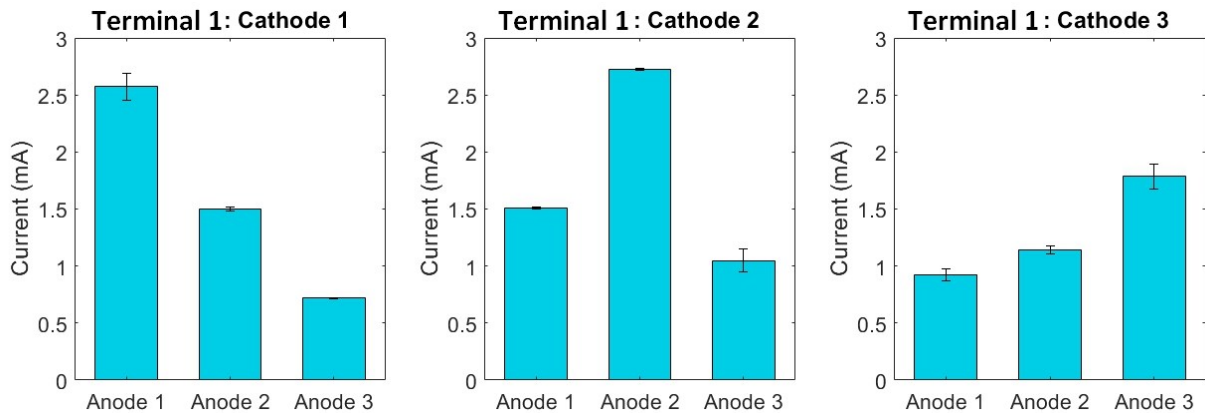
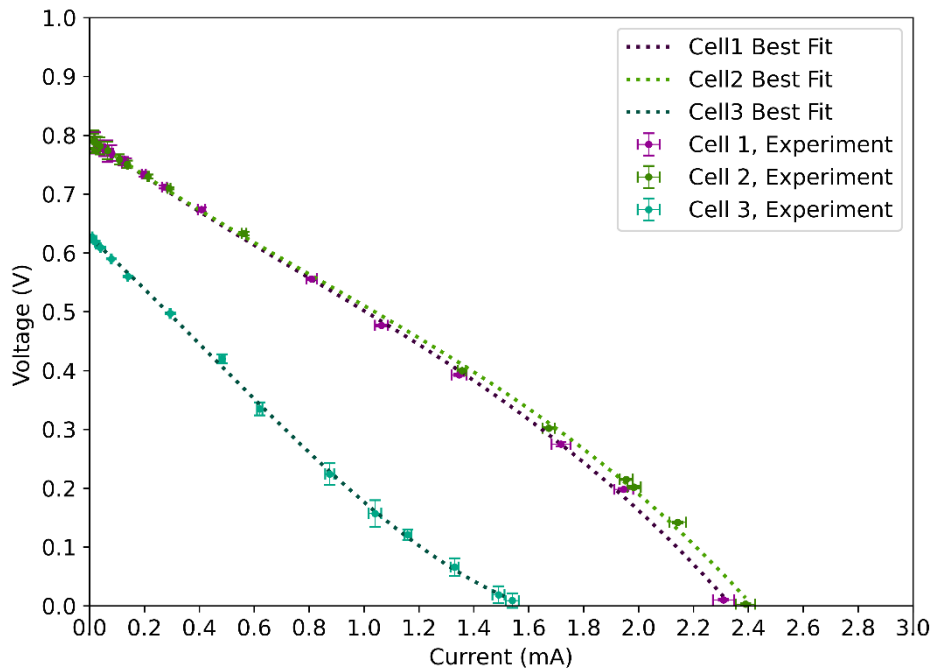


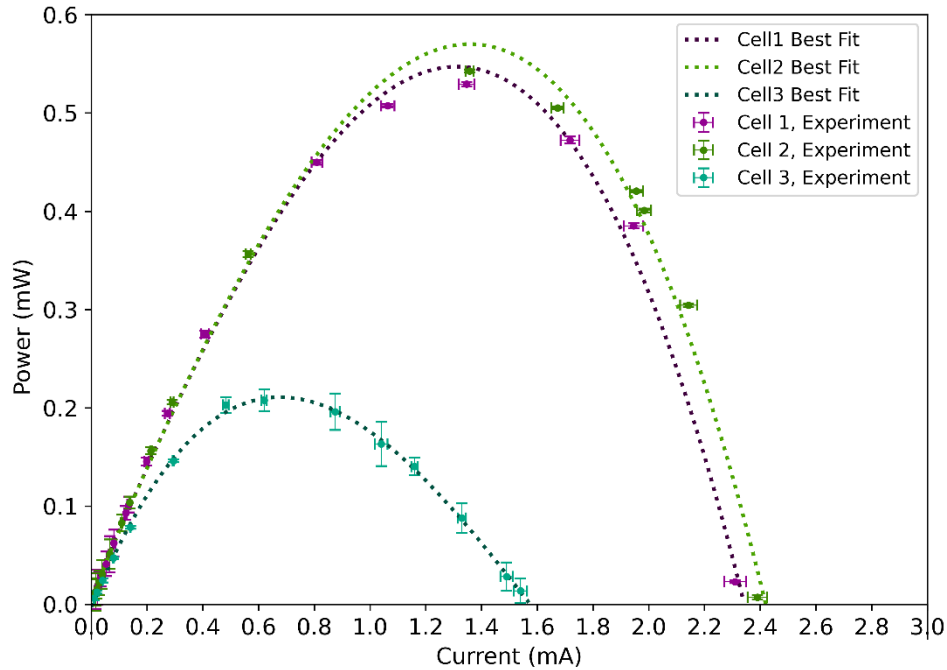
Figure 3.14 SCC data for each electrical connection of the integrated internally connection  $\mu$ -PSC device

There are other parameters that can affect the range of outputs. One main parameter is the quality of the MEA fabrication which can affect the output range. As shown in Table 3.4 and Figure 3.14, one possible reason for the lower outputs in cell 3 can be subjected to the quality of MEA fabrication. The difference in MEA fabrication can results in the enhancement or reduction of electron collection/release of the electrodes.

Figure 3.15 shows the I-V characteristics and power-current curve of each of the cells in the interconnected design. The measurement was obtained one cell after another. According to the Figure, the properly fabricated cells (cell one and cell two) show OCV data of about 800 mV and the near SCC region output of about 2.3 mA to 2.4 mA. Lower values shown in cell 3 data are due to the possible defects in the MEA fabrication, which results in the reduction in its outputs.



(a)



(b)

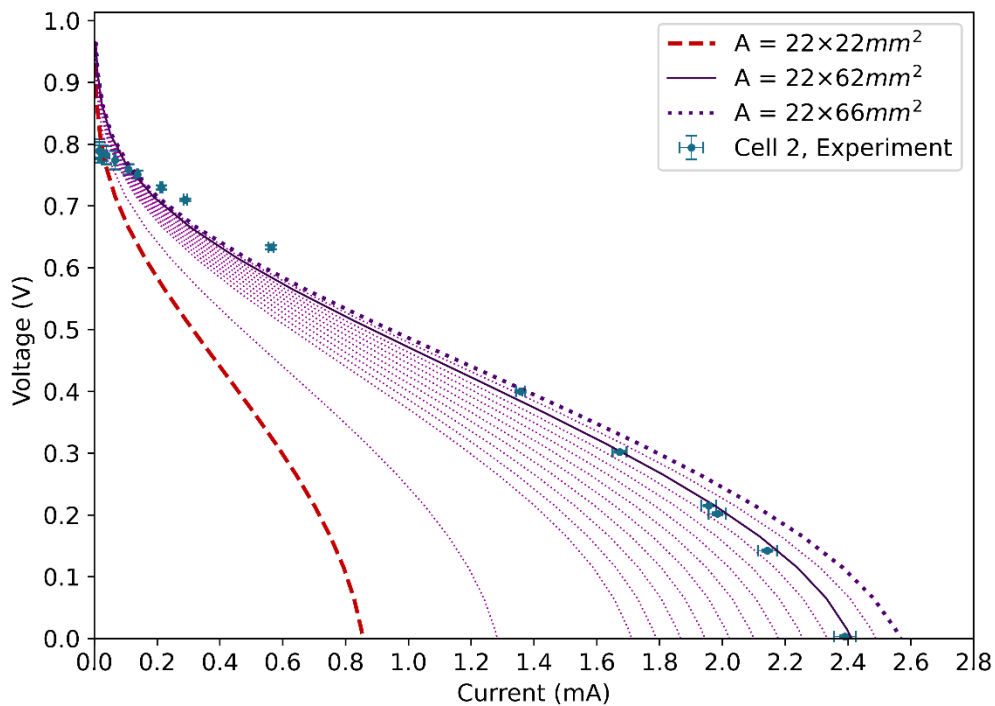
Figure 3.15 (a) I-V characteristics and (b) power-current data of the cells of the interconnected design

According to the previous figures, cell 2 has the maximum output amongst the three cells. The other reason can be due the symmetric location of cell 2, which can use maximum shared electrons from cell 1 and cell 3. In addition, the average output from this cell in this design is almost three times the output obtained from a single cell  $\mu$ -PSC device which can be subjected to the presence of internal connections between the cells. The internal connection which results in the fluid connection, can cause more protons to be transferred due to the presence of three PEM. Generally, one of the limiting factors in PEM-related technologies is the mass transport in the PEM[6], [86], [87]. In a single cell  $\mu$ -PSC, the generated SCC is measured to be about  $840\mu\text{A}$ . In this configuration, the system almost acts as one  $\mu$ -PSC device with a surface area size of three  $22\text{mm}$  by  $22\text{mm}$  chips. This would allow more protons to be transferred while extracting electrons at cell terminals. Therefore, results from cell 2 is will be compared with the model developed in Chapter Two, to understand better the effect of surface area in the interconnected design.

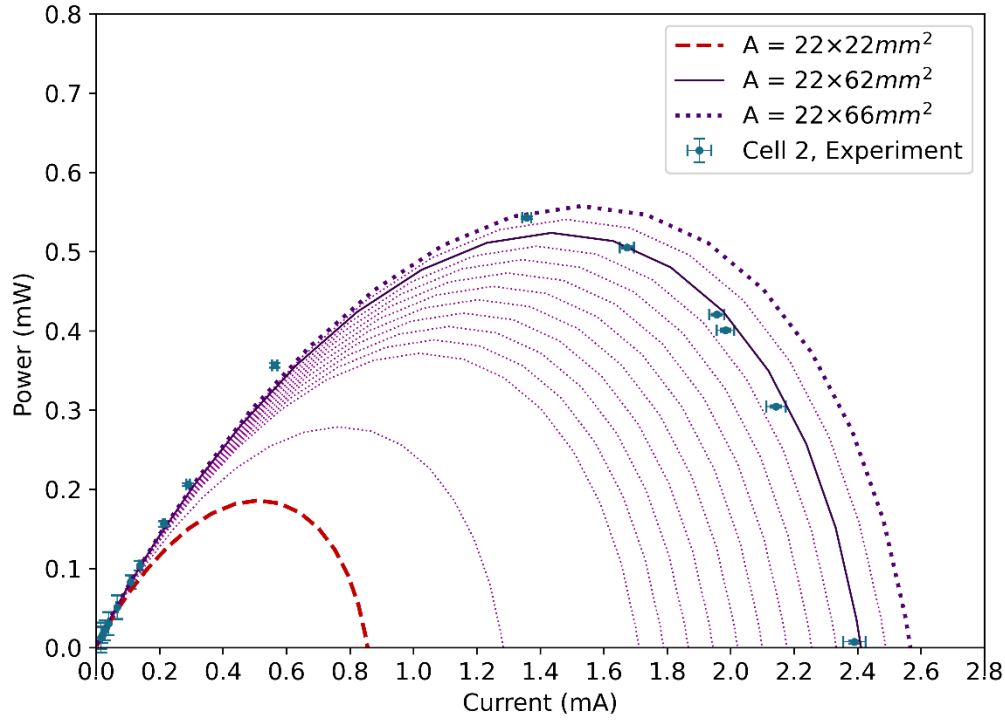
### 3.6. Validation of Modeling and Experiment

According to the previous section, cell 2 provides the maximum electrical output amongst the three cells. In this section, by using the model developed in Chapter Two, it is desired to validate the model at a higher surface area. For this reason, by only changing the length of the model geometry, the I-V characteristics of the  $\mu$ -PSC have been predicted. The length (L) shown in Figure 2.5 value starts from 22mm and increases to 66mm with the step size of 2mm, while the width is kept at 22mm.

In Figure 3.16, the light purple dotted lines show the prediction at various surface areas. By increasing the length of the model, the surface area will increase, and it is expected that the output current should increase. Accordingly, the 22mm $\times$ 22mm prediction and 22mm by 66mm chip prediction have been highlighted with different colors to show the difference in outputs.



(a)



(b)

Figure 3.16 (a) I-V characteristics and (b) power curve for model prediction (shown with lines and dot lines) and experimental data for cell 2 (shown with data points and error bars)

According to Figure 3.16, the interconnected  $\mu$ -PSC is functioning the same as a  $\mu$ -PSC chip with the size of 22mm by 66mm which is three times of a single  $\mu$ -PSC. It can be observed that the experimental data is best fit to the prediction results of 22mm by 62mm chip which is shown by the dark purple line in Figure 3.16. Lower current output in the experimental data can be referred to the presence of internal connections between the adjacent chambers. The model predicts the behavior based on the assumption that the increase in size is continuous in which the 22mm by 66mm chip has one PEM of the same size. However, in the interconnected design, the MEA is separate for each chamber which makes three 22mm by 22mm MEA. Moreover, due to the additional distance which caused by internal connections, the internal resistance of the overall system will increase. In addition, by only collecting the electrons from the middle chamber (Cell 2), a portion of released electrons in chambers 1 and 3 need to be transferred to the middle chamber at which the overall loss and electron collection and respectively lower output current could occur. In other words, the performance of the interconnected array of  $\mu$ -PSC seems to be equivalent to a

single chip  $\mu$ -PSC with a size of 22mm by 62mm. It may not be able to reach the expected results for having three times of the surface area of a single 22mm by 22mm  $\mu$ -PSC.

### **3.7. Conclusion**

In this chapter, an approach in the development of the  $\mu$ -PSC technology has been provided to increase the output current and cell performance. This design was based on designing an array of  $\mu$ -PSC chips into one frame with internal connections. This approach aimed to analyze the effect of internal connection on device performance. The results from this approach show that the OCV from each cell stands in the same range as with the previous designs. The output current shows a noticeable jump. The reason can be due to the presence of internal connections within the cells, allowing more protons to be transferred to the cathode side due to the increase in the active surface area of the device. As this mass transport phenomenon is a limiting factor compared to electron transport, the device almost acts as an  $\mu$ -PSC device with three times a surface area. The results from the most effective chip have also been compared with the modeling results which shows that the performance of the interconnected device is less than the expectations. More investigation can be done in future works to understand the behavior of the interconnected  $\mu$ -PSC.

## **4. Design, Development, and Verification of an Independent Array of Micro-Photosynthetic Power Cell**

### **4.1. Introduction**

Consumption of energy is becoming a critical worldwide concern[88]. Throughout the recent decades, various types of energy harvesting and power generating technologies have been developed which all can be categorized into three subgroups which are fossil fuels, renewable energies, and nuclear energy[89]. Renewable energy can be known as the new trend[1] as it can provide the required power for various applications while being more environmentally friendly than the other two types. A category of renewable energies which create great attention in the past few years is the utilization of biological organisms as the source of power generation, specifically for low-power applications including IoT sensors[48]. Amongst various research, microbial fuel cells and photosynthetic power cells are the ones that show potential.

In the conventional type of these technologies, living microorganisms, including blue-green microalgae cultures or specific types of bacteria, are being used as the anolyte of a two-chamber system which is divided by a membrane-electrode assembly (MEA). Depending on the type of technology, protons and electrons will be released due to either photosynthesis/respiration or metabolic activities of the cells. The electrons are being collected by the electrically conductive electrodes placed on both sides of the proton exchange membrane (PEM) are transferred to an external circuit for power generation. Meanwhile, protons will be passed through the PEM from the anode side to the cathode side. Finally, the electrons reach the cathode chamber from the external circuit, and depending on the chemical components that exist in the cathode side, a set of chemical reactions can happen to finalize the bioelectrochemical reaction chain.

This research mainly focuses on the development of the micro photosynthesis power cell ( $\mu$ -PSC) which utilizes a popular green algae culture known as *Chlamydomonas reinhardtii* CC-125 wild type as the heart of the  $\mu$ -PSC for generating power from the act of photosynthesis in light conditions and the act of respiration in dark conditions[29]. This is the main advantage of the  $\mu$ -PSC over conventional power generation systems, including photovoltaic technology in which the power can only be generated under the light. Still, the development of such a device is in the

research phase and it is important to analyze and optimize different aspects of this evolving technology.

An important aspect of the development of  $\mu$ -PSC, especially for this research, is the design and fabrication technique of an array configuration that is many  $\mu$ -PSC in one chip. It is desired that the design be scaled up with many cells arrayed in one frame. Moreover, within the conventional fabrication technique, the complexity of having an arrayed device with multiple  $\mu$ -PSC will increase dramatically. On the other hand, increasing the complexity causes an increase in the consumption of material, fabrication time, overall cost, and errors that might happen during the fabrication. For these reasons, it is important to develop a fabrication technique that covers the limiting aspects of the previous designs in addition to the fact that the chip material that is going to be used must be compatible with the biological organisms, catholyte material, and cell media.

Previously, several researches have been conducted using different types of materials for the fabrication. McCormick et al.[90] fabricated a chip which consists of a Platinum cathode chamber, a Carbon cloth as the anode connector, PDMS as the gasket to seal the main frame which was made of Perspex glass in a horizontal sandwich. The given design was in contact with the green algae *C. Vulgaris* and cyanobacterium *Synechococcus*. Thorne et al.[91] implemented titanium oxide (TiO) anodes and chemical vapor deposition to coat them with a layer of fluorine-doped tin oxide (FTO) with *Chlorella Vulgaris* biofilms. The power density results showed that the cell is compatible with the given material even though its processes still show complexity and high cost.

Shahparnia[29] provided a new method of fabrication in which the  $\mu$ -PSC device was fabricated by a bio-compatible polymer known as PDMS 184, which was fabricating anode and cathode chambers. The polymer has shaped the chamber by being cured in a predesigned mold. The gold electrodes were sputtered on the surface of the proton exchange membrane with specific geometry and thickness to form the membrane electrode assembly (MEA). Finally, the polymer-based chambers and MEA were bonded together using a PDMS adhesive to prevent leakage within the medium. The proposed technique was successful for research. However, the high cost of preparation including the cost of gold sputtering and fabrication complexity, including the gold sputtering technique, limit its usages.

Kuruvinashetti[45] provides a cheaper fabrication technique for  $\mu$ -PSC devices. In this method, instead of using the direct sputtering technique, the electrodes were fabricated by sputtering 20nm

of gold on a thin aluminum expanded metal with a thickness of 25 $\mu$ m. The electrodes were then stacked to the PEM to form the MEA. This process reduces the complexity of the previous fabrication method while reducing the overall costs. This technique facilitates the fabrication of several  $\mu$ -PSC devices to have the possibility of testing parallel and series combinations of  $\mu$ -PSC devices to attain higher current and voltage. In order to attain the higher values of electrical power, it was required to have multiple single chips which were connected by wires. This makes it hard and less flexible for the system to be transferred, tested with a high number of cells, and more sensitive to physical damages.

This chapter is focused on a modified design to develop an array by having multiple independent  $\mu$ -PSC devices in one solid frame, increases the strength of the frame, makes the device parts reusable, and as a result, reduces the overall cost of the fabrication. The given fabrication technique is provided for 3 $\times$ 1  $\mu$ -PSC chips for the purpose of this research. However, the number can be increased further depending on the need. The active surface area of each cell is kept constant as it has been optimized in previous researches [29].

The experimental tests of the independent arrayed  $\mu$ -PSC provide essential information on device performance while making it possible to evaluate the outputs with the previously designed and fabricated single  $\mu$ -PSC and investigate its functionality. In this chapter, the performance of the independent arrayed  $\mu$ -PSC is examined, and the principal output parameters, including short-circuit current (SCC), open-circuit voltage (OCV), peak power, I-V characteristics, etc. of each cell in the independently arrayed  $\mu$ -PSC are analyzed and compared with the prediction result. The device has been fabricated with EPON 862 resin, following the experiment provided in Chapter Three, for the effect of chamber material on microalgae culture. This resin has higher structural strength compared to the other chosen materials in Chapter Three which is provided in Table 3.1. Higher tensile strength shows that the fabricated part can withstand a higher value of stress while being pulled or stretched before breaking. On the other hand, by preparing a proper mold, multiple series of  $\mu$ -PSC array frames can be produced within less time in case of having arrays with many chips.

The modeling predictions on the behavior of the independent arrayed  $\mu$ -PSC have also been provided, along with the experimental results in the same figures. As the principle of operation of the independently arrayed  $\mu$ -PSC and the single-chip  $\mu$ -PSC, which has been developed in the

previous research, the prediction described in Chapter 2 has been used to predict the behavior of the independently arrayed  $\mu$ -PSC cells. Moreover, the effect of parameters that would affect the outputs is also provided based on the simulation. In the final part, the array design of the three chips in series and the parallel combination has been provided along with the I-V characteristics and power curve of characteristics of different combinations.

## **4.2. Independent Arrayed $\mu$ -PSC Design and Fabrication**

### **4.2.1. Geometry and Design**

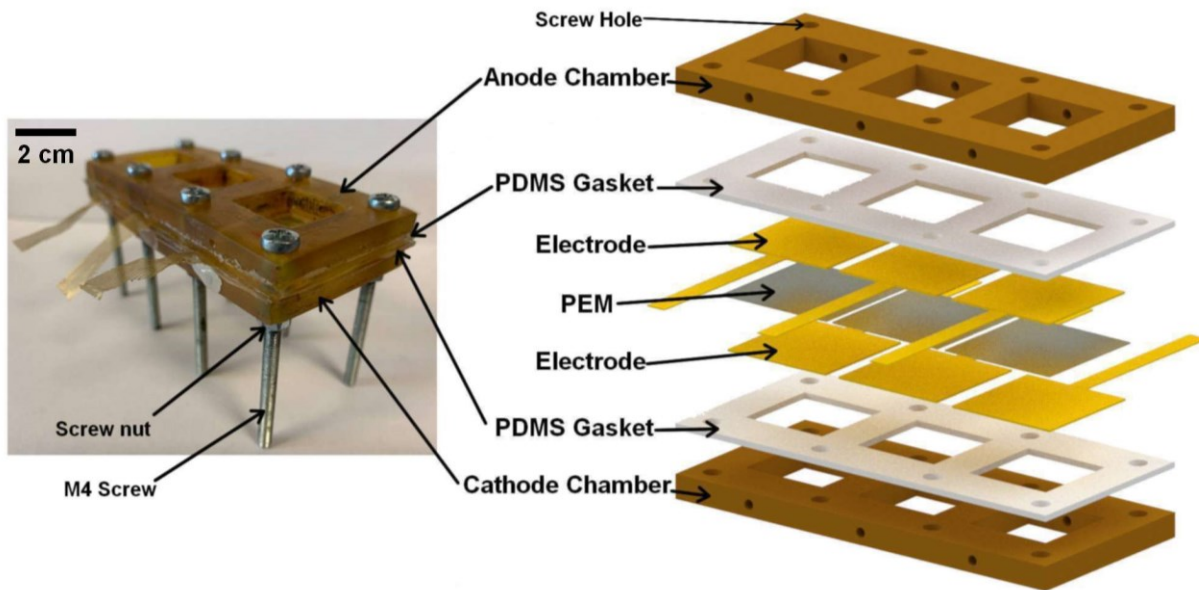
The design in this chapter consists of three  $\mu$ -PSC devices that are arrayed in one frame, as shown in Figure 4.1 (a). This method provides several advantages for future research. It lets the analysis of multiple  $\mu$ -PSC devices obtain a different level of voltage and current depending on the device's performance. Moreover, the fabrication process is more straightforward, and it is possible to add more  $\mu$ -PSC devices to the array in future designs to obtain a higher level of electrical power. One important aspect of the design is to make sure that the anode and cathode chamber are completely separated from each other by the membrane-electrode assembly (MEA). On the other hand, it should be able to assemble the device easily while being able to be disassembled when maintenances and MEA replacements are required.

Figure 4.1 (a) provides the actual fabricated device as well as the exploded view of each part. According to the figure, the independently arrayed  $\mu$ -PSC consists of bonded proton exchange membrane and electrodes, which form the MEA, placed in the middle. Two thin 2mm layers of PDMS have been placed on both sides of the MEA to seal the system and prevent medium leakage during the test. The mentioned parts are sandwiched with the high-strength resin-based anode chamber and cathode chamber frames. The whole structure should be stacked with eight M4 screws and screw nuts.

According to Figure 4.1 (b), the total number of cells in the  $\mu$ -PSC array has been chosen to be three in a row with the single-chip active surface of  $4.84\text{mm}^2$ . The optimum active surface area of the device had been determined previously by Shahparnia[29]. Following the given information for active surface area, the total length for the frame of the  $\mu$ -PSC array is designed to be 106mm

with a gap of 10mm between adjacent chambers. This will provide the possibility of having a proper overlap of 3mm between the MEA and PDMS gaskets while keeping the MEAs separate from each other in the final sandwich structure.

On the sides, the offset from the chamber area to the exterior part is designed to be 13mm. To fix the sandwich structure of the stack design, which includes an anode chamber, MEA, and cathode chamber, eight holes have been placed on the chamber's frame in which M4 screws can be used inside. These screws then should be fastened with proper nuts and tightened with screw nuts. The total thickness of the frame is set to be 6mm. A detailed drawing including full dimensions and views is provided in Figure 4.1 (b).



(a)

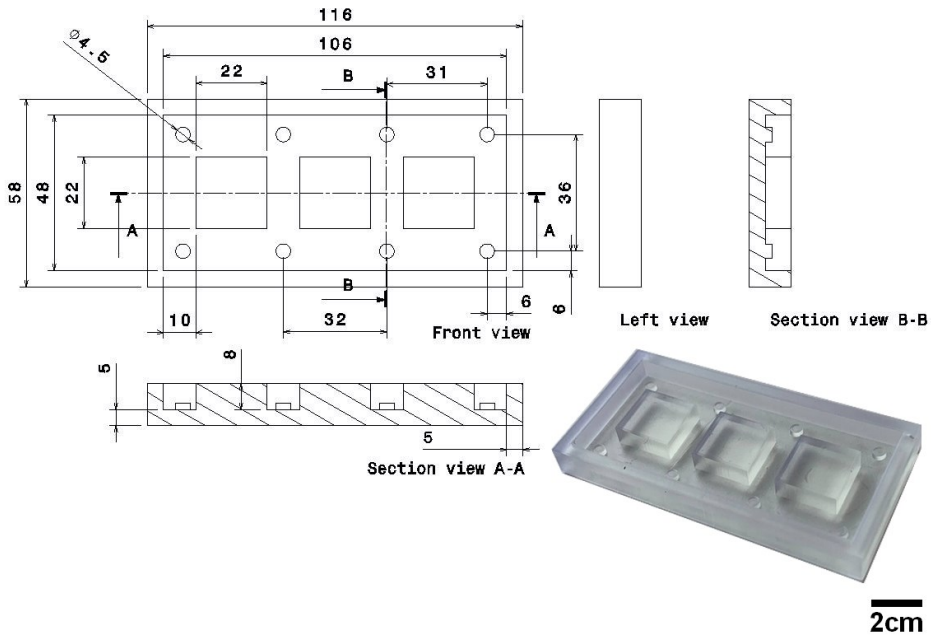
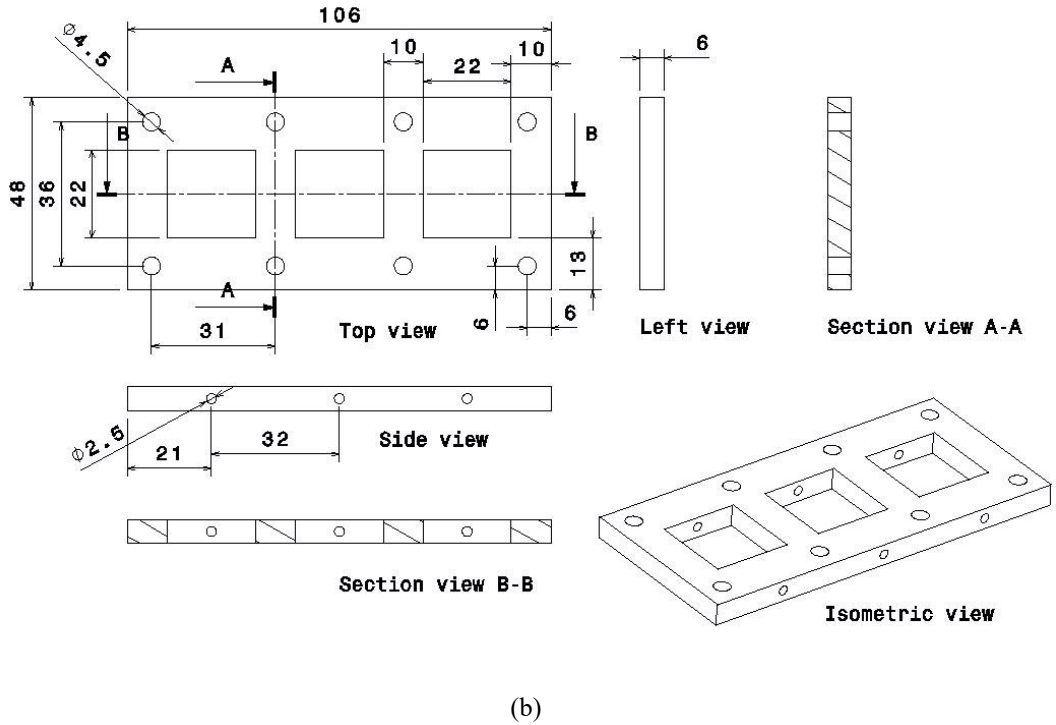


Figure 4.1 (a) Exploded view of the independent arrayed  $\mu$ -PSC and complete geometrical specification\* of (a)  $\mu$ -PSC array and (b) high-temperature resin mold specification\*

\* All dimensions are in millimeter

### 4.2.2. Fabrication Process

To form the chosen epoxy resin EPON 862 into the shape that appeared in Figure 4.1 (b), it is required to prepare a mold in which the mixture of EPON 862 resin and its curing agent (EPIKURE curing agent W) which cure at 160°C, can be molded. The mold has been 3D printed using the SLA printer in order to get a smooth surface, as in Figure 4.1 (c). The mold material should be able to withstand the curing temperature of EPON 862 which is 160°C. Formlabs high-temperature resin and Formlabs flexible resin[92] are two options that can function up to 230°C and is higher than the curing point of EPON 862. Teflon coating spray has been applied to the surface of the mold to minimize the chance of sticking between resin and mold. The wall and substrate thicknesses of the mold are considered to be 5mm.

The EPON 862 resin needs to be mixed with EPIKURE curing agent W with a mixing ratio of 100:26[93]. The added components should be mixed properly for 10 minutes and degassed using a vacuum chamber to remove the trapped air bubbles. Next is the addition of the resin mixture to the mold and cure it for 4 hours at the temperature of 160°C to properly solidify the resin. The cured component needs to be kept at room temperature to cool down. The cured resin forms the anode/cathode chamber of the independently arrayed  $\mu$ -PSC frame, as seen in Figure 4.2 (a).

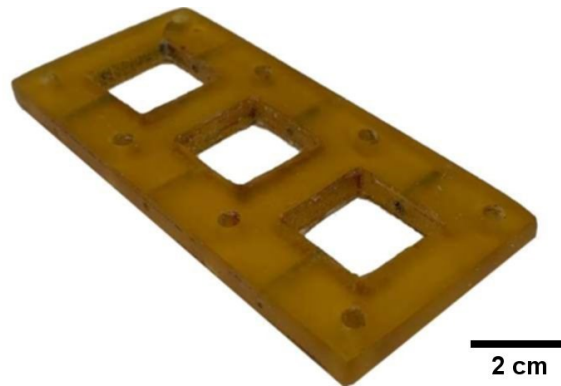


Figure 4.2 Independently arrayed  $\mu$ -PSC frame with EPON 826 and

The fabricated part cannot prevent medium leakage between chambers. This is due to the high tensile modulus of the frame which makes the frame very rigid. Therefore, the addition of a flexible layer that can function as sealing is required. For this purpose, a thin layer of PDMS with a thickness of 2mm is prepared with the ratio of 10:1 and cured in the oven at 60°C for 3 hours. Then, the prepared PDMS gasket layer has been bonded on one side of the frame by a thin film of

PDMS at the ratio of 10:1. The frame and the PDMS layer have been clamped and kept inside the oven at 60°C for 3 hours to bond the PDMS layer to the frame. The frame will be ready for final fabrication after the removal of extra PDMS, as shown in Figure 4.3.

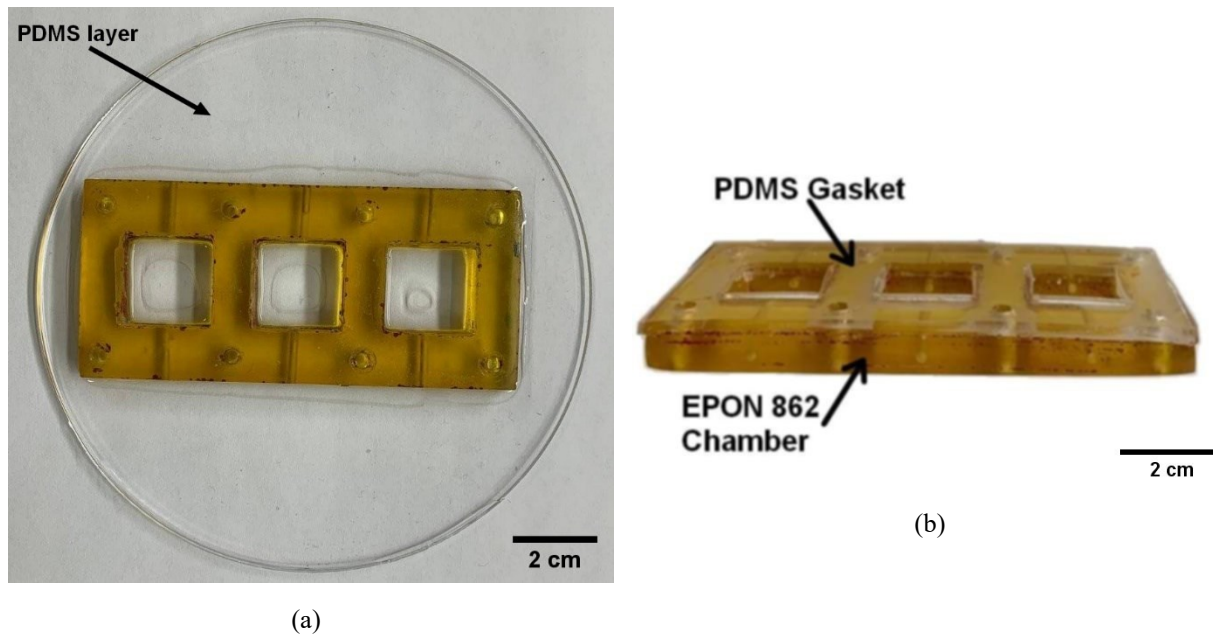


Figure 4.3 Bonded PDMS to the epoxy chamber of independently arrayed  $\mu$ -PSC and (b) final view of the bonded PDMS gasket and chamber after removing extra PDMS layer

The preparation of proton exchange membrane (Nafion 117), gold electrodes and their assembly are explained in detail in Section 3.4.2. the summary of the MEA preparation is as in Table 4.1.

Table 4.1 Summary of MEA preparation steps

Membrane-Electrode-Assembly	<ol style="list-style-type: none"> <li>1. Keep the proton exchange membrane* on a flat surface</li> <li>2. Add a thin layer of Gorilla glue on the edge of proton exchange membrane</li> <li>3. Attach the electrodes** onto the surface of the proton exchange membrane in a way the glue wet the edges of the electrodes</li> <li>4. Clamp the assembly for 90 minutes</li> </ol>
* Proton exchange membrane	<p>Cut into 3cm×3cm pieces and treat as follow:</p> <ol style="list-style-type: none"> <li>1. 30 minutes in Deionized Water at 70°C</li> <li>2. 30 minutes in Hydrogen Peroxide at 70°C</li> <li>3. Three-times wash in DI water each for 30 minutes at 70°C</li> <li>4. Keep in Cleanroom Class 1000 for 12 hours</li> </ol>
** Electrode	<ul style="list-style-type: none"> <li>– Gold electroplating with the thickness of 500nm on a 25μm Aluminum grid sheet</li> <li>– Cut the gold electroplated sheet into 2.5cm×2.5cm pieces</li> </ul>

### 4.2.3. Device Assembly

The assembly of the device includes  $\mu$ -PSC arrayed anode chamber and cathode chamber, three MEAs, eight M4-0.7×60 screws, screw nuts, and lock washers. The screws should be placed on one frame as in Figure 4.4 (a). then the MEAs should be placed on the frame in a way that the MEA not being in contact with each other while filling the chips' surface area. The electrodes are extended by hot melt glue, as in Figure 4.4 (b), for external circuit connection. Next, the second frame is placed to form the exploded view as in Figure 4.4 (c). The lock washer can be added to screws and tightening of the nuts as much as the gaps between two PDMS gaskets are removed, as shown in Figure 4.4 (d). Maximum tightening can cause breaks inside the PDMS layer which can cause media leakage, chambers connections, and MEA damage. Figure 4.4 shows the process of the device assembly. The bottom frame should be covered with glass and be used as the cathode chamber. The small holes on the sides of the frame can be used for media exchange. Once the cathodes are filled with media, the small 2.5mm holes on the sides need to be closed by hot melt glue.

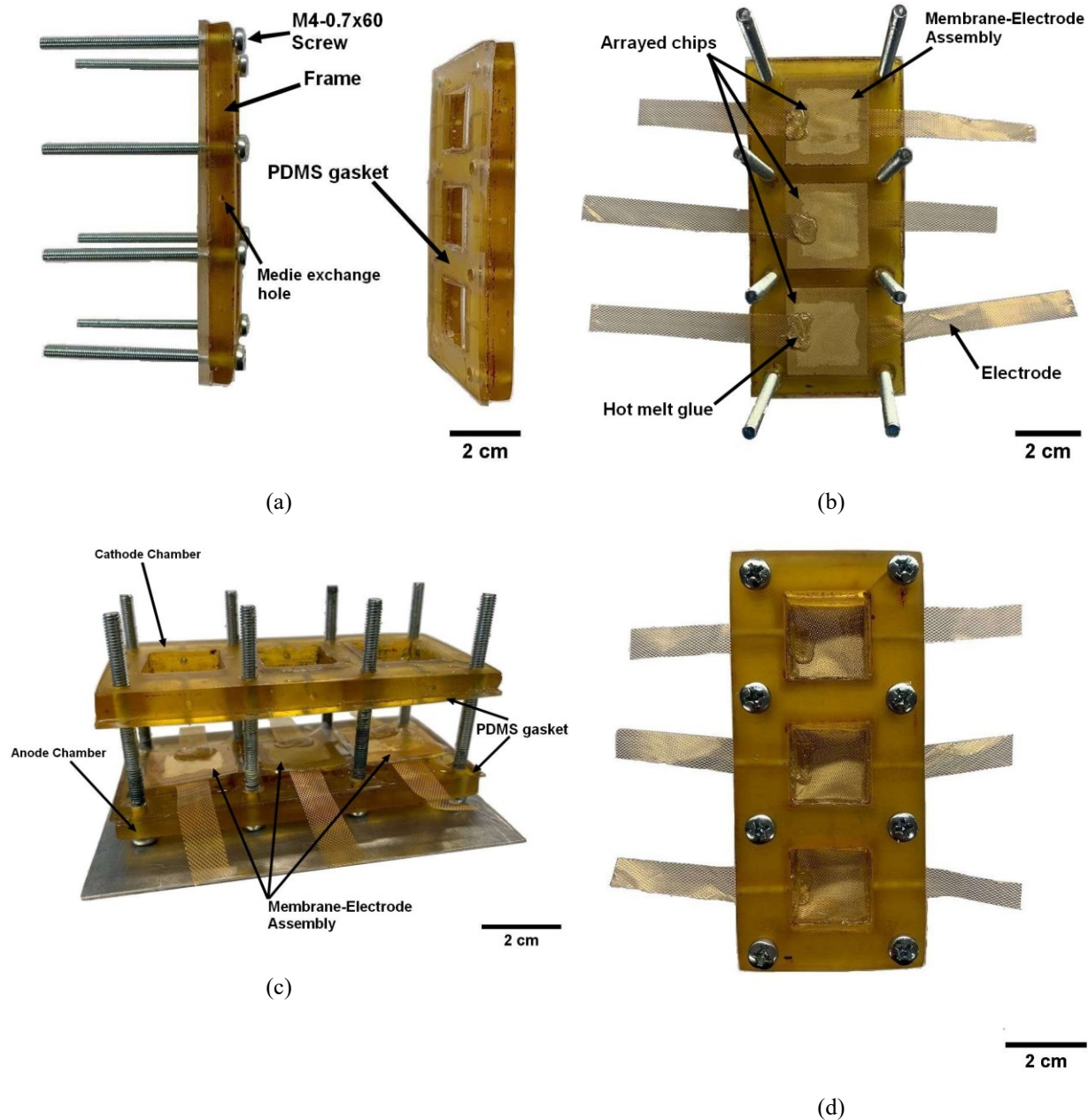


Figure 4.4 Final Assembly of the  $\mu$ -PSC array design

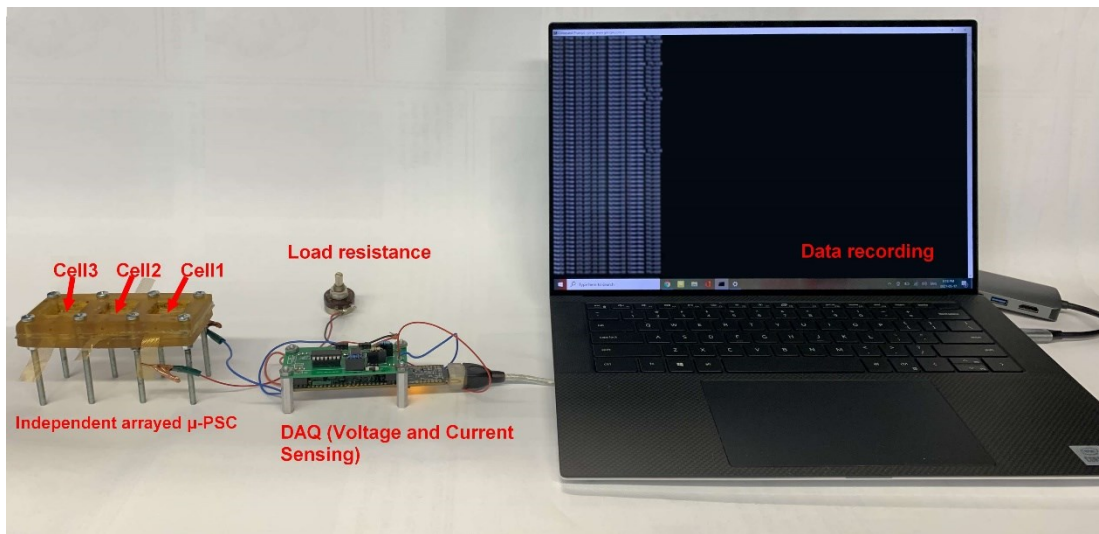
### 4.3. Experiment Condition and Setup

All the tests in the experimental phase of the Independent arrayed  $\mu$ -PSC has been taken at 23°C under the light intensity of about 300lux. The algae cell culture which has been used for this research is *Chlamydomonas reinhardtii* CC-125 wild type which is a widely used microalgae culture in photosynthesis studies. The cells have been culture and suspended in the cell culture

medium of Tris-Acetate-Phosphate solution (TAP medium) for 48 hours at the temperature of 23°C as from this time, and the cells are in their most active condition in terms of division, growth, and photosynthesis. The total volume of the microalgae culture added to each anode chamber was 2.5ml.

The effect of potassium ferricyanide concentration as the catholyte on the performance of the  $\mu$ -PSC has been thoroughly investigated by Shahparnia[29]. It has been observed that the increase in the concentration of potassium ferricyanide increases the cell voltage. However, at concentrations above 25% w/v (25gr/100ml), the OCV will be saturated. Accordingly, the optimal concentration of 25% w/v has been prepared and implemented for the evaluation of the Independently arrayed  $\mu$ -PSC. A volume of 2.5ml of potassium ferricyanide has been added to the cathode chamber.

The experimental setup consists of the Independently arrayed  $\mu$ -PSC, which has been connected to a precise current-voltage sensing DAQ and a variable rheostat as load resistance with the range of 0-50k $\Omega$  for loading and I-V characteristics measurements. The whole setup is then connected to a computer for recording the data. The overall view of the test setup is provided in Figure 4.5 (a). Moreover, the schematic of the OCV, SCC, load voltage and load current measurement circuits are provided in Figure 4.5 (b-d).



(a)

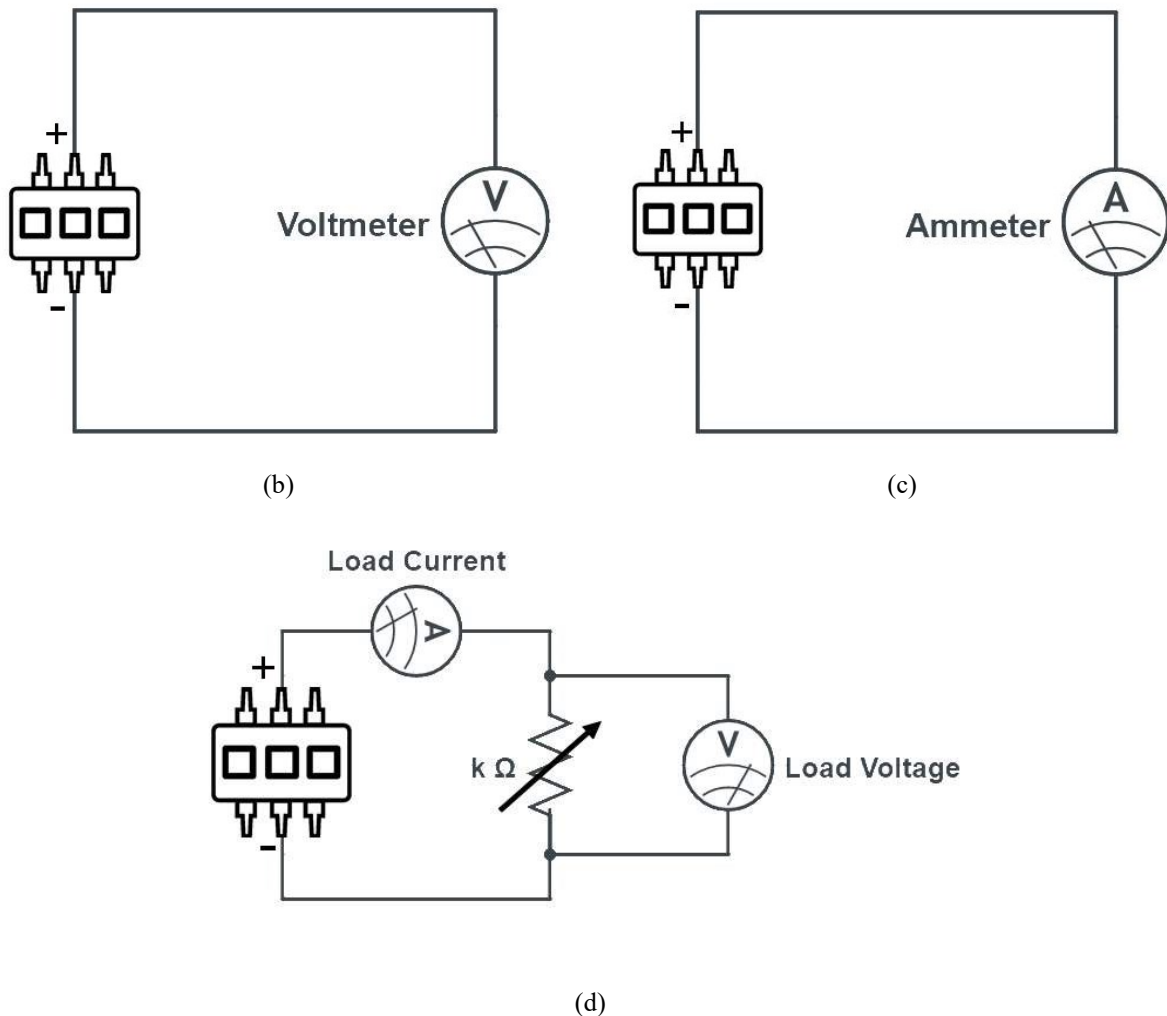


Figure 4.5 Overall view Experiment setup of the Independent arrayed  $\mu$ -PSC

## 4.4. Experimental Characterization

### 4.4.1. Open-Circuit Voltage

The open-circuit voltage (OCV) is the voltage of the  $\mu$ -PSC at zero current, and it defines the electrochemical potential of the cell. Theoretically, it is the maximum voltage that could be generated by a typical power generating device which is due to the electrochemical potential difference of the biological and chemical compounds in the anode and cathode chambers. Generally, the OCV of the  $\mu$ -PSC varied from 0.6 to 1V. Voltage has been recorded for each of the cells in the Independent arrayed  $\mu$ -PSC by connecting the DAQ to the anode and cathode terminals of each cell with the schematic configuration as in figure 4.5 (b). In addition to the

theoretical definition, the fabrication quality of the membrane-electrodes assembly (MEA) and microorganisms' dynamics affect the maximum possible voltage. Poorly fabricated MEA, including inappropriate adhesion of the electrodes to the PEM, can also result in low OCV.

For the comparative analysis between the Independently arrayed  $\mu$ -PSC cells, Figure 4.6 has been provided, demonstrating the recorded OCV data for each of the three cells of the Independent arrayed  $\mu$ -PSC for 60 minutes. The results show a stable trend in each of the cells in the recording duration, which shows the stable potential of work for the device. The range of OCV variation is in the range of 750mV to 820mV.

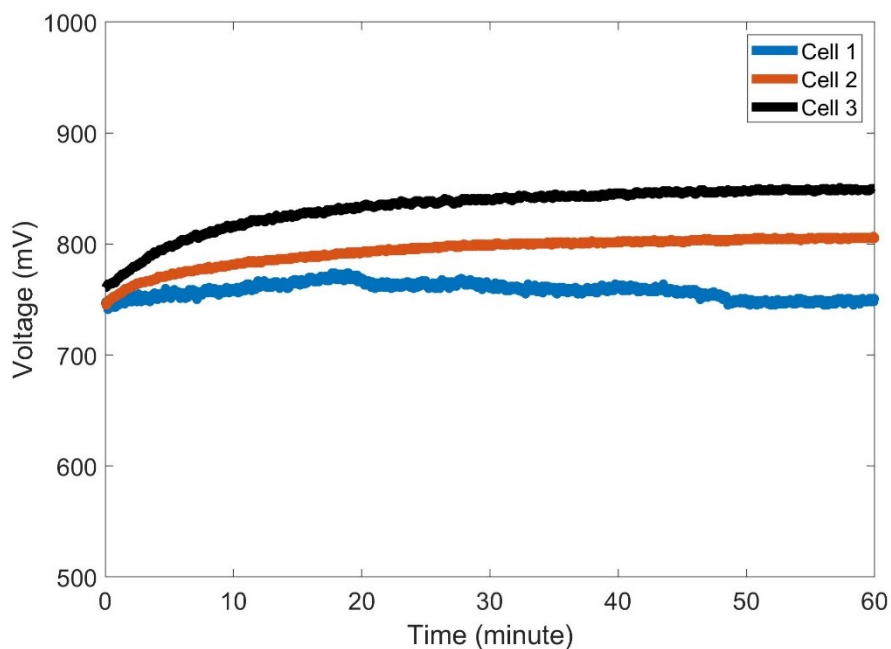


Figure 4.6 OCV data for 60 minutes test of each chip in the Independently arrayed  $\mu$ -PSC

The cell voltage has also been observed for 72 hours, as in Figure 4.7, which shows the Independent arrayed  $\mu$ -PSC could generate stable OCV for cell 1 as an example. As the anode side is open to the air and has not been isolated as the cells require carbon dioxide and oxygen for photosynthesis and respiration, the amount of cell media in the anode chamber decreases over time due to the surface evaporation. Thus, the OCV shows a reducing pattern from the measurement at time zero. However, with the addition of cell media at different times, approximately every 24 hours, the OCV value increases again.

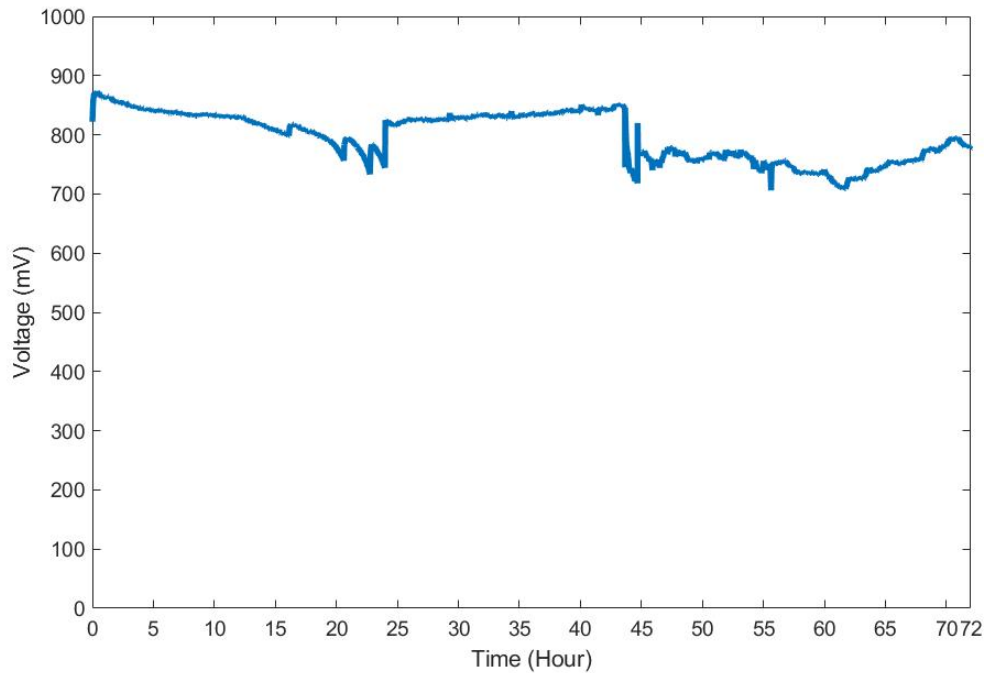


Figure 4.7 Long-term OCV data observation of the Independent arrayed  $\mu$ -PSC

#### 4.4.2. Short-Circuit Current

The short-circuit current (SCC) is the generated current due to the flow of electrons through the external circuit at zero or very low electrical impedance in which the voltage across the power cell is zero. It is also showing the maximum current which can be generated by any typical power generation device.

In order to observe the SCC of each chip of the Independently arrayed  $\mu$ -PSC, the current sensing unit was connected to the electrodes of each chip as in Figure 4.5 (c). The SCC has been recorded for 10 minutes for five times, and the average value of each chip with the error bars showing the range of variation has been calculated. The SCC data has been provided in Figure 4.8.

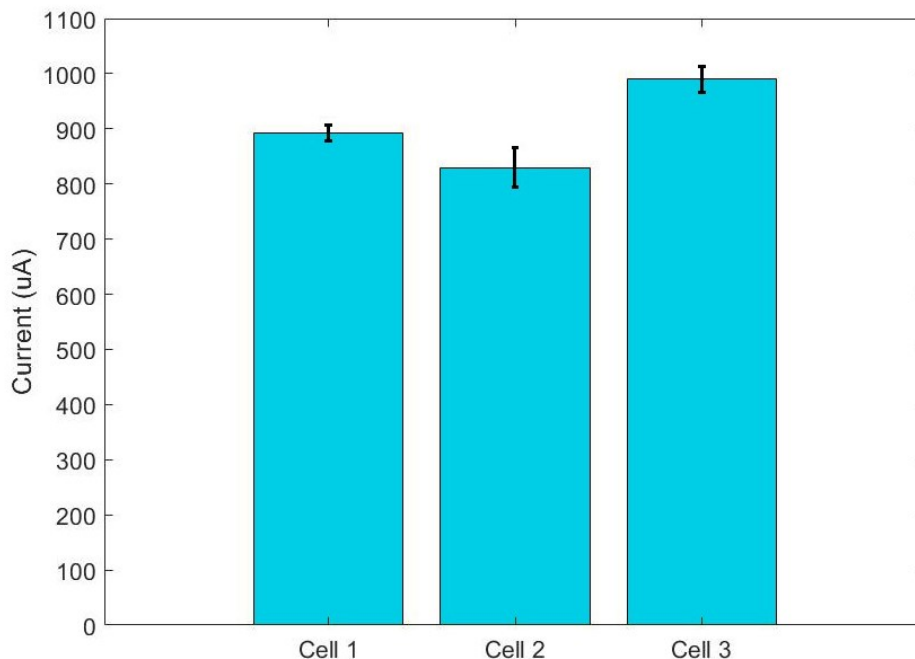


Figure 4.8 Short-circuit current data for each chip of the independently arrayed  $\mu$ -PSC with the error bars showing one unit of standard deviation of the collected data

According to the measurements, the range of SCC is between 800uA to 1000uA. The variation in SCC data of each cell can be due to the fabrication quality, dynamics of the microalgae culture, etc. The better the electrodes bond to the PEM, the higher and more stable results can be obtained. On the other hand, due to the presence of biological organisms in the  $\mu$ -PSC technology, there will be an inherent variation due to the dynamics of the microalgae behavior, which has been illustrated using the error bar in Figure 4.8.

#### 4.4.3. Constant Loading Characterization

$\mu$ -PSC technology is developed to power up sensors and many other devices requiring low power to operate. For this reason, it is vital to analyze the  $\mu$ -PSC outputs at different loading conditions. For this purpose, the performance of the independent arrayed  $\mu$ -PSC chips has been observed within different constant electrical loadings. The electrical circuit provided in Figure 4.5 (d) has been used to monitor the load current and load voltage for different constant load resistance values over a period of time. The results have been observed for this stage and provided in cell current and voltage variation over time and the average value of cell voltage and current within different

loadings. In Figure 4.9, the observation of load voltage and load current has been provided for 60 minutes of each of the independent arrayed  $\mu$ -PSC chips at connecting the  $1k\Omega$  of external load. The results show a stable trend within the time span of 60 minutes. The range of voltage variation is between 470mV and 380mV, and the variation in the current data is within almost the same range. The reason behind this variation can be referred to the biological dynamics of the algal cells.

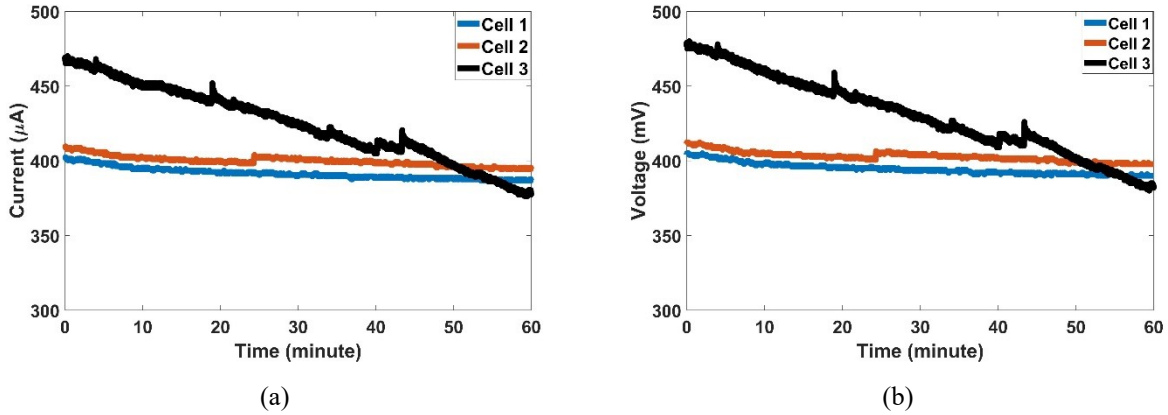


Figure 4.9  $1k\Omega$  loading data of (a) load current and (b) load voltage in 60 minutes

Based on the trend of the load voltage and load current variation for  $1k\Omega$  of constant loading, the load voltage and load current measurement for the other constant loadings has been provided in Table 4.2 with the duration 10 minutes record for each. According to Table 4.2, the device can generate a load voltage of 85 to 105 mV at the load of  $0.1 k\Omega$ , and the voltage of 750 to 840 mV at  $10k\Omega$ . Respectively, the cells providing a current of 0.81mA to 1.05mA at the load of  $0.1 k\Omega$  and 73 to  $84\mu A$  at a load equal to  $10k\Omega$ . With the increase in load resistance, the electron flow decreases and causes a more accumulation of electrons in each chamber which leads to an increase in cell voltage.

Table 4.2 The load voltage and load current of each chip of the independently arrayed  $\mu$ -PSC at various constant loadings (range of variation is equal to one unit of standard deviation of the recording data)

Parameter	Chip number	Constant Load Resistance Value				
		$0.1 k\Omega$	$0.5 k\Omega$	$2 k\Omega$	$5 k\Omega$	$10 k\Omega$
Load Voltage (mV)	1	$81 \pm 4$	$289 \pm 3$	$567 \pm 6$	$683 \pm 3$	$739 \pm 3$
	2	$83 \pm 3$	$302 \pm 5$	$798 \pm 4$	$742 \pm 4$	$807 \pm 3$
	3	$106 \pm 4$	$361 \pm 4$	$658 \pm 3$	$789 \pm 2$	$843 \pm 3$
Load Current (mA)	1	$0.81 \pm 0.020$	$0.57 \pm 0.015$	$0.27 \pm 0.030$	$0.13 \pm 0.012$	$0.07 \pm 0.013$
	2	$0.83 \pm 0.015$	$0.60 \pm 0.025$	$0.29 \pm 0.020$	$0.14 \pm 0.017$	$0.08 \pm 0.014$
	3	$1.05 \pm 0.017$	$0.72 \pm 0.019$	$0.33 \pm 0.015$	$0.16 \pm 0.008$	$0.08 \pm 0.008$

#### 4.4.4. I-V Characteristics

One of the main parameters in the analysis of the behavior of any power generating device is the characteristics of the voltage over current, which is also known as I-V characteristics, and the corresponding curve is known as the polarization curve. The captured data from this curve can be employed to design a more efficient power converter for power generating instruments, including  $\mu$ -PSC devices.

The setup configuration is the same as the schematic provided in Figure 4.5 (d). Instead of placing a constant resistance, a rheostat load with the range of 0-50k $\Omega$  has been placed in the circuit. The direction of resistance change is from the maximum load resistance value near the OCV domain toward minimum resistance near the SCC domain. The total number of 12 to 15 data points have been collected in three trials for each chip of the Independent arrayed  $\mu$ -PSC. The provided results include the average point of the three trials recording and the error bar representing the current and voltage variation among three trials. In addition, the modeling results have been provided along with the experimental results. Two numerical parameters that cannot be measured directly for the  $\mu$ -PSC have been tuned up which limiting current density and PEM conductivity. This is because the proton exchange membrane shows deformation after some time and when contact with cell culture media in anode chamber or Potassium Ferricyanide in cathode chamber which both the mediums contain water. In a properly fabricated MEA, the electrodes are well-bonded to the membrane, and the gap between the electrodes and the membrane will be very low. However, the deformation can increase or decrease the distance between the PEM surface with electrodes which can affect the number of participating algae cells in  $\mu$ -PSC power generation. In other words, the concentration of participating species, which are algae cells in the anode chamber and Potassium Ferricyanide in the cathode chamber, will change near the electrode surface which can directly alter the limiting current density[10] in the model that is associated with the effect of species concentration on the concentration loss. The deformation can also cause delamination of electrodes from PEM, and the change in the conductivity of PEM[94], which can affect also affect the performance of  $\mu$ -PSC. Figure 4.10 provides the MEA deformations of the independently arrayed  $\mu$ -PSC chips. According to the images captured after the test, the deformation in cell 3 is less than cell 1 and cell 2 and the delamination of electrodes is far less in cell 3, respectively which can be

the reason for better electrical behavior in comparison with the cell 1 and cell 2 in the independently arrayed  $\mu$ -PSC.

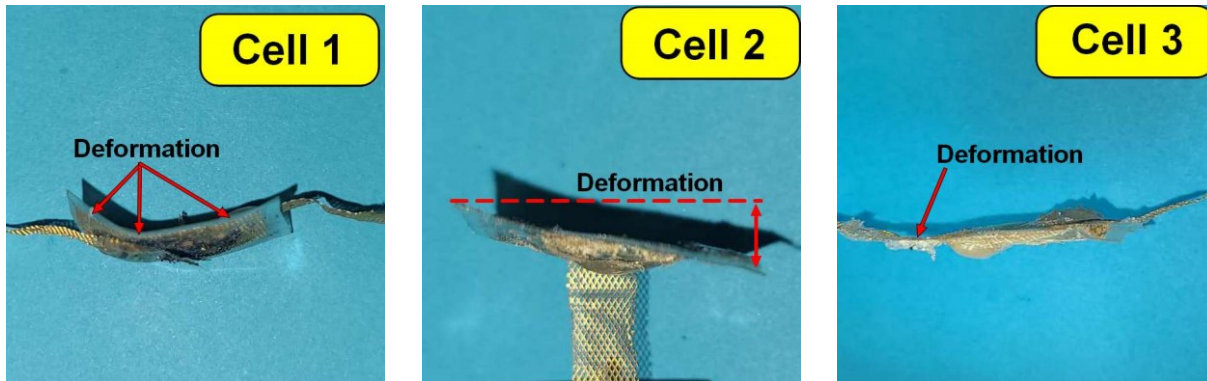


Figure 4.10 Proton exchange membranes deformation image after the test of independently arrayed  $\mu$ -PSC

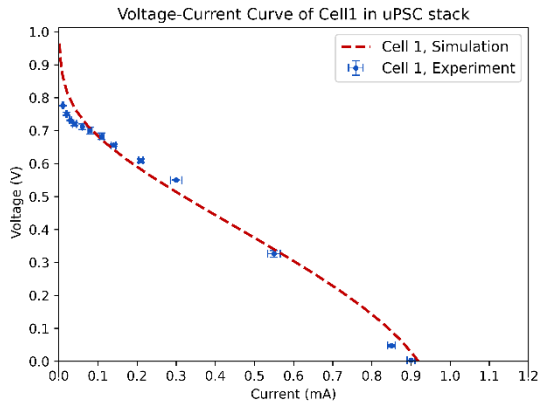
Table 4.3 provides the parameter changes for the modeling of each of the cells of the Independent arrayed  $\mu$ -PSC which is defined mainly within a range depending on the application and fabrication technique[25], [53], [84]. For the independently arrayed  $\mu$ -PSC, it is defined in a range between 1.818 to 2.318. The mentioned reason may also affect the number of protons that can be transferred through the PEM as the condition for this occurrence is more plausible when the MEA is properly fabricated. As a result, this can be observed as a change in the PEM conductivity both in experimental data and modeling. The PEM conductivity can be varied from 0.01 to 0.2 S/cm[56], [95]. Moreover, the best fit from the modeling will be used for the calculation of fill factor of each chip in the independently arrayed  $\mu$ -PSC.

Table 4.3 Simulation parameter change for Independent arrayed  $\mu$ -PSC

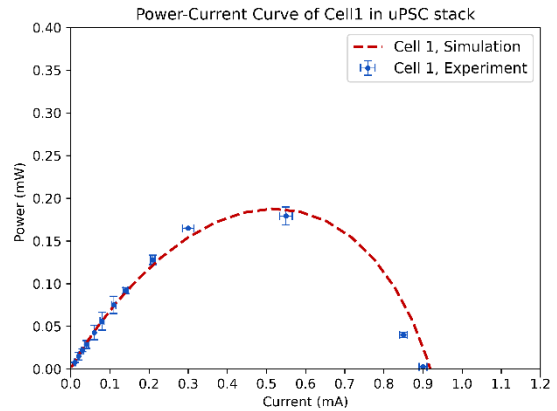
Parameter	Cell 1	Cell 2	Cell 3
Limiting current density ( $A/m^2$ )	1.818	1.918	2.318
PEM conductivity (S/cm)	0.12	0.10	0.20

Figure 4.11 shows the I-V characteristics and the respective power-current curve of each of the cells in the independently arrayed  $\mu$ -PSC. The blue dots with the ranges represent the average value of the experimental data and the maximum and minimum value through the errors, which have been obtained in a three-trial data recording for each chip. The red lines represent the simulation results which has been obtained from the model provided in chapter 2 with the change in parameters as provided in Table 4.3. For all three cells, the voltage starts at about 0.8 V, which

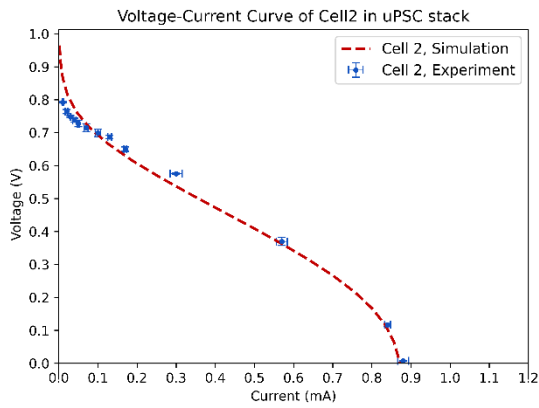
follows the same trend as with other design provided in chapters Three. The current value at the SCC region is different for each cell. This is due to the mentioned reasons and considering that in contrast to the OCV, the output current is heavily dependent on the quality of the fabrication and nuanced differences in the fabrication of MEA, leading to the difference in answers. Accordingly, it seems that the quality of cell 3 is slightly better than the other two cells.



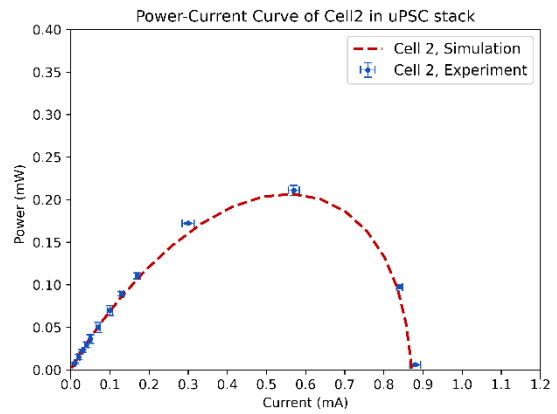
(a)



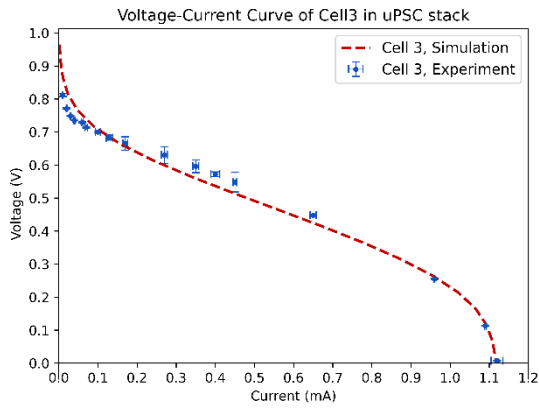
(b)



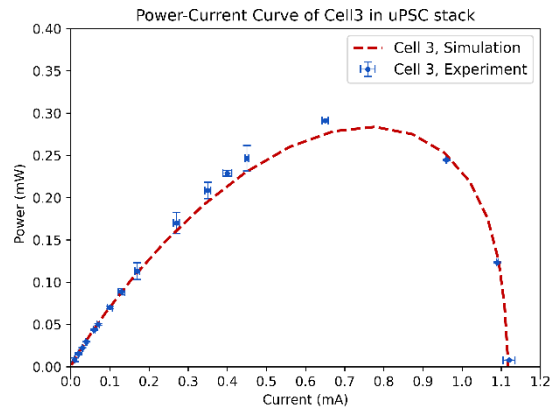
(c)



(d)



(e)



(f)

Figure 4.11 (a), (c), (e) I-V characteristics and (b), (d), (f) power-current curve of the Independent arrayed  $\mu$ -PSC cells

Figure 4.12 shows the variation of  $\mu$ -PSC peak power at various limiting current densities and PEM conductivity. The figure has been plotted with the  $\mu$ -PSC power prediction with 20 equally spaced values for limiting current density starting from 1.5 to 2.5 A/m<sup>2</sup> and the PEM conductivity from 1 to 20 S/m. According to the figure, the cell peak power is more influenced by the PEM conductivity than the limiting current density. The reason is the cell performance is more dependent on the proton transfer among the PEM. The higher the proton conductivity is, the higher the electrical power that can be obtained from the  $\mu$ -PSC. Limiting current density only shows the maximum current that a  $\mu$ -PSC can produce, which is why it cannot increase the peak power by itself. In other words, limiting current density alter the capacity for acquiring maximum current which also can lead to the rise in peak power if the PEM conductivity is also high. The scattered points in Figure 4.12 show the prediction values for the independently arrayed  $\mu$ -PSC cells' peak power at various limiting current densities and PEM conductivity in which a well-fabricated chip can function at higher limiting current densities and PEM conductivities.

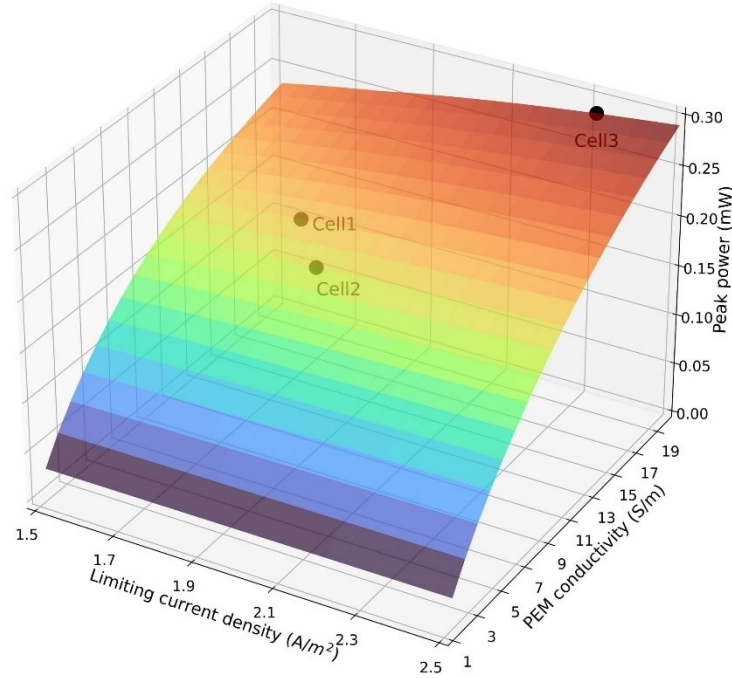


Figure 4.12 Peak power variation of the  $\mu$ -PSC at various limiting current density and PEM conductivity

#### 4.4.5. Fill Factor

The fill factor is another important parameter to characterize the cell output and generally the quality of the power generating device[96]. It can be represented by the ratio of maximum power point which happens at the voltage of  $V_{MP}$  and the current of  $I_{MP}$ , over the multiplication of open-circuit voltage of  $V_{OC}$  and short-circuits current of  $I_{SC}$  as provided in Equation 4.1. For a better comparison of the fill factor among the cells in the Independent arrayed  $\mu$ -PSC, the I-V characteristics plot has been normalized.

$$Fill\ Factor\ (FF) = \frac{I_{MP} \times V_{MP}}{I_{SC} \times V_{OC}} \quad (4.1)$$

According to figure 4.13 and the results from Table 4.4, it can be observed that the device quality and, respectively, an increase in cell output, can affect the fill factor. In the designed Independent arrayed  $\mu$ -PSC, it has been observed that cell 3 provides better output in comparison with the other two. The fill factor for cell 3 is also higher and reaches the value of 0.262. In other words, the

surface area of the purple domain increase with the increment in device output. The minimum value which has been derived is about 0.21 or higher.

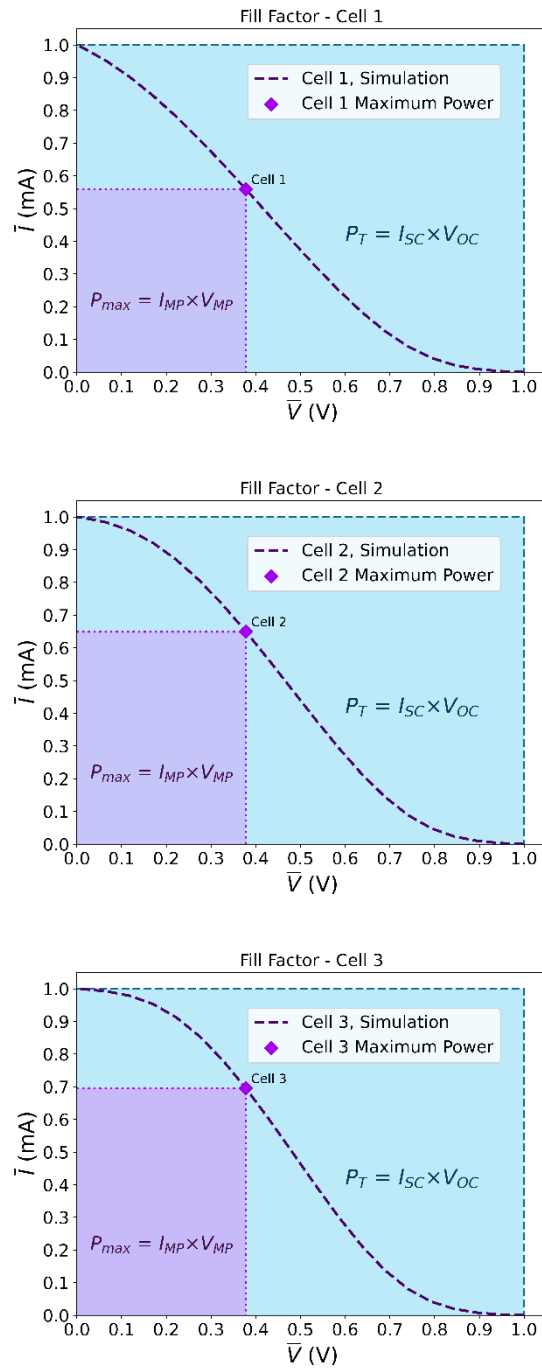


Figure 4.13 Modeling results fill factor of the Independent arrayed  $\mu$ -PSC cells

Table 4.4 Modeling fill factor value for the Independent arrayed  $\mu$ -PSC cells

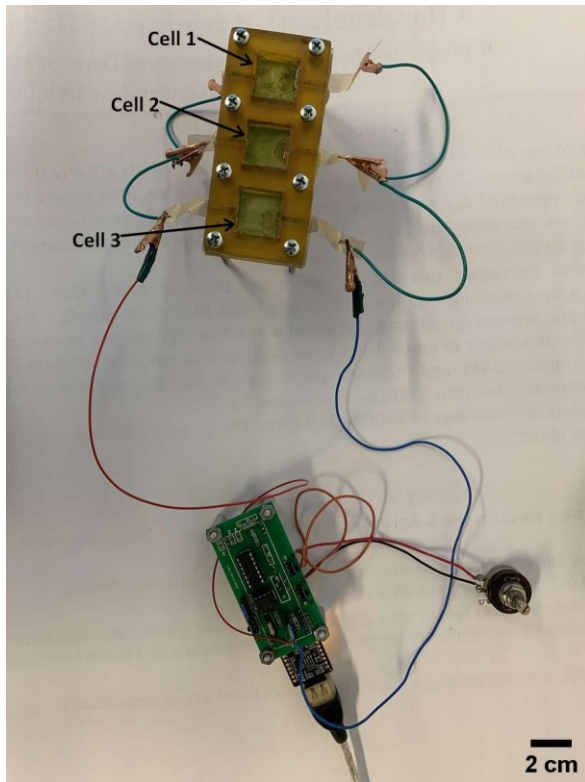
Parameter	Cell 1	Cell 2	Cell 3
Normalized current at Peak Power (mA)	0.55	0.64	0.69
Normalized voltage at Peak Power (V)	0.37	0.37	0.37
Fill Factor	0.211	0.245	0.262

#### 4.4.6. Array Configuration

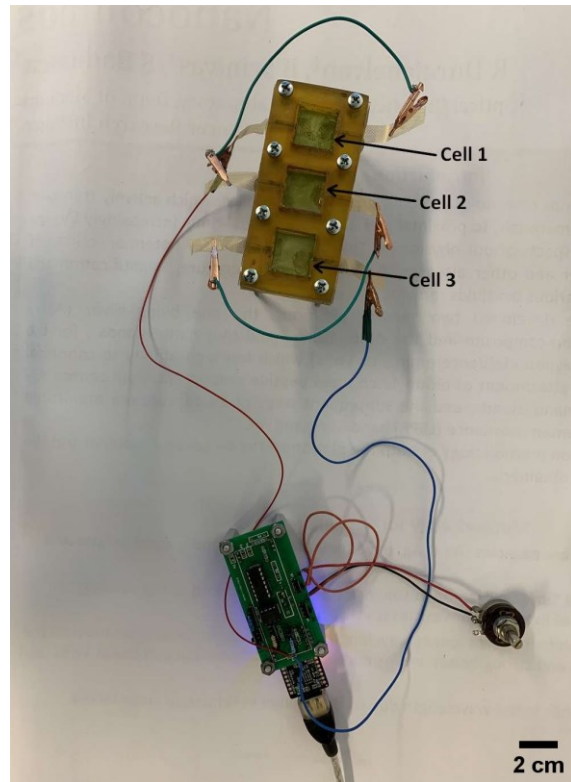
The array configuration provides the capability of obtaining different stages of voltage and current. The configuration of various series, parallel and the combination of these two have been first implemented on multiple single-chip  $\mu$ -PSC by Kuruvinashetti[45]. It was found that by having a proper combination of  $\mu$ -PSC devices, it is possible to intensify the output power. Depending on the quality of the  $\mu$ -PSC cells, the combination may need to be changed in order to get the best value. This is because a defect  $\mu$ -PSC in a non-optimized configuration can lead to extreme power loss and performance reduction.

In this section, the results from the parallel and series connection of the three independent cells in the array design are provided. As the chambers are independent and each cell in the array can function as an independent power generator, the same criteria as in [45], can be applied to see the effect of series and parallel combinations on the output of the system which is provided in Figure 4.14.





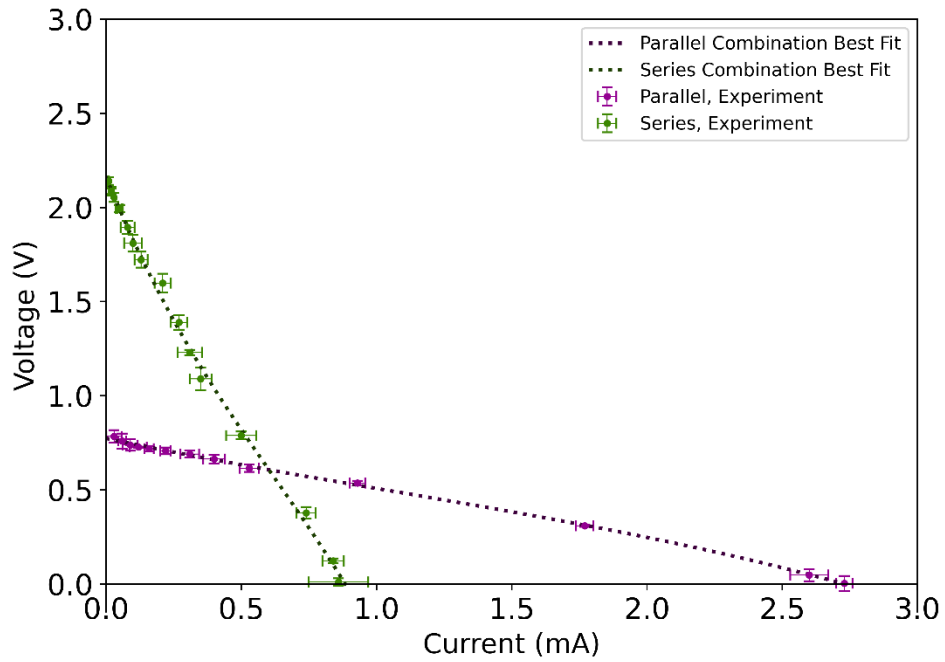
(a)



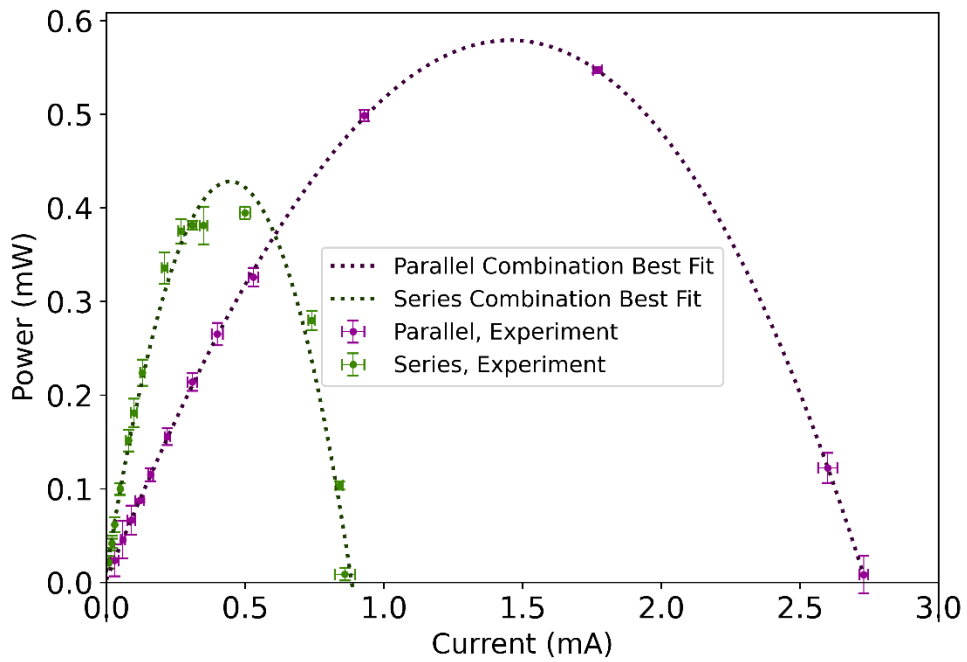
(b)

Figure 4.14 (a) Parallel and (b) series combination for the test of independent arrayed  $\mu$ -PSC

Theoretically, in the parallel combination, it is expected that the cell current increase and the cell voltage get a value around the minimum available voltage in the combination. In the series connection, it is expected that the cell voltage increases and the overall current be around the minimum available current amongst the cells.



(a)



(b)

Figure 4.15 (a) I-V characteristics and (b) power curve of three chips in series and parallel of the independent arrayed  $\mu$ -PSC

According to Figure 4.15, in series connection, the cell voltage has increased to almost three times which shows that the cell is both functioning properly. The near OCV voltage starts from about

2.1V and goes down until the near SCC current of 0.86mA. This can be a proper combination for powering small electrical components, including diodes. In parallel combination, the cell current has increased to the value of about 2.7 at the near SCC region while the cell voltage remains almost constant at about 0.77V.

The comparison between the power curve between series and parallel combination shows that the parallel combination can provide a higher peak for the power generation as the slope of its respective I-V plot is much lower than the series combination. With the combination of more independent arrayed  $\mu$ -PSC, it may be possible to attain higher levels of voltage and current depending on the need.

#### **4.5. Conclusion**

The current design and fabrication method proposed in this chapter for independently arrayed  $\mu$ -PSC, is a simple, fast, and low-cost technique in comparison with the previous designs, including the method that implements photolithography for gold deposition. Moreover, in terms of structural aspects, the fabricated frame can be tested and reused for a long time and with different testing conditions due to the selection of high-strength material. Considering the mentioned features of this design, the results follow the same trend as with the single-chip PDMS-base  $\mu$ -PSC. The results show a short-circuit current of about 0.88 to 1.1mA and an open-circuit voltage of about 800mV. It has been observed that the fabrication quality can affect primarily the cell current as the system voltage is mostly dependent on the electrochemical potential of the anolyte and catholyte. On the other hand, the modeling results have been compared with experimental results, showing that the membrane-electrodes assembly quality and deformation would be the reason for acquiring different current values among the cells. The fill factor as one of the important for the characterization of device quality is provided. The results show that a better fabrication chip can provide a higher fill factor. In addition, the I-V characteristics and power curve for the series and parallel combination have been provided. The results show that with a series connection, it is possible to attain higher cell voltage which can be used to power up small electrical components. Moreover, with the parallel connection, the system provides a higher current with the almost constant voltage as with each individual cell. The design, fabrication, and experimental results of

the independently arrayed  $\mu$ -PSC revealed to be a better choice in the development of arrayed  $\mu$ -PSC as the device has stronger structural characteristics and provides more flexibility of acquiring different levels of cell voltage and cell current with a proper combination.

## 5. Conclusion and Future Works

### 5.1. Conclusion

In this study, two fabrication techniques for the development of the array of  $\mu$ -PSC have been developed. One design consisted of  $1 \times 3$  array of  $\mu$ -PSC, which are internally connected. The second design consisted of three independent  $\mu$ -PSC chips in one single frame design. For this purpose, several materials have been examined for their compatibility with microalgae culture and cell culture medium. The results show that EPON 862 resin, PLA plastic, PDMS and Formlabs clear resin are compatible in contact with cell culture medium and microalgae culture, and no visual damage has been observed. Among the mentioned materials, the structural properties and fabrication time and overall cost, the EPON 862 resin and PLA plastic show promising potential to be used for the frame material of two designs. The first design consists of three internally connected chips. The chambers were FDM 3D-printed with PLA plastic and the technique has been explained in detail in Chapter 3. The other design consists of three independent chips. The chambers have been made with EPON 862 resin. The fabrication technique has been explained in detail in Chapter 4.

In Chapter 2, an improved model to predict the electrical behavior of the  $\mu$ -PSC was provided using COMSOL Multiphysics. The model predicts the electrical behavior based on electrochemical kinetics and the transport phenomena of the participating species in the power generation of the  $\mu$ -PSC. The prediction results were provided and evaluated through a parametric study, including the effect of internal resistance and temperature variation on the load current and load voltage. The prediction was validated with experimental results from a fabrication single-chip  $\mu$ -PSC.

The interconnected array design shows an internal connection between adjacent chambers, providing a maximum SCC of about 2.4mA in chamber 2. However, due to the internal connections, it is hard to measure the contribution of each chamber on the mentioned output current. The analysis indicated that the given designs could be useful for reaching a high current is desired. The independently arrayed  $\mu$ -PSC has been presented in Chapter 4 and the outputs of each chip have been analyzed. The results showed that each cell could show an OCV of about

760mV to 820mV and the SCC of about 800 $\mu$ A to 1.1mA, depending on the MEA fabrication quality.

The comparison between the two designs shows that the series combination in independently arrayed  $\mu$ -PSC can generate a higher overall voltage of around 2.2V than each chip in the interconnected design, which is about 0.8V. This can be used in generating different levels of voltages to power up the sensors. On the other hand, the independently arrayed design can be used to increase the output current through the parallel combination while maintaining the overall voltage at the value of 0.8V. The output current of the parallel combination in the independently arrayed  $\mu$ -PSC is around 2.6mA. More investigations and research are required for the design of the parallel and series circuit combination in the interconnected design as the cell are internally connected with each other.

In terms of the fabrication process, the presented methods for both the interconnected and independent array of  $\mu$ -PSC provide an easier and faster way for the fabrication of the  $\mu$ -PSC device. This will minimize the errors which can happen during the fabrication. The fabrication time for multiple independently arrayed  $\mu$ -PSC is lower than the interconnected array of  $\mu$ -PSC, which requires a longer time for 3D-printing the chambers with the FDM 3D printer. Moreover, independently arrayed  $\mu$ -PSC is made of EPON 862 resin which shows a stronger material specification in comparison with the interconnected array of  $\mu$ -PSC fabricated with PLA plastic. Thus, it is possible to use the independently arrayed  $\mu$ -PSC for a longer period. From the mentioned points, it can be said that the independent array designs show more promising outputs for the development of the array of  $\mu$ -PSC.

## **5.2. Future Works**

The micro-photosynthetic power cell is future technology for low and ultra-low power applications, including IoT sensors in various domains. Following the designs which discussed in this thesis, more studies can be conducted in design, material selection, and biological aspects.

Few suggestions are provided here as future works.

1. In order to increase the system's reliability, the effect of other electrode materials, including carbon-based porous sheets, instead of the gold electrode can be studied. The selected materials need to be examined for biocompatibility with microalgae culture and cell culture media to ensure reliable, long-lasting outputs.
2. It is recommended to further investigate the internal connections between the chambers in the interconnected  $\mu$ -PSC to better understand the behavior of the system.
3. Implementing other catholyte material instead of potassium ferricyanide is recommended, such as pure oxygen supply. This may require a modified design for the cathode chamber to endure the gas catholyte at the desired concentration.
4. To further increase the overall power, designing an array of  $\mu$ -PSC containing multiple  $\mu$ -PSC in an  $n \times m$  array design is recommended. The design requires a proper electrical circuit to optimize and maximize energy harvesting. The design would be capable of acquiring higher voltage and current at various levels, which can adequately supply the power for various sensors.
5. In terms of modeling, the proposed model in this study can be improved for a more realistic prediction. This can include the addition of the main photosynthesis reactions to the model.
6. To better understand the technology and investigating the phenomena in  $\mu$ -PSC for further optimization of the technology, a micro-scale device can be designed, and the behavior of algal cells in be studied with the microscopic study.
7. Study the efficiency of the  $\mu$ -PSC and the microalgae culture

## References

- [1] U. S. E. I. Administration, “International Energy Outlook 2019,” Mar. 2019. doi: 10.5860/CHOICE.44-3624.
- [2] M. Z. Jacobson *et al.*, “100% Clean and Renewable Wind, Water, and Sunlight All-Sector Energy Roadmaps for 139 Countries of the World,” *Joule*, vol. 1, no. 1, pp. 108–121, 2017, doi: 10.1016/j.joule.2017.07.005.
- [3] H. K. Tanneru, K. Kuruvinashetti, P. Pillay, R. Rengaswamy, and M. Packirisamy, “Feasibility studies of micro photosynthetic power cells as a competitor of photovoltaic cells for low and ultra-low power iot applications,” *Energies*, vol. 12, no. 9, pp. 5–9, 2019, doi: 10.3390/en12091595.
- [4] A. S. Adila, A. Husam, and G. Husi, “Towards the self-powered Internet of Things (IoT) by energy harvesting: Trends and technologies for green IoT,” *2018 2nd Int. Symp. Small-Scale Intell. Manuf. Syst. SIMS 2018*, vol. 2018-Janua, pp. 1–5, 2018, doi: 10.1109/SIMS.2018.8355305.
- [5] H. Rashidzadeh, P. S. Kasargod, T. M. Supon, R. Rashidzadeh, and M. Ahmadi, “Energy harvesting for IoT sensors utilizing MEMS technology,” *Can. Conf. Electr. Comput. Eng.*, vol. 2016-October, pp. 1–4, 2016, doi: 10.1109/CCECE.2016.7726622.
- [6] R. O’Hayre, S.-W. Cha, W. Colella, and F. B. Prinz, *Fuel Cell Fundamentals*. Hoboken, NJ, USA: John Wiley & Sons, Inc, 2016.
- [7] R. A. Felseghi, E. Carcadea, M. S. Raboaca, C. N. Trufin, and C. Filote, “Hydrogen fuel cell technology for the sustainable future of stationary applications,” *Energies*, vol. 12, no. 23, 2019, doi: 10.3390/en12234593.
- [8] J. Brey, D. Muñoz, V. Mesa, and T. Guerrero, “Use of Fuel Cells and Electrolyzers in Space Applications: From Energy Storage to Propulsion/Deorbitation,” *E3S Web Conf.*, vol. 16, 2017, doi: 10.1051/e3sconf/20171617004.
- [9] J. M. Ogden, M. M. Steinbugler, and T. G. Kreutz, “Comparison of hydrogen, methanol and gasoline as fuels for fuel cell vehicles: implications for vehicle design and infrastructure development,” *J. Power Sources*, vol. 79, no. 2, pp. 143–168, Jun. 1999, doi: 10.1016/S0378-7753(99)00057-9.
- [10] NETL, “Seventh Edition Fuel Cell Handbook,” National Energy Technology Laboratory, Pittsburgh, PA, and Morgantown, WV (United States), Pittsburgh, PA, and Morgantown, WV,

- Nov. 2004. doi: 10.2172/834188.
- [11] R. C. Neville, *Solar energy conversion : the solar cell*. Elsevier, 1995.
- [12] S. K. Jain and K. K. Sharma, “Solar Cells: In Research and Applications-A Review,” *Mater. Sci. Appl.*, vol. 6, pp. 1145–1155, 2015, doi: 10.4236/msa.2015.612113.
- [13] N. Rathore, N. L. Panwar, F. Yettou, and A. Gama, “A comprehensive review of different types of solar photovoltaic cells and their applications,” *Int. J. Ambient Energy*, pp. 1–18, Mar. 2019, doi: 10.1080/01430750.2019.1592774.
- [14] M. A. Green, E. D. Dunlop, D. H. Levi, J. Hohl-Ebinger, M. Yoshita, and A. W. Y. Ho-Baillie, “Solar cell efficiency tables (version 54),” *Prog. Photovoltaics Res. Appl.*, vol. 27, no. 7, pp. 565–575, Jul. 2019, doi: 10.1002/pip.3171.
- [15] Y. Sun, S. Wachche, and 2 Andrew Mills, “2018 Renewable Energy Grid Integration Data Book,” 2018. Accessed: Apr. 06, 2020. [Online]. Available: <https://www.nrel.gov/docs/fy20osti/74823.pdf>.
- [16] A. P. Kirk, *Solar Photovoltaic Cells: Photons to Electricity*. Elsevier Inc., 2014.
- [17] B. E. Logan, *Microbial Fuel Cells*. Hoboken, NJ, USA: Wiley Blackwell, 2008.
- [18] V. Sivasankar, P. Mylsamy, and K. Omine, *Microbial fuel cell technology for bioelectricity*. Springer International Publishing, 2018.
- [19] M. Rahimnejad, A. Adhami, S. Darvari, A. Zirepour, and S. E. Oh, “Microbial fuel cell as new technology for bioelectricity generation: A review,” *Alexandria Engineering Journal*, vol. 54, no. 3. Elsevier B.V., pp. 745–756, Sep. 01, 2015, doi: 10.1016/j.aej.2015.03.031.
- [20] C. Santoro, C. Arbizzani, B. Erable, and I. Ieropoulos, “Microbial fuel cells: From fundamentals to applications. A review,” *J. Power Sources*, vol. 356, pp. 225–244, Jul. 2017, doi: 10.1016/j.jpowsour.2017.03.109.
- [21] A. D. Tharali, N. Sain, and W. J. Osborne, “Microbial fuel cells in bioelectricity production,” *Front. Life Sci.*, vol. 9, no. 4, pp. 252–266, Oct. 2016, doi: 10.1080/21553769.2016.1230787.
- [22] M. Shahparnia, M. Packirisamy, P. Juneau, and V. Zazubovich, “Micro photosynthetic power cell for power generation from photosynthesis of algae,” *TECHNOLOGY*, vol. 03, no. 02n03, pp. 119–126, Jun. 2015, doi: 10.1142/s2339547815400099.
- [23] A. R. Dehghani-Sanij, E. Tharumalingam, M. B. Dusseault, and R. Fraser, “Study of energy

- storage systems and environmental challenges of batteries,” *Renewable and Sustainable Energy Reviews*, vol. 104. Elsevier Ltd, pp. 192–208, Apr. 01, 2019, doi: 10.1016/j.rser.2019.01.023.
- [24] T. Payarou, K. Kuruvinashetti, R. Sudharshan Kaarthik, P. Pillay, and M. Packirisamy, “Sensing Circuitry for Real-Time Power Studies of Micro-Photosynthetic Power Cells,” in *Canadian Conference on Electrical and Computer Engineering*, Aug. 2018, vol. 2018-May, doi: 10.1109/CCECE.2018.8447819.
- [25] M. A. Masadeh, K. Kuruvinashetti, M. Shahparnia, P. Pillay, and M. Packirisamy, “Electrochemical Modeling and Equivalent Circuit Representation of a Microphotosynthetic Power Cell,” *IEEE Trans. Ind. Electron.*, vol. 64, no. 2, pp. 1561–1571, Feb. 2017, doi: 10.1109/TIE.2016.2618755.
- [26] L. Taiz, E. Zeiger, I. M. Møller, and A. Murphy, *Physiology Plants*. 2014.
- [27] S. Sasso, H. Stibor, M. Mittag, and A. R. Grossman, “The natural history of model organisms from molecular manipulation of domesticated *chlamydomonas reinhardtii* to survival in nature,” *Elife*, vol. 7, Nov. 2018, doi: 10.7554/eLife.39233.
- [28] A. Richmond and Q. Hu, *Handbook of Microalgal Culture: Applied Phycology and Biotechnology: Second Edition*. Oxford, UK: wiley, 2013.
- [29] M. Shahparnia and A. Thesis, “Polymer Micro Photosynthetic Power Cell: Design, Fabrication, Parametric Study and Testing,” Concordia university, 2011.
- [30] R. M. Allen and H. P. Bennetto, “Microbial fuel-cells - Electricity production from carbohydrates,” *Appl. Biochem. Biotechnol.*, vol. 39–40, no. 1, pp. 27–40, Sep. 1993, doi: 10.1007/BF02918975.
- [31] I. A. Ieropoulos, J. Greenman, C. Melhuish, and J. Hart, “Comparative study of three types of microbial fuel cell,” *Enzyme Microb. Technol.*, vol. 37, no. 2, pp. 238–245, Jul. 2005, doi: 10.1016/j.enzmictec.2005.03.006.
- [32] L. A. Drachev, A. A. Kondrashin, V. D. Samuilov, and V. P. Skulachev, “Generation of electric potential by reaction center complexes from *Rhodospirillum rubrum*,” *FEBS Lett.*, vol. 50, no. 2, pp. 219–222, Feb. 1975, doi: 10.1016/0014-5793(75)80492-3.
- [33] L. A. Drachev *et al.*, “Reconstitution of biological molecular generators of electric current. Cytochrome oxidase,” *J. Biol. Chem.*, vol. 251, no. 22, pp. 7072–6, Nov. 1976, Accessed: May 12, 2020. [Online]. Available: <http://www.ncbi.nlm.nih.gov/pubmed/186452>.

- [34] N. K. Packham, D. M. Tiede, P. Mueller, and P. L. Dutton, "Construction of a flash-activated cyclic electron transport system by using bacterial reaction centers and the ubiquinone-cytochrome b-c1/c segment of mitochondria.," *Proc. Natl. Acad. Sci. U. S. A.*, vol. 77, no. 11, pp. 6339–6343, Nov. 1980, doi: 10.1073/pnas.77.11.6339.
- [35] N. K. Packham, C. Packham, P. Mueller, D. M. Tiede, and P. L. Dutton, "Reconstitution de photochemically active reaction centers in planar phospholipid membranes," *FEBS Lett.*, vol. 110, no. 1, pp. 101–106, Jan. 1980, doi: 10.1016/0014-5793(80)80033-0.
- [36] K. Tanaka, R. Tamamushi, and T. Ogawa, "BIOELECTROCHEMICAL FUEL-CELLS OPERATED BY THE CYANOBACTERIUM, ANABAENA VARIABILIS.," *J. Chem. Technol. Biotechnol. Biotechnol.*, vol. 35 B, no. 3, pp. 191–197, Sep. 1985, doi: 10.1002/jctb.280350304.
- [37] K. Tanaka, N. Kashiwagi, and T. Ogawa, "Effects of light on the electrical output of bioelectrochemical fuel-cells containing *Anabaena variabilis* M-2: Mechanism of the post-illumination burst," *J. Chem. Technol. Biotechnol.*, vol. 42, no. 3, pp. 235–240, Apr. 1988, doi: 10.1002/jctb.280420307.
- [38] T. Yagishita, T. Horigome, and K. Tanaka, "Effects of light, CO<sub>2</sub> and inhibitors on the current output of biofuel cells containing the photosynthetic organism *Synechococcus* sp.," *J. Chem. Technol. Biotechnol.*, vol. 56, no. 4, pp. 393–399, 1993, doi: 10.1002/jctb.280560411.
- [39] S. Tsujimura, A. Wadano, K. Kano, and T. Ikeda, "Photosynthetic bioelectrochemical cell utilizing cyanobacteria and water-generating oxidase," *Enzyme Microb. Technol.*, vol. 29, no. 4–5, pp. 225–231, Sep. 2001, doi: 10.1016/S0141-0229(01)00374-X.
- [40] K. B. Lam, M. Chiao, and L. Lin, "A micro photosynthetic electrochemical cell," *Proc. IEEE Micro Electro Mech. Syst.*, pp. 391–394, 2003, doi: 10.1109/memsys.2003.1189768.
- [41] K. B. Lam, E. A. Johnson, M. Chiao, and L. Lin, "A MEMS photosynthetic electrochemical cell powered by subcellular plant photosystems," *J. Microelectromechanical Syst.*, vol. 15, no. 5, pp. 1243–1250, 2006, doi: 10.1109/JMEMS.2006.880296.
- [42] M. Rosenbaum, U. Schröder, and F. Scholz, "Utilizing the green alga *Chlamydomonas reinhardtii* for microbial electricity generation: A living solar cell," *Appl. Microbiol. Biotechnol.*, vol. 68, no. 6, pp. 753–756, Oct. 2005, doi: 10.1007/s00253-005-1915-4.
- [43] A. V. Ramanan, "ENERGY HARVESTING AND MODELING OF PHOTOSYNTHETIC POWER CELL," 2013.

- [44] P. Bombelli, T. Müller, T. W. Herling, C. J. Howe, and T. P. J. Knowles, “A high power-density, mediator-free, microfluidic biophotovoltaic device for cyanobacterial cells,” *Adv. Energy Mater.*, vol. 5, no. 2, 2015, doi: 10.1002/aenm.201401299.
- [45] K. Kuruvinashetti, “Arrayed Micro-Photosynthetic Power Cell: Modeling, Testing and Performance Enhancement,” Concordia University, 2020.
- [46] D. H. Park and J. G. Zeikus, “Electricity generation in microbial fuel cells using neutral red as an electronophore,” *Appl. Environ. Microbiol.*, vol. 66, no. 4, pp. 1292–1297, Apr. 2000, doi: 10.1128/AEM.66.4.1292-1297.2000.
- [47] D. L. Nelson and M. M. Cox, *Loose-leaf Version for Lehninger Principles of Biochemistry*. W. H. Freeman, 2017.
- [48] K. Kuruvinashetti, G. Guoqing, J. Haobin, and M. Packirisamy, “Perspective—Application of Micro Photosynthetic Power Cells for IoT in Automotive Industry,” *J. Electrochem. Soc.*, vol. 167, no. 3, p. 037545, Jan. 2020, doi: 10.1149/1945-7111/ab67ae.
- [49] M. Ma, X. Shi, L. Cao, and Z. Deng, “The operation of photosynthetic microbial fuel cells powered by *Anabaena variabilis*,” in *ICMREE 2013 - Proceedings: 2013 International Conference on Materials for Renewable Energy and Environment*, 2013, vol. 3, pp. 968–972, doi: 10.1109/ICMREE.2013.6893833.
- [50] M. T. Winkler, C. R. Cox, D. G. Nocera, and T. Buonassisi, “Modeling integrated photovoltaic-electrochemical devices using steady-state equivalent circuits,” *Proc. Natl. Acad. Sci. U. S. A.*, vol. 110, no. 12, pp. E1076–E1082, Mar. 2013, doi: 10.1073/pnas.1301532110.
- [51] Y. Zeng, Y. F. Choo, B. H. Kim, and P. Wu, “Modelling and simulation of two-chamber microbial fuel cell,” *J. Power Sources*, vol. 195, no. 1, pp. 79–89, Jan. 2010, doi: 10.1016/j.jpowsour.2009.06.101.
- [52] V. B. Oliveira, M. Simões, L. F. Melo, and A. M. F. R. Pinto, “A 1D mathematical model for a microbial fuel cell,” *Energy*, vol. 61, pp. 463–471, Nov. 2013, doi: 10.1016/j.energy.2013.08.055.
- [53] T. Payarou, S. Rahimi, K. Kuruvinashetti, P. Pillay, and M. Packirisamy, “Detailed Electrochemical Model of Microphotosynthetic Power Cells,” *IEEE Trans. Ind. Appl.*, vol. 57, no. 2, pp. 1703–1714, Mar. 2021, doi: 10.1109/TIA.2020.3044032.
- [54] S. D. Gallaher, S. T. Fitz-Gibbon, A. G. Glaesener, M. Pellegrini, and S. S. Merchanta, “*Chlamydomonas* genome resource for laboratory strains reveals a mosaic of sequence variation,

- identifies true strain histories, and enables strain-specific studies,” *Plant Cell*, vol. 27, no. 9, pp. 2335–2352, 2015, doi: 10.1105/tpc.15.00508.
- [55] A. V. Ramanan, M. Pakirisamy, and S. S. Williamson, “Advanced fabrication, modeling, and testing of a microphotosynthetic electrochemical cell for energy harvesting applications,” *IEEE Trans. Power Electron.*, vol. 30, no. 3, pp. 1275–1285, 2015, doi: 10.1109/TPEL.2014.2317675.
- [56] C. Spiegel, *PEM Fuel Cell Modeling and Simulation Using Matlab*. 2008.
- [57] F. Barbir, *PEM Fuel Cells*. Academic Press, 2005.
- [58] H. K. Tanneru *et al.*, “Integrated bio-electrochemical model for a micro photosynthetic power cell,” *TECHNOLOGY*, vol. 04, no. 04, pp. 249–258, Sep. 2016, doi: 10.1142/s2339547816500114.
- [59] C.-P.-B. Siu and Mu Chiao, “A Microfabricated PDMS Microbial Fuel Cell,” *J. Microelectromechanical Syst.*, vol. 17, no. 6, pp. 1329–1341, Dec. 2008, doi: 10.1109/JMEMS.2008.2006816.
- [60] L. R. F. Allen J. Bard, *Electrochemical Methods: Fundamentals and Applications, 2nd Edition*. New York: Wiley, 2000.
- [61] “Chemical Reaction Engineering Module User’s Guide,” 1998. Accessed: Mar. 23, 2021. [Online]. Available: [www.comsol.com/blogs](http://www.comsol.com/blogs).
- [62] T. Stocker, *Introduction to Climate Modelling*, Illustrate. Springer Science & Business Media, 2011.
- [63] R. Taylor and R. Krishna, “Multicomponent mass transfer,” p. 579, 1993.
- [64] M. Bavarian, M. Soroush, I. G. Kevrekidis, and J. B. Benziger, “Mathematical modeling, steady-state and dynamic behavior, and control of fuel cells: A review,” *Ind. Eng. Chem. Res.*, vol. 49, no. 17, pp. 7922–7950, Sep. 2010, doi: 10.1021/ie100032c.
- [65] S. E. Oh and B. E. Logan, “Proton exchange membrane and electrode surface areas as factors that affect power generation in microbial fuel cells,” *Appl. Microbiol. Biotechnol.*, vol. 70, no. 2, pp. 162–169, Mar. 2006, doi: 10.1007/s00253-005-0066-y.
- [66] H. K. Tanneru, K. Kuruvinashetti, P. Pillay, R. Rengaswamy, and M. Packirisamy, “Perspective—Micro Photosynthetic Power Cells,” *J. Electrochem. Soc.*, vol. 166, no. 9, pp. B3012–B3016, 2019, doi: 10.1149/2.0031909jes.

- [67] L. Di Benedetto De Caprariis, Paolo De Filippis, Antonella Di Battista\* and M. S. Palma, “Exoelectrogenic Activity of a Green Microalgae, *Chlorella vulgaris*, in a Bio-Photovoltaic Cells (BPVs),” 2014, vol. 38, doi: 10.3303/CET1438088.
- [68] S. J. L. Rowden, P. Bombelli, and C. J. Howe, “Biophotovoltaics: Design and Study of Bioelectrochemical Systems for Biotechnological Applications and Metabolic Investigation,” in *The Life and Works of Thomas Cole*, vol. 1770, 2018, pp. 335–346.
- [69] M. Shim, J. Jeong, J. Maeng, I. Park, and C. Kim, “Fully Integrated Low-Power Energy Harvesting System with Simplified Ripple Correlation Control for System-on-a-Chip Applications,” *IEEE Trans. Power Electron.*, vol. 34, no. 5, pp. 4353–4361, May 2019, doi: 10.1109/TPEL.2018.2863390.
- [70] P. Mayer, M. Magno, and L. Benini, “Smart Power Unit - MW-to-nW Power Management and Control for Self-Sustainable IoT Devices,” *IEEE Trans. Power Electron.*, vol. 36, no. 5, pp. 5700–5710, May 2021, doi: 10.1109/TPEL.2020.3031697.
- [71] C. W. Hung and W. T. Hsu, “Power consumption and calculation requirement analysis of AES for WSN IoT,” *Sensors (Switzerland)*, vol. 18, no. 6, p. 1675, Jun. 2018, doi: 10.3390/s18061675.
- [72] N. H. Behling, “Fuel Cells and the Challenges Ahead,” in *Fuel Cells*, Elsevier, 2013, pp. 7–36.
- [73] Dow Chemical Company, “D.E.R. 324 Liquid Epoxy Resin,” Dow Chemical Company. Accessed: Apr. 01, 2021. [Online]. Available: [http://sfile-pull.f-static.com/image/users/423667/ftp/my\\_files/Srafim/epoxy/DOW\\_324.pdf?id=27507802](http://sfile-pull.f-static.com/image/users/423667/ftp/my_files/Srafim/epoxy/DOW_324.pdf?id=27507802).
- [74] Hexion Inc., “Benefits of Using EPON Resin 862,” 2005.
- [75] B. M. Priyadarshini, V. Dikshit, and Y. Zhang, “3D-printed bioreactors for in vitro modeling and analysis,” *International Journal of Bioprinting*, vol. 6, no. 4. Whioce Publishing Pte. Ltd., p. 267, 2020, doi: 10.18063/IJB.V6I4.267.
- [76] Hexion Inc., “Hand Lay-up FRP Matrix EPON™ Resin 862 / HELOXY™ Modifier 68 / EPIKURE™ Curing Agent 3234.” Accessed: Apr. 01, 2021. [Online]. Available: [www.hexion.com/Contacts/](http://www.hexion.com/Contacts/).
- [77] F. M. PROPERTIES, “Safety Data Sheet.” Accessed: Apr. 22, 2021. [Online]. Available: [www.GSMSDS.com](http://www.GSMSDS.com).
- [78] FORMLABS MATERIAL PROPERTIES, “Standard Materials for High-Resolution Rapid

Prototyping.”

- [79] S. Pakkiriswami, B. F. N. Beall, and D. P. Maxwell, “On the role of photosynthesis in the nitratedependent induction of the alternative oxidase in *Chlamydomonas reinhardtii*,” *Botany*, vol. 87, no. 4, pp. 363–374, Apr. 2009, doi: 10.1139/B09-004.
- [80] I. D. Johnston, D. K. McCluskey, C. K. L. Tan, and M. C. Tracey, “Mechanical characterization of bulk Sylgard 184 for microfluidics and microengineering,” *J. Micromechanics Microengineering*, vol. 24, no. 3, p. 035017, Feb. 2014, doi: 10.1088/0960-1317/24/3/035017.
- [81] L. Napoli, M. J. Lavorante, J. Franco, A. Sanguinetti, and H. Fasoli, “Effects on nafion® 117 membrane using different strong acids in various concentrations,” *J. New Mater. Electrochem. Syst.*, vol. 16, no. 3, pp. 151–156, Jul. 2013, doi: 10.14447/jnmes.v16i3.4.
- [82] S. Pujiastuti and H. Onggo, “Effect of various concentration of sulfuric acid for Nafion membrane activation on the performance of fuel cell,” in *AIP Conference Proceedings*, Feb. 2016, vol. 1711, no. 1, p. 060006, doi: 10.1063/1.4941639.
- [83] G. B. W. Harris, Elizabeth H., David B. Stern, Ed., *The Chlamydomonas Sourcebook*. Academic Press, 1989.
- [84] T. Payarou, “Micro-Photosynthetic Power Cell Modeling, Sensing, and Energy Harvesting,” Concordia Univeristy, 2018.
- [85] P. Baert, T. Bosteels, and P. Sorgeloos, *Manual on the Production and Use of Live Food for Aquaculture*. Rome: Food and Agriculture Organization (FAO), 1996.
- [86] J. Xu, G. P. Sheng, H. W. Luo, W. W. Li, L. F. Wang, and H. Q. Yu, “Fouling of proton exchange membrane (PEM) deteriorates the performance of microbial fuel cell,” *Water Res.*, vol. 46, no. 6, pp. 1817–1824, Apr. 2012, doi: 10.1016/j.watres.2011.12.060.
- [87] H. Rismani-Yazdi, S. M. Carver, A. D. Christy, and O. H. Tuovinen, “Cathodic limitations in microbial fuel cells: An overview,” *Journal of Power Sources*, vol. 180, no. 2. Elsevier, pp. 683–694, Jun. 01, 2008, doi: 10.1016/j.jpowsour.2008.02.074.
- [88] M. Rahimnejad, A. A. Ghoreyshi, G. Najafpour, and T. Jafary, “Power generation from organic substrate in batch and continuous flow microbial fuel cell operations,” *Appl. Energy*, vol. 88, no. 11, pp. 3999–4004, Nov. 2011, doi: 10.1016/j.apenergy.2011.04.017.
- [89] F. Akdeniz, A. Çağlar, and D. Güllü, “Recent energy investigations on fossil and alternative

- nonfossil resources in Turkey,” *Energy Convers. Manag.*, vol. 43, no. 4, pp. 575–589, Mar. 2002, doi: 10.1016/S0196-8904(01)00036-X.
- [90] A. J. McCormick *et al.*, “Photosynthetic biofilms in pure culture harness solar energy in a mediatorless bio-photovoltaic cell (BPV) system,” *Energy Environ. Sci.*, vol. 4, no. 11, pp. 4699–4709, Nov. 2011, doi: 10.1039/c1ee01965a.
- [91] R. Thorne *et al.*, “Porous ceramic anode materials for photo-microbial fuel cells,” *J. Mater. Chem.*, vol. 21, no. 44, pp. 18055–18060, Nov. 2011, doi: 10.1039/c1jm13058g.
- [92] FORMLABS MATERIAL PROPERTIES, “Flexible Resin for Ergonomic Features,” 2016.
- [93] V. K. Rangari, M. S. Bhuyan, and S. Jeelani, “Microwave curing of CNFs/EPON-862 nanocomposites and their thermal and mechanical properties,” *Compos. Part A Appl. Sci. Manuf.*, vol. 42, no. 7, pp. 849–858, Jul. 2011, doi: 10.1016/j.compositesa.2011.03.014.
- [94] S. J. Paddison and K. S. Promislow, Eds., *Device and Materials Modeling in PEM Fuel Cells*, vol. 113. New York, NY: Springer New York, 2009.
- [95] M. Cassir, D. Jones, A. Ringuedé, and V. Lair, “Electrochemical devices for energy: Fuel cells and electrolytic cells,” in *Handbook of Membrane Reactors*, vol. 2, Elsevier Ltd, 2013, pp. 553–606.
- [96] S. Tsujimura, A. Wadano, K. Kano, and T. Ikeda, “Photosynthetic bioelectrochemical cell utilizing cyanobacteria and water-generating oxidase,” *Enzyme Microb. Technol.*, vol. 29, no. 4–5, pp. 225–231, Sep. 2001, doi: 10.1016/S0141-0229(01)00374-X.